Louisiana State University
LSU Digital Commons

LSU Doctoral Dissertations Graduate School

2014

Performance Characterization of the Dual-Recycled Michelson Subsystem in Advanced LIGO

Anamaria Effler
Louisiana State University and Agricultural and Mechanical College, aeffle2@lsu.edu

Follow this and additional works at: https://digitalcommons.lsu.edu/gradschool_dissertations

Part of the Physical Sciences and Mathematics Commons

Recommended Citation

Effler, Anamaria, "Performance Characterization of the Dual-Recycled Michelson Subsystem in Advanced LIGO" (2014). *LSU Doctoral Dissertations*. 2888.
https://digitalcommons.lsu.edu/gradschool_dissertations/2888

This Dissertation is brought to you for free and open access by the Graduate School at LSU Digital Commons. It has been accepted for inclusion in LSU Doctoral Dissertations by an authorized graduate school editor of LSU Digital Commons. For more information, please contactgradetd@lsu.edu.

PERFORMANCE CHARACTERIZATION OF THE DUAL-POWER RECYCLED MICHELSON SUBSYSTEM IN ADVANCED LIGO

A Dissertation

Submitted to the Graduate Faculty of the
Louisiana State University and
Agricultural and Mechanical College
in partial fulfillment of the
requirements for the degree of
Doctor of Philosophy

in

The Department of Physics and Astronomy

by
Anamaria Effler
B.S., California Institute of Technology, 2006
May 2015

For my grandmother, Florica Ruja.

ACKNOWLEDGMENTS

There are many people who made this dissertation possible, either directly, by providing me with help and advice, or indirectly, by influencing my life and my view of it. Some have done both. I have to thank my parents and grandparents for raising me in a difficult economic and political environment. I want to thank Prof. Alan Weinstein and Dr. Riccardo DeSalvo for enticing me to work with the LIGO project during my college years. During my time as an operator, the staff of the LIGO Hanford Observatory and in particular Dr. Rick Savage gave me the first hands-on introduction to the LIGO detector for which I would develop quite the affinity.

From my time as a graduate student I have immense gratitude for two people in particular: my adviser, Prof. Gabriela González and my local LIGO mentor, Dr. Valera Frolov. Without them, I would have been lost. Aside from direct scientific knowledge, they provided a strange but very effective balance: Gabriela teaching me to appreciate when work is done well enough to move on and to have confidence in my abilities; and Valera teaching me to always dig deeper and question everything, including myself.

I would like to thank some great LIGO scientists: Prof. Rana Adhikari, Dr. Lisa Barsotti, Prof. Matt Evans, Dr. Peter Fritschel and, of course, Prof. Rai Weiss for the wisdom they leaked in my direction, knowingly or not. Plus a thank you to Dr. Robert Schofield, who taught me that no measurement is too strange, just the amount of required care and persistence in completing it may vary.

I owe a great deal of thanks to my peers working or who have worked at the LIGO Livingston Observatory. They have helped me with measurements, advice, support, friendship, entertainment and splitting rent (in acquaintance order): Kate Dooley, Nic Smith, Jeff Kissel, Tobin Fricke, Ryan DeRosa, Jenne Driggers, Keiko Kokeyama, Adam Mullavey, Chris Mueller, Jan Poeld, Zach Korth, Den Martynov and Rob Ward. And last but not least I have to thank the staff of the Livingston Observatory for tolerating me and being immensely helpful.

TABLE OF CONTENTS

APPENDIX

LIST OF TABLES

LIST OF FIGURES

ABSTRACT

General relativity predicts the existence of gravitational waves as ripples in space-time propagating at the speed of light. They couple to matter weakly, which implies only cataclysmic cosmic events generating such waves can be detected. Binary neutron star coalescences are, for example, one of the most promising detectable source. Their weak coupling also implies that very sensitive instruments are needed to detect them, and the most sensitive so far have been laser interferometers with km-scale arms. The Laser Interferometric Gravitational wave Observatory (LIGO) is exactly such an instrument, and the most sensitive in the world to the date of this dissertation. It operates two identical interferometers, one in Hanford, WA and one in Livingston, LA.

I will present noise studies on two different topics.First, studies of environmental effects in the enhanced LIGO detector era (2008-2010) for both sites, showing that stationary ambient environmental noise did not limit the sensitivity at the time. After enhanced LIGO, advanced LIGO began installation, where all hardware was replaced except the enclosing vacuum system. The expected improvement in sensitivity is designed to be tenfold, which results in a factor of a thousand in the volume of space from where a source could be detected.

This dissertation then focuses on a sub-configuration of advanced LIGO, the dual-recycled Michelson interferometer (DRMI), which is the LIGO instrument without the 4km arms. I will expose in detail the length sensing and control scheme which is the cornerstone of LIGO's ability to provide a linear gravitational wave readout. We model the behavior of the instrument in order to identify key commissioning targets. I will present models and measurements I performed at the Livingston Observatory for assessing two main topics: the sensing performance and the noise couplings in the DRMI.

This work has only been possible with the support from the NSF grants NSF-PHY 0905184 and 1205882.

CHAPTER 1
INTRODUCTION

1.1 A Bit of History

Albert Einstein revolutionized the world of physics when he published his theory of general relativity in 1916 [5]. It explained the redshift of light, Mercury's perihelion precession and the lensing of light around the Sun - just to name a few simple examples. Its main assumption is that space and time are not independent, but exist as a four dimensional manifold which can be curved by matter. In turn motion of mass is dictated by the curvature of spacetime.

General relativity also predicts the existence of gravitational waves (GW) propagating freely through spacetime at the speed of light. However, their interaction with matter is so weak that there was little hope to detect them. Joseph Weber was the first to challenge this statement; he was unsuccessful despite a hasty announcement in 1964 that he had detected gravitational waves. His work energized the scientific community and the field of gravitational wave detection was born [6].

In 1973 the Hulse-Taylor pulsar was discovered, and its observation over the past some 40 years has been one of the most accurate tests of the existence of gravitational waves, when comparing the observed decay of the orbit with the general relativity prediction of energy loss through gravitational wave emission [7].

1.2 Motivation for Gravitational Wave Research

The direct detection of gravitational waves is not only a further test of general relativity, but would provide us with a different view of the universe. All astronomical observations to date use either particles such as neutrinos or the electromagnetic spectrum; once a new region of the spectrum was technologically possible to investigate, the amount of knowledge we gained about the universe was beyond predictions. An obvious example is the cosmic microwave background. Gravitational waves are a different spectrum entirely which does not require the existence of electromagnetic interactions but of massive, compact objects accelerating rapidly.

Furthermore, due to their weak interaction with matter, they can provide less distorted information (compared to light) from distant objects. Therefore we can characterize the astrophysical sources which produce gravitational waves when detecting them. Table 1.1 shows the four types of the most likely sources, categorized by two criteria: whether the waveform can be analytically calculated and whether the emission is coherent over a long period of time (continuous sources) or is of a very short duration (bursts). The distance row gives an approximate idea of the distance that these sources could be detected by ground based detectors, based on signal strength. When calculating such distances accurately, we have to know the models for the sources as well as the response and sensitivity of the detector [8]. Continuous sources can be detected even if the signal is smaller because it can be integrated over a long period of time as it is sinusoidal[9]. Knowing location in the sky and the rotational period of a pulsar (e.g. the Crab) reduces the parameter space of the search nicely. The stochastic background predicted to exist from the Big Bang is especially of interest because gravitational waves were emitted before light could escape, and could provide information even closer to the birth of the universe. This signal is very weak and stochastic, so it can only be extracted from a long coherent integration. This signal would be too small for LIGO to detect, unless inflation theories are wrong, but it could detect a background from small, unresolved sources. If not, LIGO could set upper bounds on such a stochastic background.

Table 1.1: Types of GW sources and signals

Time	Long Duration		Short Duration	
Waveform	Known	Unknown	Known	Unknown
Signal Character	Continuous	Stochastic	Inspirals	Bursts
Example	Pulsar	Big Bang	NS-NS	Supernova
Distance	galactic	-	extragalactic	galactic

Compact object inspiral merger signals are only strong enough to be detected by LIGO close in time to their merger, when their orbital period is much less than one second and their proximity produces larger amplitude gravitational waves. The waveform has been numerically calculated both before the merger (inspiral phase), during the merger and after the merger (ringdown phase). These sources are considered the most likely for a first detection both because of their strength and the analytical knowledge of the inspiral waveform. Data analysis pipelines can use a set of templates of different parameters (masses, sky position, polarization, etc) to extract such signals from data, which provides us with not more confidence in the detection of a signal and also a test of our theoretical understanding and numerical modeling methods.

1.3 Gravitational Waves Propagation, Effect and Generation

To understand the properties and propagation of GWs, we need to solve the Einstein field equation, but we can apply further simplifications such as vacuum propagation (where the stress-energy tensor $\mathbf{T} = 0$). The general field equation is:

$$\mathbf{G} = \frac{8\pi \mathrm{G}}{\mathrm{c}^4}\mathbf{T} \text{ with} \tag{1.1}$$

$\mathbf{G} = \mathbf{R}_{\mu\nu} - \frac{1}{2}Rg_{\mu\nu}$ the Einstein Tensor, $\mathbf{R}_{\mu\nu}$ the Ricci curvature tensor, R the Ricci scalar, G the gravitational constant, c the speed of light and $\mathbf{T}$ the stress-energy tensor.

In the weak field limit the space metric $\mathrm{g}_{\mu\nu}$ which encodes full information about the curvature of spacetime can be approximated as:

$$\mathrm{g}_{\mu\nu} = \eta_{\mu\nu} + \mathrm{h}_{\mu\nu}, \tag{1.2}$$

where $\eta_{\mu\nu}$ is the flat space Minkowski metric and $\mathrm{h}_{\mu\nu}$ is a small perturbation applied on this flat metric - the GW we are looking for. With these approximations, the field equations reduce to a simple wave equation (in Lorentz gauge):

$$\Box\bar{\mathrm{h}}_{\mu\nu} = 0 \text{ with } \bar{\mathrm{h}}_{\mu\nu} \equiv \mathrm{h}_{\mu\nu} - \frac{1}{2}\eta_{\mu\nu}\mathrm{h}. \tag{1.3}$$

In the transverse traceless (TT) gauge this equation can be solved, and the solutions for a wave propagating in the z direction are of the form:

$$\bar{\mathrm{h}}_{\mu\nu} = \begin{pmatrix} 0 & 0 & 0 & 0 \\ 0 & h_+ & h_\times & 0 \\ 0 & h_\times & -h_+ & 0 \\ 0 & 0 & 0 & 0 \end{pmatrix} * \cos(2\pi \mathrm{f}(\mathrm{t} - \frac{\mathrm{r}}{\mathrm{c}})), \tag{1.4}$$

where h_+ is the plus polarization, $h_\times$ is the cross polarization, f is the frequency of the GW, t is time, r is the distance coordinate and c is the speed of light. This shows that GW have two polarizations, they propagate at the speed of light and are transverse. The polarizations are aptly named to be suggestive of the effect on spacetime. It is stretched and compressed either in a + or × pattern perpendicular to the direction of propagation of the wave, as can be seen in Figure 1.1. $\mathrm{h}_{\mu\nu}$ is dimensionless and represents a strain, defined as $\Delta\mathrm{L}/\mathrm{L}$, how much the length L is stretched by a passing wave.

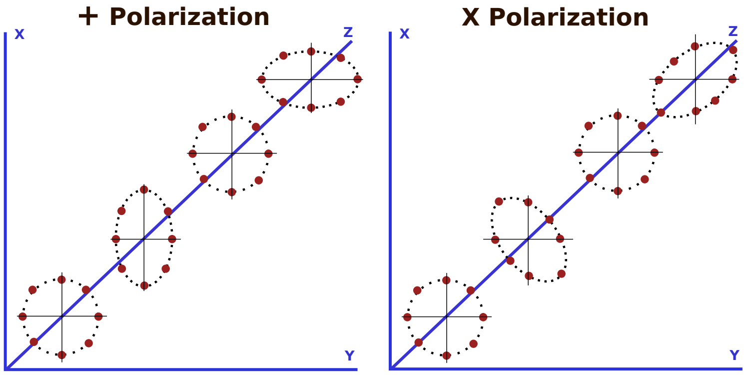

Figure 1.1: Schematic of the two polarization of gravitational waves shown propagating in z-direction

At the source, the stress-energy tensor is not zero, and solving the corresponding field equation yields the approximate solution (with time and spacial components separated):

$$\bar{\mathrm{h}}_{\mathrm{ab}}(\mathrm{t},\mathbf{x}) = \frac{16\pi \mathrm{G}}{\mathrm{rc}^4}\frac{\partial^2}{\partial^2 \mathrm{t}}\mathbf{I}_{\mathrm{ab}}(\mathrm{t}-\frac{\mathrm{r}}{\mathrm{c}}), \tag{1.5}$$

where $\mathbf{I}_{\mathrm{ab}}$ is the quadrupole moment of inertia, and here r is the distance to the source. This is the lowest order term in the solution; monopole terms are forbidden by conservation of mass (similar to electromagnetism where conservation of charge forbids monopole radiation) and dipole terms are forbidden by conservation of momentum, angular momentum and the absence of negative mass. This solution shows that GW amplitude decays as 1/r and that in order to have be a source of GW, the object needs to have a time-varying quadrupole moment. A perfectly spherical rotating object will not emit GW.

1.3.1 Example 1: Pulsars

Pulsars, which are rotating neutron stars, can only produce GWs if they have some asymmetry. If they do, then they will have a time-varying quadrupole moment. We assume a 1cm "mountain" on the surface, a 10 km radius, a 1.4 $\mathrm{M}_\odot$ mass, rotation about the z axis and observation angle ι with respect to the rotation axis we get an ellipticity $\epsilon \equiv (\mathrm{I}_{\mathrm{xx}} - \mathrm{I}_{\mathrm{yy}})/\mathrm{I}_{\mathrm{zz}} \approx 10^{-6}$ and a principal moment of inertia $\mathrm{I}_{\mathrm{zz}} \simeq \frac{2}{5}\mathrm{ma}^2 \approx 10^{38}\mathrm{kg\ m}^2$. The wave has a frequency of $\mathrm{f}_{\mathrm{GW}} = 2\mathrm{f}_{\mathrm{rot}}$ and the two strain polarizations are given by [10]:

$$\begin{aligned}
&\mathrm{h}_+ = \mathrm{h}_0\frac{1+\cos^2\iota}{2}\cos(2\pi \mathrm{f}_{\mathrm{GW}}(\mathrm{t}-\frac{\mathrm{r}}{\mathrm{c}})),\\
&\mathrm{h}_\times = \mathrm{h}_0\cos^2\iota\,\cos(2\pi \mathrm{f}_{\mathrm{GW}}(\mathrm{t}-\frac{\mathrm{r}}{\mathrm{c}})) \quad \text{with}\\
&\mathrm{h}_0 = \frac{4\pi^2\mathrm{G}}{\mathrm{c}^4}\frac{\mathrm{I}_{\mathrm{zz}}\mathrm{f}_{\mathrm{GW}}^2}{\mathrm{r}}\epsilon \quad \text{or}\\
&\mathrm{h}_0 \simeq 1.06 * 10^{-25}\left(\frac{\epsilon}{10^{-6}}\right)\left(\frac{\mathrm{I}_3}{10^{38}\mathrm{kg\ m}^2}\right)\left(\frac{10\mathrm{kpc}}{\mathrm{r}}\right)\left(\frac{\mathrm{f}_{\mathrm{GW}}}{1\mathrm{kHz}}\right)^2.
\end{aligned} \tag{1.6}$$

The power carried away by these gravitational waves, given by the derivative of energy loss with time, is [10]:

$$
\begin{aligned}
&\mathrm{P} = \frac{32\mathrm{G}}{5\mathrm{c}^5}\epsilon^2 \mathrm{I}_{\mathrm{zz}}^2 \omega_{\mathrm{rot}}^6 \quad \text{or} \\
&\mathrm{P} \simeq 1.7 * 10^{33}\mathrm{W}\left(\frac{\epsilon}{10^{-6}}\right)^2 \left(\frac{\mathrm{I}_3}{10^{38}\mathrm{kg\ m}^2}\right)^2 \left(\frac{\mathrm{f}_{\mathrm{rot}}}{500\mathrm{Hz}}\right)^6 .
\end{aligned}
\tag{1.7}
$$

This simplified example shows that while gravitational waves carry away a lot of energy, they interact very little with matter. In other words, spacetime is very rigid.

1.3.2 Example 2: Inspiraling Neutron Star Binary

A binary system has a quadrupole moment varying periodically with frequency as the two objects orbit each other, and will emit gravitational waves. As the system loses energy it will slowly inspiral, making the rotational frequency larger and in turn losing even more energy. Defining the chirp mass of a binary as $\mathrm{M_c} = \mu^{3/5}(\mathrm{m}_1 + \mathrm{m}_2)^{2/5}$, we obtain the same form for the two polarizations of the spacetime strain as equations 6 and 7, with ι being the angle of the observer with respect to the plane of rotation. Unfortunately, due to the low frequency of rotation relative to what is technologically detectable on Earth, the inspiral can only be detected in the last few minutes before the merger, at best. The amplitude h_0 with the simplification of circular orbits is:

$$
\mathrm{h}_0 = \frac{4}{\mathrm{r}}\left(\frac{\mathrm{GM_c}}{\mathrm{c}^2}\right)^{5/3}\left(\frac{\pi \mathrm{f}_{\mathrm{GW}}}{\mathrm{c}}\right)^{2/3}
$$

It is interesting to see how the frequency of the GW depends on time until merger τ, which can be calculated from initial period T_0 until the binary reaches the innermost stable circular orbit (ISCO) of radius 6M (where M is the mass of the system):

$$
\tau = 9.829 \times 10^6 \mathrm{yrs}\left(\frac{\mathrm{T}_0}{1\mathrm{hr}}\right)^{8/3}\left(\frac{\mathrm{M}_\odot}{\mathrm{m}_1 + \mathrm{m}_2}\right)^{2/3}\left(\frac{\mathrm{M}_\odot}{\mu}\right), \tag{1.8}
$$

with $\mu = \mathrm{m}_1\mathrm{m}_2/(\mathrm{m}_1 + \mathrm{m}_2)$ the reduced mass,

$$
\mathrm{f}_{\mathrm{GW}} = 134\mathrm{Hz}\left(\frac{1.21\mathrm{M}_\odot}{\mathrm{M_c}}\right)^{5/8}\left(\frac{1\mathrm{s}}{\tau}\right)^{3/8} . \tag{1.9}
$$

The time until coalescence is calculated as the time until the binary reaches the inner-most stable circular orbit (ISCO). The frequency a day before merger is ∼2Hz for example. The strain amplitude h_0 for a system with chirp mass 1.21 $\mathrm{M}_\odot$ (made of two neutron stars of mass 1.4 $\mathrm{M}_\odot$) at a distance of 15 Mpc becomes $\sim 9 \times 10^{-24}$ a day before coalescence and at 1s before it is $\sim 10^{-22}$.

The power radiated away is:

$$\mathrm{P} = \frac{32\mathrm{c}^5}{5\mathrm{G}} \left(\frac{\mathrm{G M_c} \omega_{\mathrm{GW}}}{2\mathrm{c}^3} \right)^{10/3} \tag{1.10}$$

which one second before the merger is $\sim 10^{44}$ Watts! Again we notice the discrepancy between energy carried away by GW and their weak subsequent interaction with spacetime.

1.4 The Laser Interferometric Gravitational-wave Observatory (LIGO)

There have been two main approaches to the direct detection of gravitational waves: bar detectors and interferometric detectors, the latter shown in Figure 1.2 [11][12][13].Though the quest for GW started with resonant bar detectors, including Allegro - the LSU commissioned detector [14], the wide band operation of interferometric detectors has won over the resonant-mass detector narrow band sensitivity. In addition there are other gravitational wave experiments which are more source specific, employing pulsar timing[15] and cosmic microwave background polarization[16].

LIGO was approved for funding by the National Science Foundation in 1992, with two interferometers in Hanford, WA and one in Livingston, LA. The detectors consist of a Michelson interferometer setup, with 4km long arms housed in an ultrahigh vacuum system, as shown in Figure 1.3. The laser enters in the upper left corner in the diagram, is split into two beams down the long arms, shown interrupted, and is reflected by a mirror at each end. The two beams recombine at the center and the differential arm length is sensed at the output port, circled in the diagram.

Figure 1.2: Current and planned interferometric GW detectors. The two US LIGO sites, VIRGO and GEO are in operation or in upgrade stages. KAGRA construction in Japan has begun, and will be an underground cryogenic detector. A third LIGO site is planned in India but construction has not begun at the time of this writing.

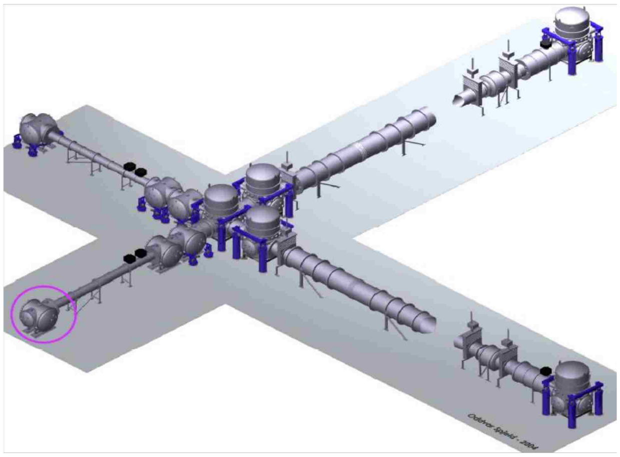

Figure 1.3: LIGO vacuum system [credit: Oddvar Spjeld]

LIGO has built two generations of instruments, initial (iLIGO) and enhanced (eLIGO) as the first, and is currently in the commissioning stage of the advanced detector setup (aLIGO), the second era. Initial LIGO ended in Oct 2007, having accomplished a one-year triple coincidence data science run (S5) between the three detectors, with a sensitivity of $\sim 10^{-19}\mathrm{m}/\sqrt{\mathrm{Hz}}$ at 100 Hz or $\sim 3\mathrm{x}10^{-23} 1/\sqrt{\mathrm{Hz}}$ in strain units. Enhanced LIGO was an intermediate step, in order to test a few of the advanced LIGO technologies and ended in Oct 2010 (known as the sixth science run, S6). Initial LIGO used a radio frequency (RF) heterodyne readout scheme, in air, with maximum input power of ~7W. Enhanced LIGO used a DC homodyne readout scheme in vacuum [17] with maximum input power of ~18W. The advanced LIGO install began after S6 ended, and is basically complete at the time of this writing. Figure 1.4 shows a timeline of the relevant LIGO milestones.

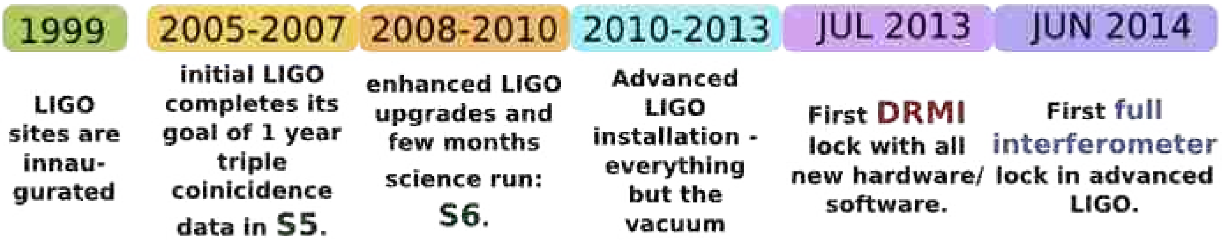

Figure 1.4: The LIGO timeline showing the initial and enhanced LIGO transition into the advanced LIGO era.

One way of measuring the sensitivity of the detector in astrophysical terms is the farthest distance at which LIGO would see a binary merger of two neutron stars, called the "range" for short. Given the geometry of the detector, not all directions give an equally strong signal, so this number is averaged over the antenna pattern of the detector shown in Figure 1.5. The neutron stars are assumed to have the standard 1.4 solar mass for this metric. Defined as such, the best range obtained in S5 was ~15 MPc [18] and in S6 was ~ 22 MPc [19].

The initial and enhanced LIGO optical configuration was as shown in Figure 1.6 and referred to as a power-recycled Michelson interferometer with Fabry-Perot recycled arms. Advanced LIGO has added another optical cavity by introducing a signal recycling mirror between the beam splitter and the readout port. These concepts will be discussed in detail in later chapters.

1.5 Dissertation Outline

The research described in this document centers around the concept of noise and the reduction of its effects on the instrument with the scope of improving the detector sensitivity and hence increasing the GW detection probability/rate. In the design of the advanced

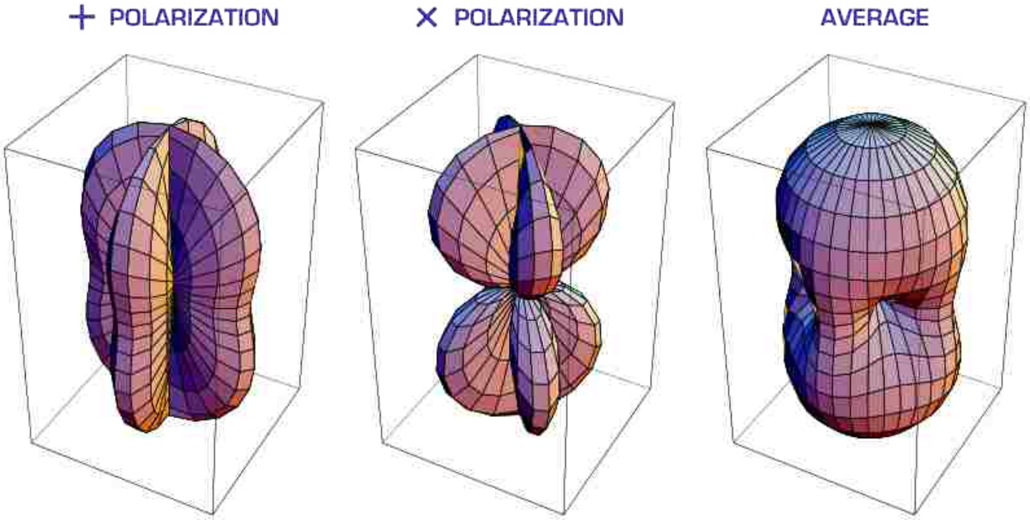

Figure 1.5: Antenna pattern of the LIGO interferometer for the two polarizations of GWs, as well as the resulting averaged antenna pattern [credit: Nelson Christensen]

LIGO detector great care was taken to properly choose the parameters of the optics, suspensions, electronics, etc such that they would not limit the detector above the three main fundamental sources discussed in Section 2.2 : quantum, thermal and seismic. However, there are many avenues for noise to sneak into such a sensitive and complex instrument, which requires intricate noise modeling to set requirements for all the components. To give a few examples related to suspensions, it is not only thermal noise and longitudinal motion that matter, but also angular noise, external magnetic coupling to the actuators and damping control noise. Such modeling has advised, for example, the size of the magnets used in the coil actuators for all stages of all suspensions.

We can categorize noise sources as external and internal to the detector. By external we could think of environmental effects, which are described in Chapter 3. By internal we could think of not-optimized parameters of the instrument which couple more noise into the GW signal than was expected. For example, if the position of a high curvature mirror is off from nominal by ∼1mm, it could cause mode-matching issues in its optical cavity or cause the buildup to be reduced. This means that during the commissioning of the detector, we have to understand (e.g. by modeling) the coupling of noise sources and

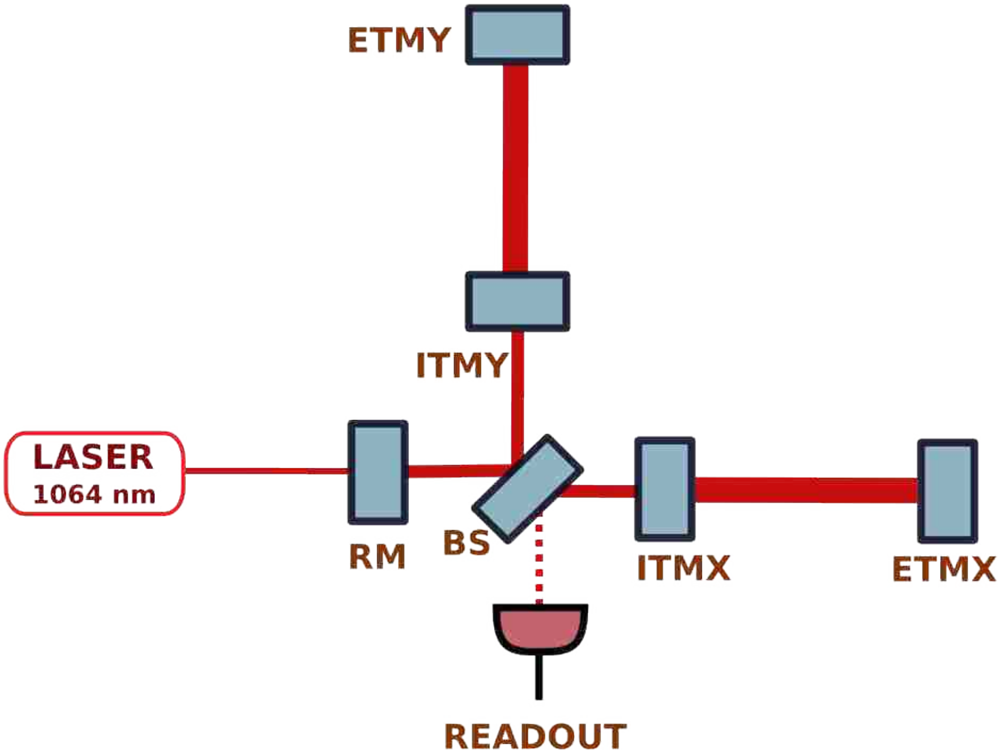

Figure 1.6: Diagram of a power-recycled Michelson interferometer with Fabry-Perot recycled arms, similar to the Initial and Enhanced LIGO optical setup. The two arm cavities are formed by an input test mass (ITM) and an end test mass (ETM), labelled X and Y. The power recycling mirror (RM or PRM) further increases the power built up inside the arm cavities. The readout of the GW signal is at the antisymmetric (AS) port, with the instrument set to be on or close to dark fringe.

measure them to confirm our expectations. Often there are unexpected issues that come up, and so early testing is essential; however, some noise sources can only be tested in very sensitive configurations because their effects are too small to be observed in other setups.

The Dual-Recycled Michelson Interferometer (DRMI) is an intermediate configuration (full interferometer without the 4km arms resonating), sensitive enough to test some noise couplings, as well as the general stability of the instrument. For reasons explained in Chapter 2, the DRMI behaves differently from the full interferometer (which translates into the quantitative couplings of various noise sources), and so additional modeling was necessary in addition to the initial modeling done in the design stage of the Advanced LIGO detector.

The chapters in this document are as follows. In Chapter 2 we introduce the details of the Advanced LIGO instrument control and optical layout, focusing on the DRMI subsystem - the main topic of this dissertation. In Chapter 3 we present a published study of environmental influences on the detector in the sixth science run of LIGO. In Chapter 4 we concentrate on the modeling of the sensing scheme for the feedback control of the resonant optical cavities of the DRMI in advanced LIGO. In Chapter 5 we show modeling and measurements of the noise sources limiting the performance of the DRMI and discuss implications for the full interferometer. In Chapter 6 we present a summary of the dissertation and conclusions related to the future performance of the Advanced LIGO detector.

CHAPTER 2
INTERFEROMETRY AND ADVANCED LIGO

2.1 Interferometric Detection of Gravitational Waves

While advanced LIGO has changed all the interferometer hardware except for the vacuum system, the optical layouts and approach to sensing and control are similar between i/eLIGO and aLIGO [20]. In this chapter we will point out the differences and similarities between these two setups as we explore the advanced LIGO detector. The LIGO interferometer is built as a combination of two main optical concepts, Michelson interferometers and Fabry-Perot resonant optical cavities.

2.1.1 The Michelson Interferometer

The main principle of GW detection with a Michelson interferometer (shown in Figure 2.1) is as follows: if a GW is propagating in a plane perpendicular to the plane of the two arms, as it passes through it will shorten one arm of the interferometer and lengthen the other. This can be observed at the anti-symmetric port of the interferometer, simplistically imagined as a shift in the fringe pattern we are accustomed to seeing on a table top interferometer; or a change in the amplitude of the power detected with a photodiode placed at the output port.

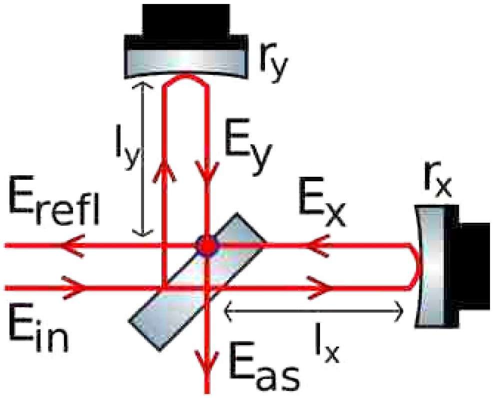

Figure 2.1: A diagram of a simple Michelson interferometer with arms denoted as X and Y, where E_{in} is the laser field entering the interferometer, E_{as} is the field at the anti-symmetric port, E_x and E_y are the fields in the arms, and E_{refl} is the reflected field.

In theory one long arm would be sufficient for the detection of a gravitational wave by observing its change in length as the wave passes by. In practice the near-dark-fringe Michelson setup further provides the essential cancellation of any common noise sources of the two arms when the beams recombine at the beam splitter. Without it, such an experiment would be dominated by the frequency and intensity noise of the laser several orders of magnitude above the desired sensitivity.

To calculate the response to a GW of a Michelson interferometer [21], we consider two equally long arms of length L and calculate the effect at the anti-symmetric (AS) port by considering the time travel difference of the light in the two arms. For an optimally oriented source:

$$\begin{aligned} \mathrm{ds}^2 = 0 &= \mathrm{g}_{\mu\nu}\mathrm{dx}^\mu \mathrm{dx}^\nu \\ &= -\mathrm{c}^2\mathrm{dt}^2 + (1 + \mathrm{h}(2\pi\mathrm{ft} - \mathbf{k}\cdot\mathbf{x}))\mathrm{dx}^2 \end{aligned}$$

$$\tau_{\mathrm{arm}} \approx \frac{1}{\mathrm{c}}\int_0^{\mathrm{L}} (1 + \frac{1}{2}\mathrm{h}(2\pi\mathrm{ft} - \mathbf{k}\cdot\mathbf{x}))\mathrm{dx} \tag{2.1}$$

Using this, we can do the return time calculation, add them to obtain the full round trip time and subtract the two arm total time. Here we make the approximation that the metric perturbation is constant over the time of light propagation in the arm. This gives the time difference of the two beams recombining at the beam splitter (BS), and hence their phase shift to each other:

$$\Delta\tau(\mathrm{t}) = \mathrm{h}(\mathrm{t})\frac{2\mathrm{L}}{\mathrm{c}} \;\text{ and }\; \Delta\phi(\mathrm{t}) = \mathrm{h}(\mathrm{t})\frac{2\mathrm{L}}{\mathrm{c}}\,\omega_{\mathrm{laser}}. \tag{2.2}$$

We can see immediately that longer arms are beneficial, up to half a wavelength of the GW. For a GW at 100 Hz, the wavelength is ~3,000 km. This is of course not practical, but is mitigated by the addition of Fabry-Perot recycling cavities in the Michelson arms, as will be explained below.

In practice we detect the laser electromagnetic field power at the anti-symmetric port (AS), so it is useful to calculate how this signal depends on the length difference of the arms (denoted $\mathrm{\Delta L}$). We also denote the mean length of the arms as l, h as the strain of a GW and k as the wavenumber for the laser.

$$\mathrm{E_{as}} = \frac{1}{\sqrt{2}}(\mathrm{E_x} + \mathrm{E_y}) \approx -\mathrm{E_{in}} \mathrm{i} e^{\mathrm{i2kl}} \sin(\mathrm{k\Delta L}) \tag{2.3}$$

A GW will have an effect only on $\mathrm{\Delta L} \rightarrow \mathrm{\Delta L} + 2\mathrm{hl}$, so the readout sees:

$$\mathrm{P_{as}} = \mid \mathrm{E_{as}} \mid^2 \approx \mathrm{P_{in}} \sin^2(\mathrm{k\Delta L} + 2\mathrm{khl}) \tag{2.4}$$

This formula shows that we cannot have exactly equal arms ($\mathrm{\Delta L} = 0$), or the resulting signal would not be first order. However, in the case of RF readout, we can introduce a macroscopic length difference in the arms while still keeping the AS port on the dark fringe (such that $\mathrm{k_{carrier}\Delta L} = \mathrm{n}\pi$ but $\mathrm{k_{sideband}\Delta L} \neq \mathrm{n}\pi$). This offset is on the order few to tens of centimeters, and is called the Schnupp asymmetry. Alternatively, if a homodyne readout is used, then a microscopic length difference offset on the order of pm-nm can be used, making the AS port slightly off dark fringe. We cannot afford to go to the center of the fringe where the signal would be perfectly linear because of the intensity noise the dark-fringe Michelson must cancel. For the full derivation refer to Appendix A.

2.1.2 Fabry-Perot Cavities and Pound-Drever-Hall Control

LIGO has introduced secondary mirrors past the beam splitter - named input mirrors - which form 4 km long Fabry-Perot cavities and recycle the light, with a finesse on the order of 150-450. It is the difference in the length of these two long optical cavities which will change with the presence of a GW signal. Furthermore, the higher the laser power in the interferometer, the larger the signal at the output port, hence a recycling mirror was introduced before the beam splitter, with a recycling factor of ∼40. These conceptual optical additions are shown in Figure 1.6.

Figure 2.2 shows a Fabry-Perot (FP) cavity formed by two mirrors, with a laser entering from one mirror. Normally, most of the light will be reflected by the first mirror and nothing will happen in between. But if the length matches an integer number of half wavelengths of the laser, then a resonant steady state of the laser field is formed and this condition is called resonance. Resonant cavities are ubiquitous in all fields of physics, and their properties and applications to interferometers are derived in many references[22][21][23].

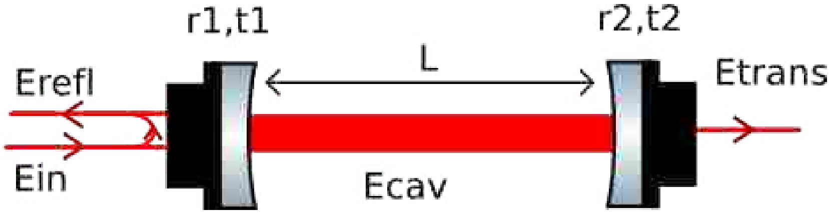

Figure 2.2: A diagram of a two mirror Fabry-Perot cavity, with mirrors denoted as 1 and 2. E_{in} is the laser field entering the cavity, E_{cav} is the field inside the cavity, E_{trans} is the transmitted field, and E_{refl} is the reflected field.

It is useful to define the finesse $\mathcal{F}$ of a cavity of length L, which depends on the field reflectivities of the two mirrors and quantifies how much power is amplified inside the cavity and how narrow the resonance is (in units of either length of the cavity or frequency of the laser). It also relates the cavity free spectral range $\Delta\nu_{\mathrm{FSR}}$ to the cavity linewidth $\delta\nu$ (also known as full width at half maximum) or to the first cavity pole p_0.

$$\mathcal{F} = \frac{\pi\sqrt{\mathrm{r}_1\mathrm{r}_2}}{1-\mathrm{r}_1\mathrm{r}_2} = \frac{\Delta\nu_{\mathrm{FSR}}}{\delta\nu} = \frac{\Delta\nu_{\mathrm{FSR}}}{2\mathrm{p}_0}, \tag{2.5}$$
$$\text{where } \Delta\nu_{\mathrm{FSR}} = \frac{\mathrm{c}}{2\mathrm{L}}.$$

For the advanced LIGO 4km arm, the power transmissions of the input test mass and end test mass are 1.48% and 5ppm respectively. This gives a finesse of roughly 420, a free spectral range of 37.5kHz, a linewidth of 90 Hz (or about 1nm in wavelength units) and a cavity pole at 45 Hz. The ratio of the power circulating inside the cavity and power incident on the cavity is simply called the buildup and is denoted as g^2. The relation to finesse differs depending whether the cavity is over-coupled or not, i.e. if $\mathrm{r}_2 > \mathrm{r}_1$[17]. If the reflectivities are equal, then the cavity is called critically-coupled, and if $\mathrm{r}_2 < \mathrm{r}_1$, the cavity is under-coupled.

$$g^2 = \frac{2}{\pi}\mathcal{F} \text{ for overcoupled cavities or}$$
$$g^2 = \frac{1}{\pi}\mathcal{F} \text{ otherwise.}$$

The reflected and transmitted fields can be expressed as below, where k is the wavenumber for the specific laser used:

$$\mathrm{E_{refl}} = \mathrm{E_{in}}\frac{\mathrm{r_1 - r_2(r_1^2 + t_1^2)e^{-2ikL}}}{\mathrm{1 - r_1 r_2 e^{-2ikL}}} \tag{2.6}$$

$$\mathrm{E_{trans}} = \mathrm{E_{in}}\frac{\mathrm{t_1 t_2 e^{-ikL}}}{\mathrm{1 - r_1 r_2 e^{-2ikL}}} \tag{2.7}$$

If we wish to control the FP cavity to keep it locked on resonance, we can actuate either on the frequency of the laser to match the length of the cavity or viceversa. But we need an error signal which can distinguish which side of the resonance the cavity is on, to know in which direction to push a mirror or the laser frequency. The power at either the transmitted or reflected port is symmetric around resonance, but the phase of the field is not. So if we can construct a relative phase measurement, we can control the cavity. The Pound-Drever-Hall method [24] accomplishes this by introducing a phase RF modulation on the main laser, usually with the choice that the resulting sidebands are anti-resonant in the cavity when the carrier is resonant. The setup is shown in Figure 2.3.

Using γ as modulation depth and ω_{m} as the modulation frequency, the modulation of the input field can be expressed as:

$$\begin{aligned}\mathrm{E_{in}} &= \mathrm{E_0 e^{i(\omega_0 t+\gamma\cos\omega_m t)}}\\ &\approx \mathrm{E_0 e^{i\omega_0 t}(J_0(\gamma)+iJ_1(\gamma)e^{i\omega_m t}+iJ_1(\gamma)e^{-i\omega_m t}-}\\ &\mathrm{-J_2(\gamma)e^{-2i\omega_m t}-J_2(\gamma)e^{2i\omega_m t}-iJ_3(\gamma)e^{-3i\omega_m t}-iJ_3(\gamma)e^{3i\omega_m t}+...).}\end{aligned} \tag{2.8}$$

By splitting the field terms as shown, we can propagate each term individually through the cavity and then add up the contributions. We can only make power measurements, so we will read the beat of some of these terms at some given frequency. For example, at DC we would detect the sum of the beat of the carrier with itself and the beat of each pair of sidebands. At $\omega_m$we would detect the beat of the carrier with each of the first order sidebands. And so on.

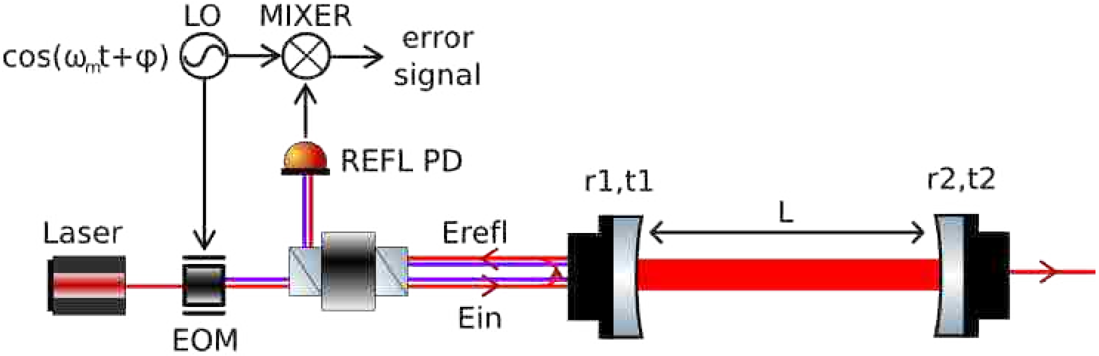

Figure 2.3: Pound-Drever-Hall method applied to a Fabry-Perot cavity to obtain the error signal for locking the cavity. The local oscillator (LO) sends the modulation to the electro-optical modulator (EOM) which creates sidebands on the laser field. Then the reflection signal is beat against the LO to obtain the demodulated audio frequency error signal to be used in a feedback loop.

If we have a Fabry-Perot cavity where the first harmonic of the sidebands is anti-resonant, then all odd harmonics will also be anti-resonant while the even harmonics will be resonant. The power in these higher order sidebands drops quickly, and so only the first few are of interest. If the first order sidebands are resonant, then the power in the second harmonic (the beat between the two first order sidebands - since we can ignore the contribution of the carrier and second order sideband beat) will tell us the power built up in the cavity. The third harmonic can be obtained by the beat of the carrier with the third harmonic sideband or by the beat of the second harmonic with the first harmonic. In the case where the first harmonic of the sideband is resonant in the cavity, it turns out that at the reflection port the dominant term is the latter. This allows for an RF control signal which is independent of the carrier and is essential to the aLIGO lock acquisition scheme. This method is referred to as“3f” locking or the Arai technique [25].

Figure 2.4 shows the PDH method applied to a Fabry-Perot cavity similar to the aLIGO arms. The lower plot shows the demodulated signal at the sideband frequency, beat with the local oscillator (the same signal which is sent to the EOM in the first place). Two signals are generated from demodulation, traditionally named I-phase and Q-phase (for in phase and in quadrature) depending on the choice of demodulating with a sine or cosine function. The demodulation phase between these signals can be rotated to translate all the relevant signal into one of the quadratures.

From Figure 2.4 we notice that for the aLIGO arms due to their high finesse, the locking signal is only linear in a very narrow length range on the order of 1nm. Therein lies the general difficulty of interferometer control. For the GW signal to be read out correctly, we rely on the arms being locked on resonance with very little power fluctuation. The differential arm residual rms motion requirement for aLIGO is 10^{-14}m [4], while the ground itself can move on the order of a few microns around 0.2 Hz.

The LIGO optical layout and controls are more intricate than the simple diagram in Figure 1.6, and here we enumerate and briefly motivate a few of the essential additional components, all of which were redesigned for advanced LIGO:

(a) a reference cavity used for frequency stabilization and an AOM/VCO setup used for intensity stabilization of the laser;

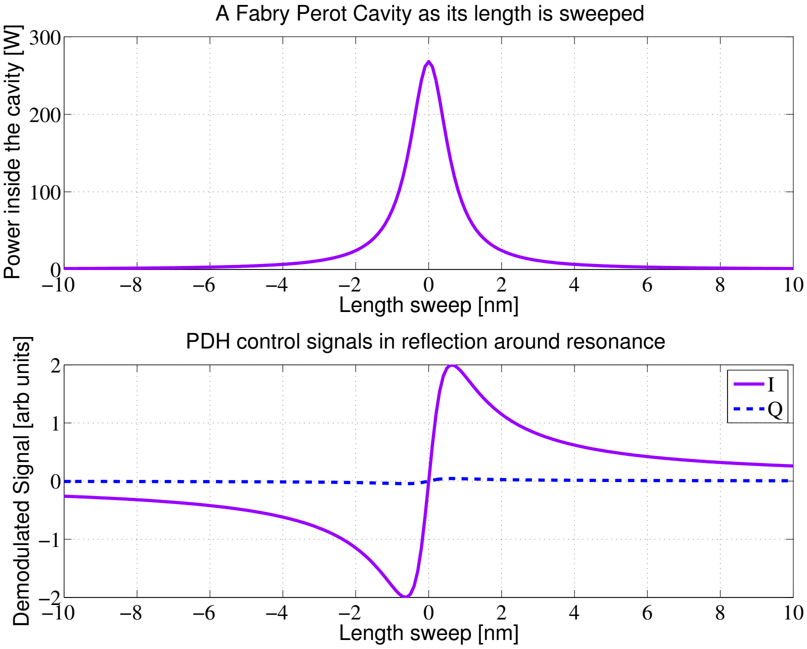

Figure 2.4: Example of PDH signals for a Fabry Perot cavity similar to the aLIGO arms, with 1W input power. Input mirror transmission of 0.0148, end mirror transmission of 5 ppm, length of 4km, laser wavelength of 1064nm and sideband modulation frequency of 45 MHz. The demodulation phase has been set to translate all length signal into the I phase.

(b) a 3 mirror cavity serving as an input mode cleaner (IMC) for further insuring that the beam into the interferometer is mostly TEM_{00}, reducing input frequency noise into the interferometer, providing input beam pointing stability and serving as a polarization filter [26];

(c) a mode matching telescope to optimize the beam size in the interferometer, addressing the issue of divergence over such a long propagation distance;

(d) the Schnupp assymetry, a slight imbalance in the two distances from the beam splitter to the input mirrors, allowing for linear signal detection at the output;

(e) an RF modulation system using the Pound-Drever-Hall method and variations thereof for locking resonant cavities;

(f) a complex digital and analog control system to maintain the detector in its linear regime, which translates to keeping all cavities locked on resonance by controlling mirror positions and frequency of the laser - this will be discussed at length in Chapter 2;

(g) an output mode cleaner (OMC), a 4 mirror cavity just before the readout, which filters out higher order modes and RF sideband noise[17];

(h) a 10 nm CO_2 laser adjusting the curvature of the input mirrors (known as the thermal compensation system - TCS), to account for the curvature distortion caused by the huge power on these mirrors when the Fabry-Perot arms are in resonance[27][28].

2.2 Advanced LIGO Upgrades

In Figure 2.5 we show the amplitude spectral density sensitivity curve for initial LIGO and enhanced LIGO side by side with the projected sensitivity curve for advanced LIGO. The goal is to obtain an average factor of 10 in sensitivity over eLIGO, which translates to 1000 in volume of space to be explored. The expected range attainable is around 200 Mpc. Population estimates, while imprecise, suggest this could lead to the detection of some 40 neutron-star binary coalescences, some 30 intermediate mass black hole binary coalescences and some 10 neutron star - black hole binary coalescences per year[20]. In addition, the increase in volume could lead to the likely detection of unmodelled bursts such as supernovae. Continuous sources such as x-ray binaries or pulsars would also benefit from increased sensitivity leading to shorter required integration time to detect their signals. As shown in Figure 2.6, there are 3 main limiting sources of noise in three different regions of the frequency spectrum of interest. The biggest improvement from initial LIGO can be seen at low frequencies, where LIGO is limited by local seismic noise, the bane of a ground based detector. At mid frequencies, both initial and advanced LIGO was/is expected to be limited by coating thermal noise. At high frequencies, the shot noise component of the quantum noise is the limiting factor. It is these three noise sources that are tackled by the aLIGO design, while ensuring that other technical noise sources which may have

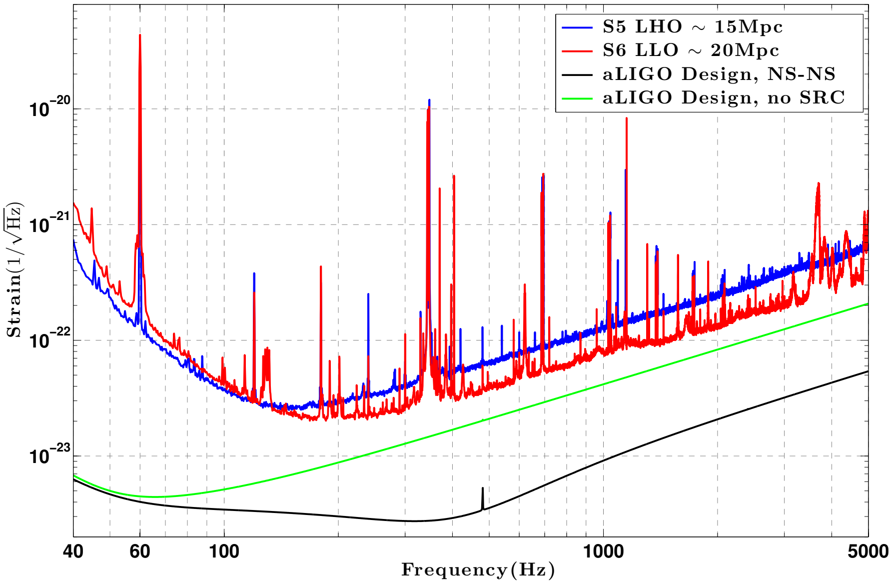

Figure 2.5: Comparison of Initial (S5), Enhanced (S6) LIGO and design Advanced LIGO sensitivity curves. The NS-NS curve for aLIGO is optimized for neutron star neutron star coalescence detection, while the "no SRC" curve is with the signal recycling cavity misaligned.

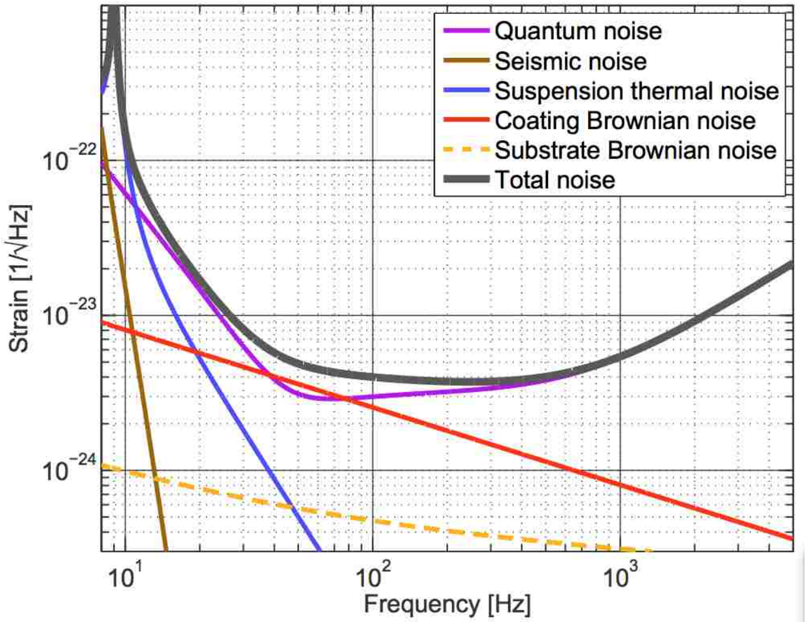

Figure 2.6: Preliminary advanced LIGO noise analysis showing the limiting noise sources, with zero detuning of SRM and 125W input power [1][2]

been borderline limiting in i/eLIGO do not hinder the achievability of the sensitivity curve formed by these fundamental (and expected) sources [4].

The advanced LIGO optical layout is shown in Figure 2.7, and will be referenced in the discussion of the advanced LIGO upgrades.

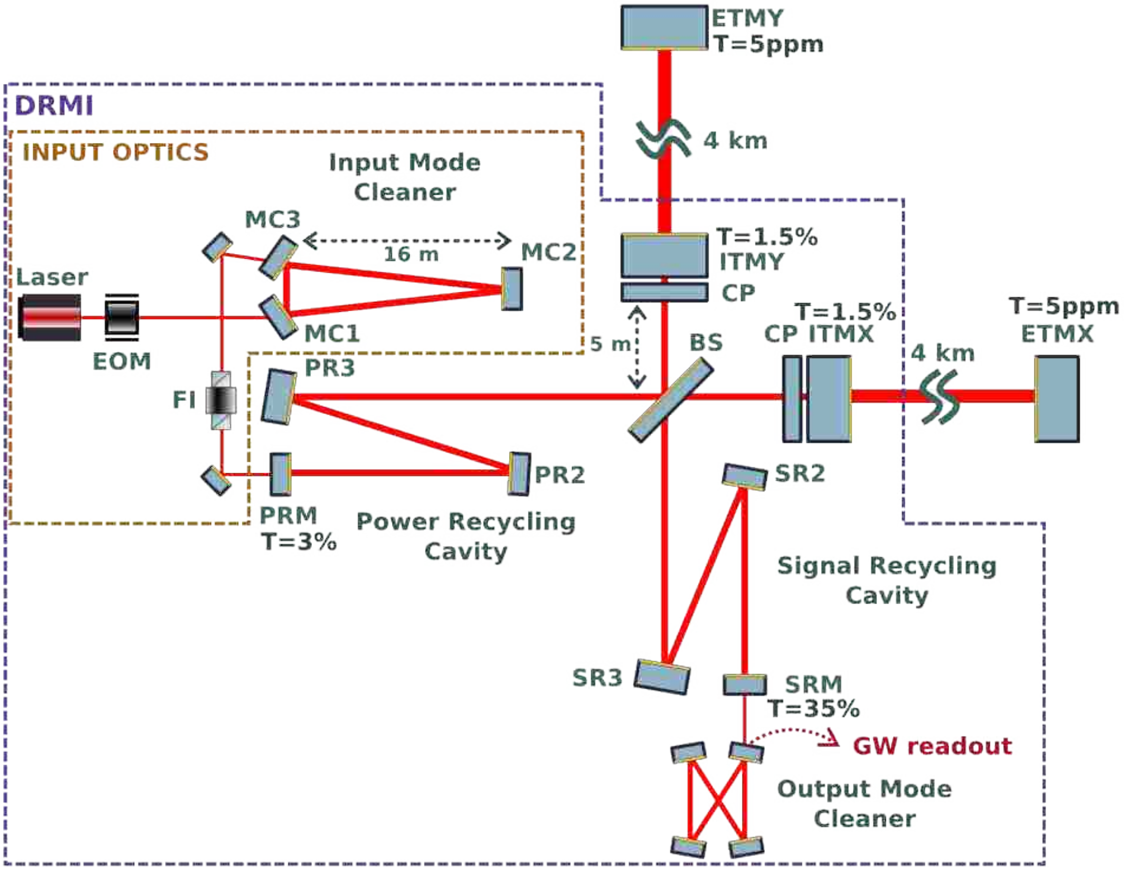

Figure 2.7: Advanced LIGO optical layout. The yellow color on optics indicates the high-reflectivity (HR) side.

2.2.1 Signal "Recycling" Cavity

The signal recycling cavity (SRC) is formed between the SRM and the input test masses (ITMs). With the increased finesse of the arms, from ∼150 in iLIGO to ∼420 in aLIGO, the differential cavity pole would be around ∼45 Hz which would then limit the sensitivity above a few hundred Hz (as can be seen through the difference of the two aLIGO design curves in Figure 2.5). The addition of the signal recycling cavity, used despite its name as a signal extraction cavity, will then raise the pole to about 415 Hz[29][22].

Furthermore, the SRM position can be tuned to change the contribution of quantum noise to the interferometer and optimize the detector for different sources, by improving sensitivity at some frequencies at the expense of others of less importance for the source of interest [30]. The design of advanced LIGO was initially with a 20% transmission optic for the SRM but was later changed to 35% to optimize sensitivity for operation at lower input power. In conjunction with this change, the Schnupp asymmetry was changed from 5cm to 8cm.

2.2.2 Stable Recycling Cavities

In i/eLIGO the power recycling cavity (PRC) was formed by one flat mirror, the PRM, and the two ITMs. Due to the PRM being a flat mirror, this caused all modes to resonate in the PRC, not just TEM_{00}. While this was not a problem for the carrier field, which was subsequently filtered by resonating in the 4km arms, the sideband field used for other controls does not resonate in the arms and hence all modes are present at the output port. For the RF heterodyne readout in iLIGO this was a problem (since the GW signal was the beat of the carrier with the sideband field). In eLIGO, the DC homodyne readout did not fully cure this problem due to the sensitivity of the OMC to alignment fluctuations which can translate higher order modes into the 00 mode [17].

Both the aLIGO PRC and SRC now have curved mirrors which only resonate the 00 mode of both carrier and the sidebands, while rejecting higher order modes. In addition, the PRC also serves as the mode-matching telescope for obtaining the large beam size required in the arms (∼5cm radius at the test masses) [31].

2.2.3 Higher Power Laser

In frequencies above ∼100 Hz, the detector sensitivity is limited by the shot noise component of the quantum noise. As laser power is increased, shot noise decreases (as $\sqrt{\mathrm{P}}$), and so the Laser Zentrum of Hannover, Germany developed an infrared Nd:Yag laser which can output close to ∼200W while meeting the aLIGO requirements for laser frequency and intensity noise[32].

2.2.4 Active Seismic Isolation Tables

The types of seismic isolation tables and suspensions in aLIGO are as shown in Figure 2.8. There are two types of chamber, the horizontal access modules (HAMs), which have horizontal mounting tables with one stage of active isolation, and beam splitter chambers (BSCs), which have two stages of active isolation and the optical tables are inverted [33] [34]. They present a vast improvement over the passive isolation of iLIGO, which would amplify motion around 20 Hz [35][36].

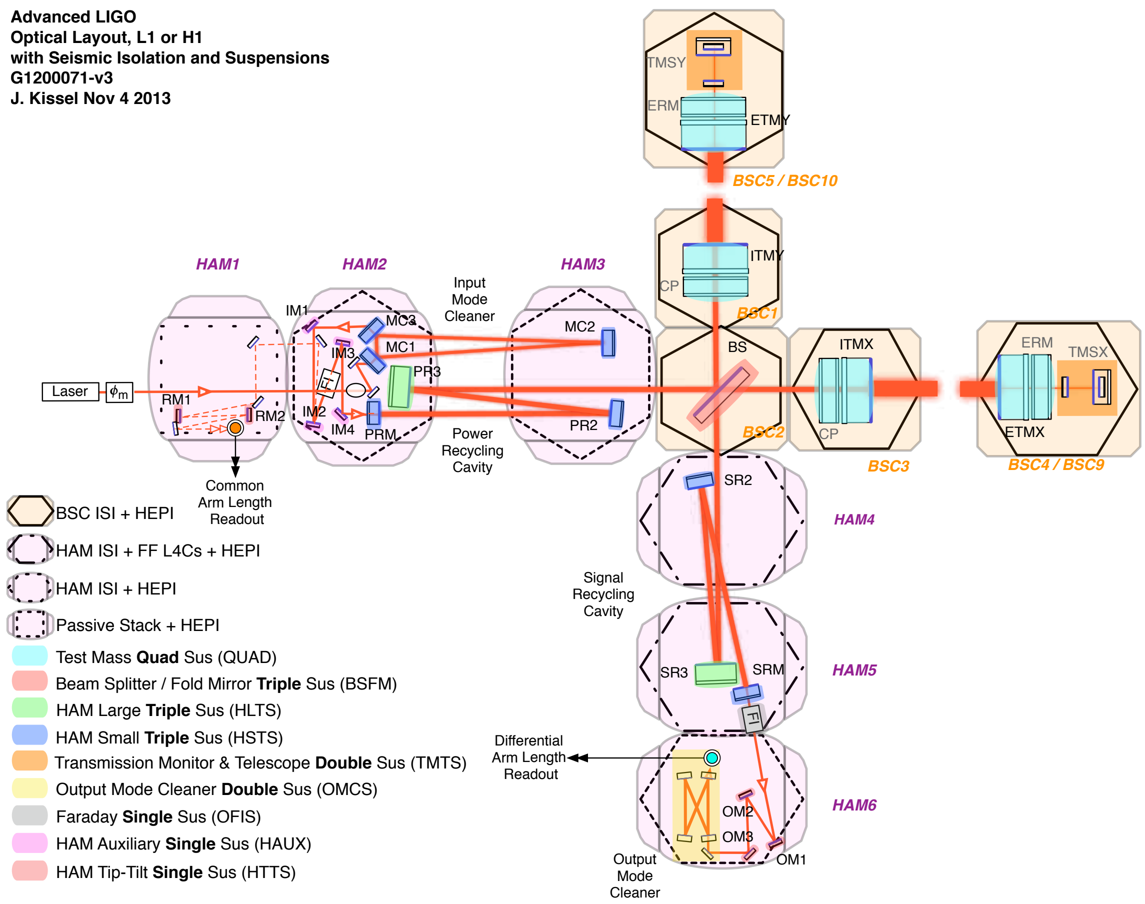

Figure 2.8: Advanced LIGO seismic isolation table and suspension types [3].

2.2.5 Multi-stage Suspensions and Larger Monolithic Test Masses

The test masses, the four mirrors forming the two arm cavities, are the most vital to isolate [37]. Their suspensions have been designed to have a quadruple stage suspension as well as a reaction mass, as shown in Figure 2.9. They are 40 kg, fused silica optics fibre welded to the fused silica mass which forms the penultimate stage of the suspension[38]. This allows the test masses to meet the suspension thermal noise requirement for the aLIGO design sensitivity, of $10^{-19}\mathrm{m}/\sqrt{\mathrm{Hz}}$ above 10 Hz in the beam direction.

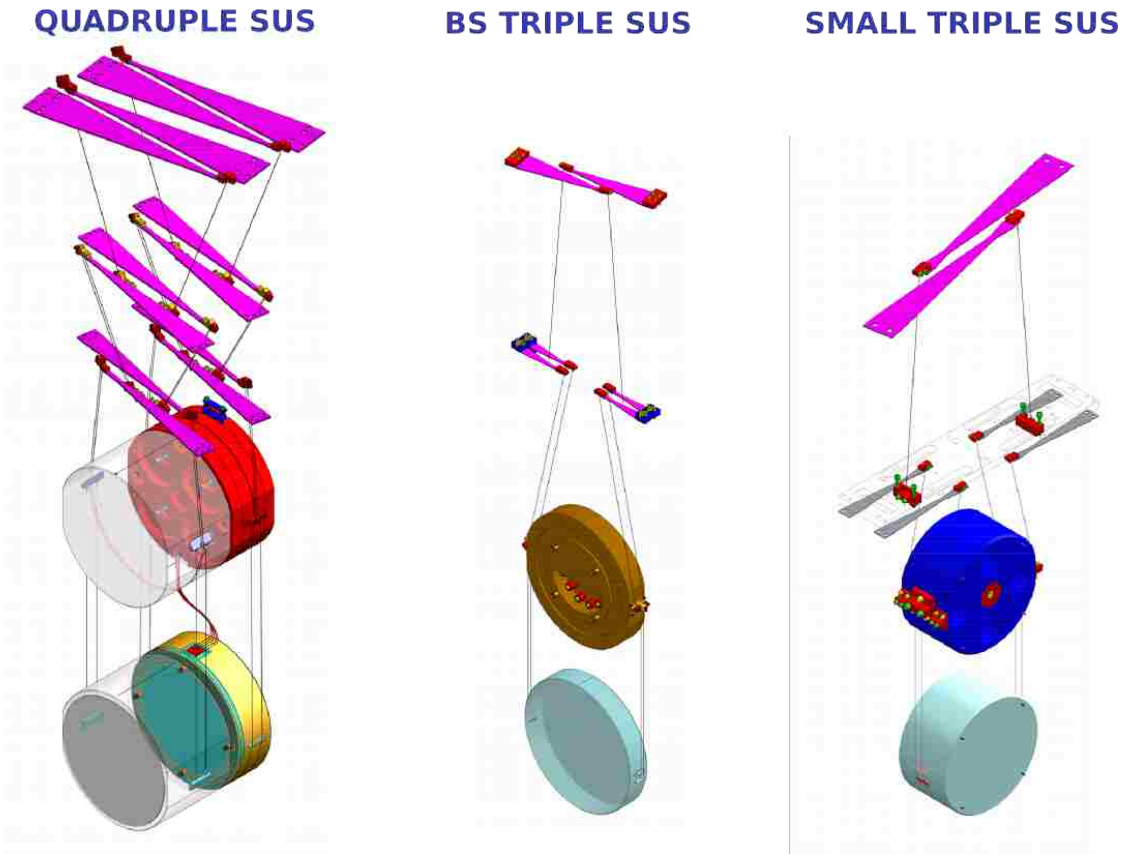

Figure 2.9: Advanced LIGO suspension mechanical drawings for three of the suspension types. The three renderings are not to scale relative to each other.

The other suspensions have been designed with fewer stages and no reaction chain, based on the requirements for their motion, as shown in Table 2.1 for longitudinal motion. Most of the main optics of the interferometer are triples, of three different types: small triple (where the optic has a mass of 2.9 kg), large triple (where the optic has a mass of 12 kg) and the beam splitter (BS) triple (which weighs 14 kg). There is also a double suspension for the OMC, as well as single suspensions for some of the auxiliary pointing optics. Figure 2.9 shows three of the main optics suspension types.

Table 2.1: Requirements by suspension type for the main optics of the interferometer, for frequencies above 10 Hz.

type	quadruple	BS triple	small triple	large triple
optic	ITMs, ETMs	BS	MCs, PRM, PR2, SRM, SR2	PR3, SR3
req.	$10^{-19}\mathrm{m}/\sqrt{\mathrm{Hz}}$	$6\mathrm{x}10^{-18}\mathrm{m}/\sqrt{\mathrm{Hz}}$	$10^{-17}\mathrm{m}/\sqrt{\mathrm{Hz}}$	$10^{-17}\mathrm{m}/\sqrt{\mathrm{Hz}}$

Each pendulum stage provides a $1/f^2$ factor of isolation from the motion of its suspension points above the resonances of the structure. Figure 2.10 shows the transfer functions (TFs) from motion of the suspension point to the motion of each stage. The slope of the isolation becomes more steep as more stages are added, resulting in an approximate total isolation of $1/f^8$. The suspension point of the structure is the seismic isolation table which provides additional motion reduction when compared to ground motion.

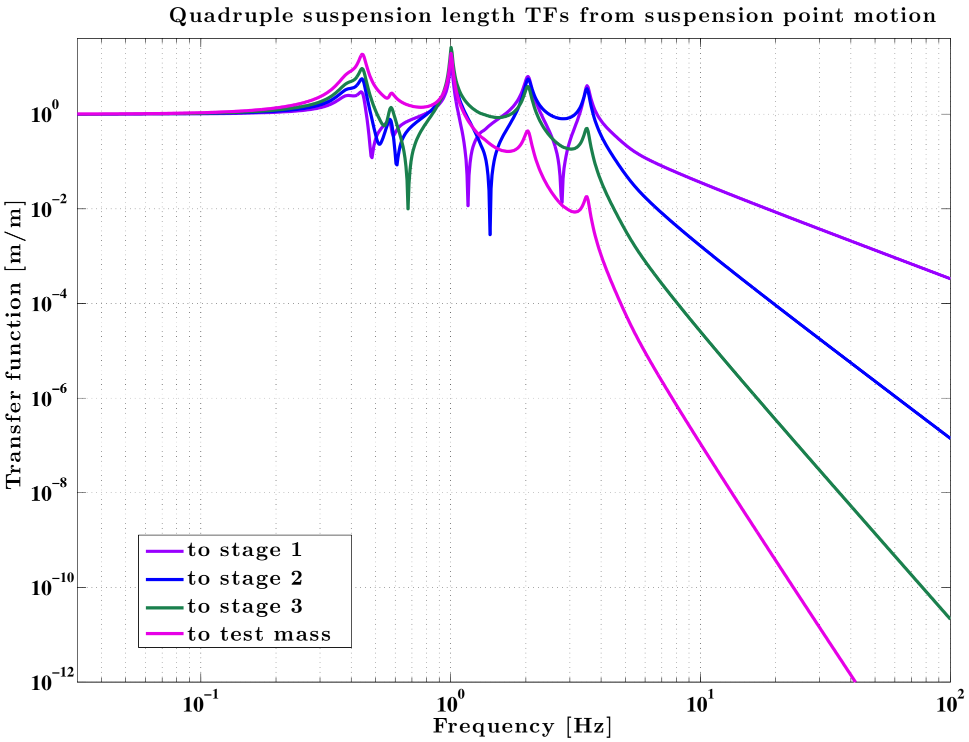

Figure 2.10: Damped transfer functions of a quadruple suspension in aLIGO for the beam direction (length) degree of freedom. The transfer functions are from motion of suspension point to the motion of each stage. Due to the low frequency resonances, by 10 Hz the motion of the optic is reduced by a factor of approximately 10 million.

Each suspension has sensors and actuators on every stage except for two cases: the quadruple suspension bottom stage which has an electrostatic drive but no sensors and the beam splitter suspension which has neither at the bottom stage. The sensor actuator combination is called an optical shadow sensor and magnetic actuator (OSEM), and aLIGO has two types: AOSEMs and BOSEMs, the latter shown in Figure 2.11. They differ in size, but their operation is the same. The coil is near a magnet glued onto the optic and by applying a current to the coil a force is applied to the magnet, pushing or pulling the mirror. On the magnet there is a small flag which enters the coil in between a small LED and a photodiode which serve as a shadow sensor. The magnets are usually glued onto the mirror in a square formation, such that the optic can be actuated in length, pitch or yaw as needed. The stages made of metal simply have magnets attached to them. The OSEMs are installed on the cage around the optic and so they read the relative motion of the suspension to its cage which is mounted to the seismic isolation platforms. The exception to this is the quadruple suspension where the two intermediate stages have their OSEMs between the main chain and the reaction chain.

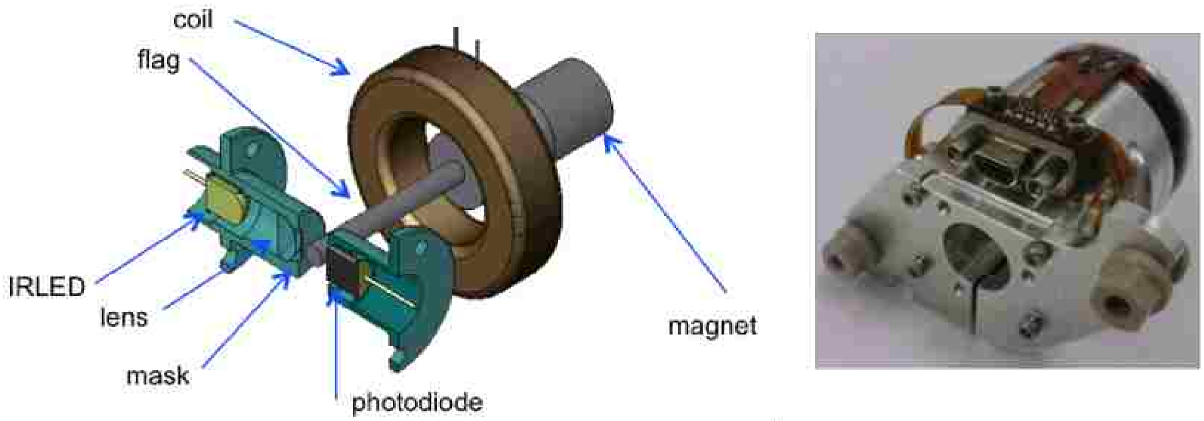

Figure 2.11: Advanced LIGO BOSEM diagram and photo.

Not all magnets are the same size, in fact they get smaller as the stages are closer to the optic. The coil drivers used for actuation are also not the same strength and get weaker as the magnets get weaker. This is due to the motion requirements in Table 2.1.

LIGO uses 18-bit digital-to-analog converters (DAC) and even if their drive is zero, they will output some bit noise. Propagating that noise through the coil driver electronics and translating to force on the magnet, it could be a limiting noise source if not chosen correctly. Furthermore, there could be ambient magnetic field coupling to the magnets themselves, a phenomenon we will discuss more in depth in Chapter 3. The stages farther from the optic can be stronger in actuation because whatever motion they impress, it will be further filtered by the pendulum of the next stages, so the requirements are proportionally less stringent on coil drivers and magnet size on higher stages.

Like any free swinging pendulum, the suspensions have various resonances in all degrees of freedom which must be damped. At the top stage of each suspension there is a configuration of six OSEMs such that all six degrees of freedom are sensed. Then the OSEMs are used to damp all degrees of freedom. The noise of the shadow sensors is on the order of a few 10^{-11}m, so some noise injection is expected from the damping loops. This is why damping is only applied at the top stage and then this damping noise is filtered by all the lower stages of suspensions. However, if strong damping is needed, even with two or three pendula isolation, this noise can be significant. In Chapter 5 we will discuss this in more detail.

2.2.6 In-vacuum Control Signals

The interferometer has to control the relative positions of all cavity forming optics, even though we are only interested in the differential length measurement of the 4km arms. The feedback controls use pick-off beams in various locations (which will be detailed in Chapter 2) to be used as the sensing signals, while actuating on the mirror suspensions. In iLIGO these signals were on optical tables in air, with little vibration isolation and one layer of acoustic enclosures. In Chapter 3 we will show that this setup would not be sufficient for acoustic and seismic coupling directly to the sensors to not limit the aLIGO sensitivity. As such, the sensing scheme and the sensors were redesigned to be in vacuum, on the same seismic isolation tables as the mirrors themselves.

2.3 Full Interferometer and DRMI Topology

The design schematic of the full interferometer is shown in Figure 2.12. The input mode cleaner is not shown. The main resonant cavities are:

- the input mode cleaner (IMC), not shown, between the laser and the PRM;
- the arms (between ITMX and ETMX, and ITMY and ETMY);
- the power recycling cavity (PRC), between the PRM and the ITMs with two folding mirrors, PR2 and PR3;
- the signal recycling cavity (SRC), between SRM and the ITMs, with two folding mirrors, SR2 and SR3;
- the output mode cleaner (OMC).

The transmission and the mass of each mirror is shown. All these mirrors' positions must be controlled to within a small fraction of the relevant cavity fringe, such that the cavities are kept on resonance and their length response is linear.

The definition of the chosen basis for the length degrees of freedom are:

- DARM = differential arm length (for the 4km arms);
- CARM = common arm length, the average length of the 4km arms;
- MICH = the Michelson length, the difference in the lengths from BS to each ITM;
- PRCL = power recycling cavity length, the average length between PRM and ITMs;
- SRCL = signal recycling cavity length, the average length between SRM and ITMs.

The red color indicates the main laser frequency (the "carrier"), which is resonant in the arms as well as in the power recycling cavity. The pink and purple indicate the two modulation frequencies used to control all degrees of freedom except DARM (which

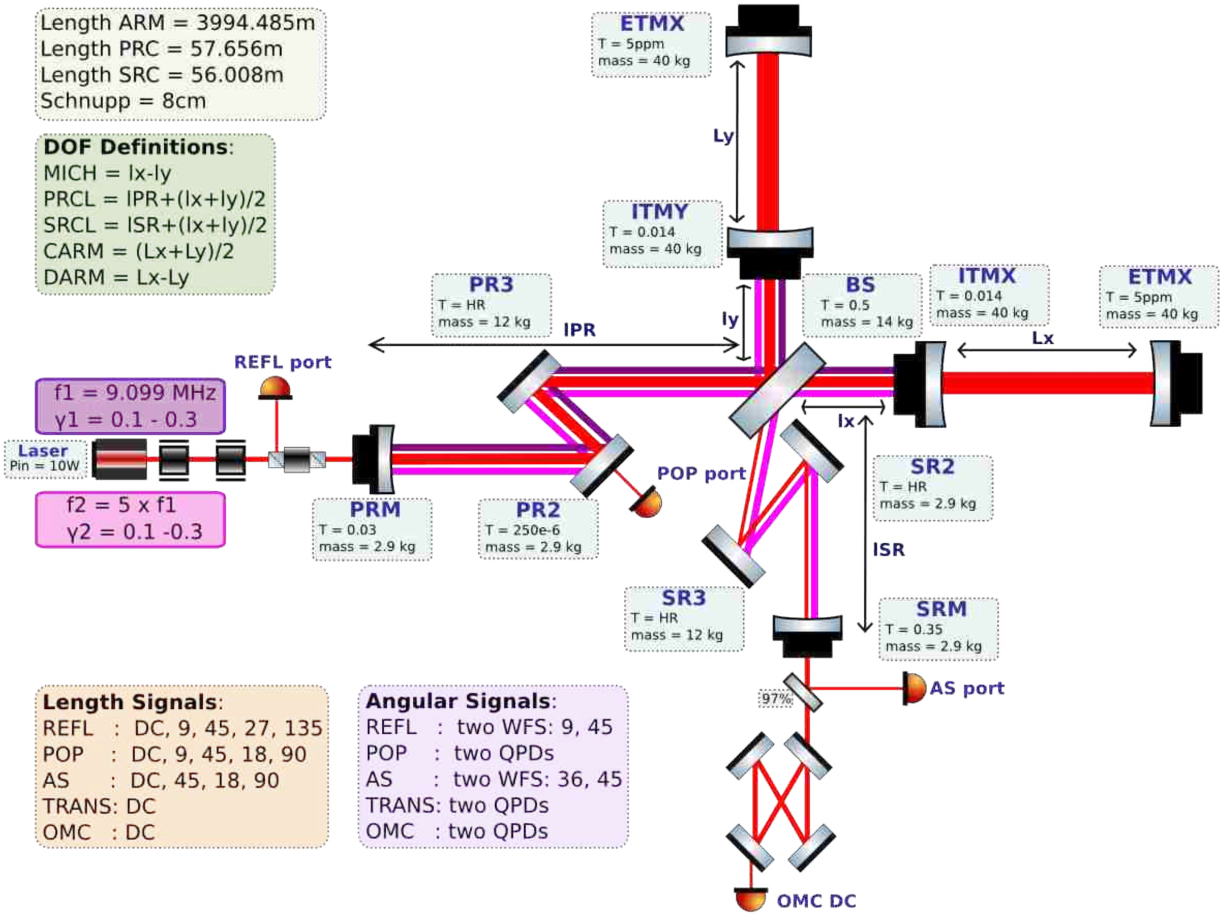

Figure 2.12: Advanced LIGO full interferometer optical layout and signal ports.

is controlled by the OMC signal, and is the gravitational wave measurement). They are multiples of each other because they are applied via an EOM before the IMC, and have to be resonant in this critically coupled cavity to reach the interferometer. The 9 MHz modulation sidebands are resonant in the PRC, while the 45 MHz modulation sidebands are resonant in both the PRC and SRC. The carrier is not resonant in the SRC, but a small DARM offset is applied to "leak" some carrier necessary for linear signal detection.

The Schnupp asymmetry is a small macroscopic difference between l_x and l_y, the distances from the BS to the two ITMs. It is necessary for signal detection, as explained in the first section of this chapter. In general, the choice for an interferometer based signal detection is to operate it on the dark fringe (no carrier light at the output port) in order to cancel out common noises to the two arms (for example frequency noise and intensity noise of the laser). For advanced LIGO, it is 8 cm and must be chosen such that the coupling of the second modulation sideband is close to critical in the dual-recycled coupled cavity (formed by the PRM, SRM and the two ITMs) in order to maximize its power in the signal recycling cavity.

The four ports used to pick-off signals and control the DOFs of the interferometer are the reflection port (REFL), the pick-off in the PRC (POP), the anti-symmetric port (AS) and the OMC transmission. The power in transmission of each arm is also recorded. The orange box in the diagram shows what length signals are available at the various ports, as well as their detection frequency. The angular signals are also shown, but are out of the scope of this dissertation.

If we remove the long arms from the full interferometer, we are left with what is called the dual-recycled Michelson interferometer (DRMI). The end mirrors can be misaligned on purpose or, as was the case for some time during the aLIGO installation, they were simply not installed yet and the vacuum system was sectioned off past the ITMs. Without the arms on resonance, the signals in the DRMI change. The carrier becomes anti-resonant in the PRC and resonant in the SRC. Only three degrees of freedom are left to be controlled: MICH, PRCL and SRCL as shown in Figure 2.13.

The difference in resonant conditions between full interferometer and DRMI showcases one of the big challenges of the aLIGO lock acquisition. It is virtually impossible to lock all five degrees of freedom at the same time, because the control signals are only linear and meaningful near resonance. This would mean that the free-swinging mirrors would have to accidentally be very close to resonance at the same time - an undesirable game of chance.

A simple idea would be to lock the DRMI and the arms separately, in sequence. But if the DRMI is locked, and the arms come into resonance, the carrier flips resonant conditions in the SRC and PRC, and so the DRMI would no longer be stably controlled. If the arms

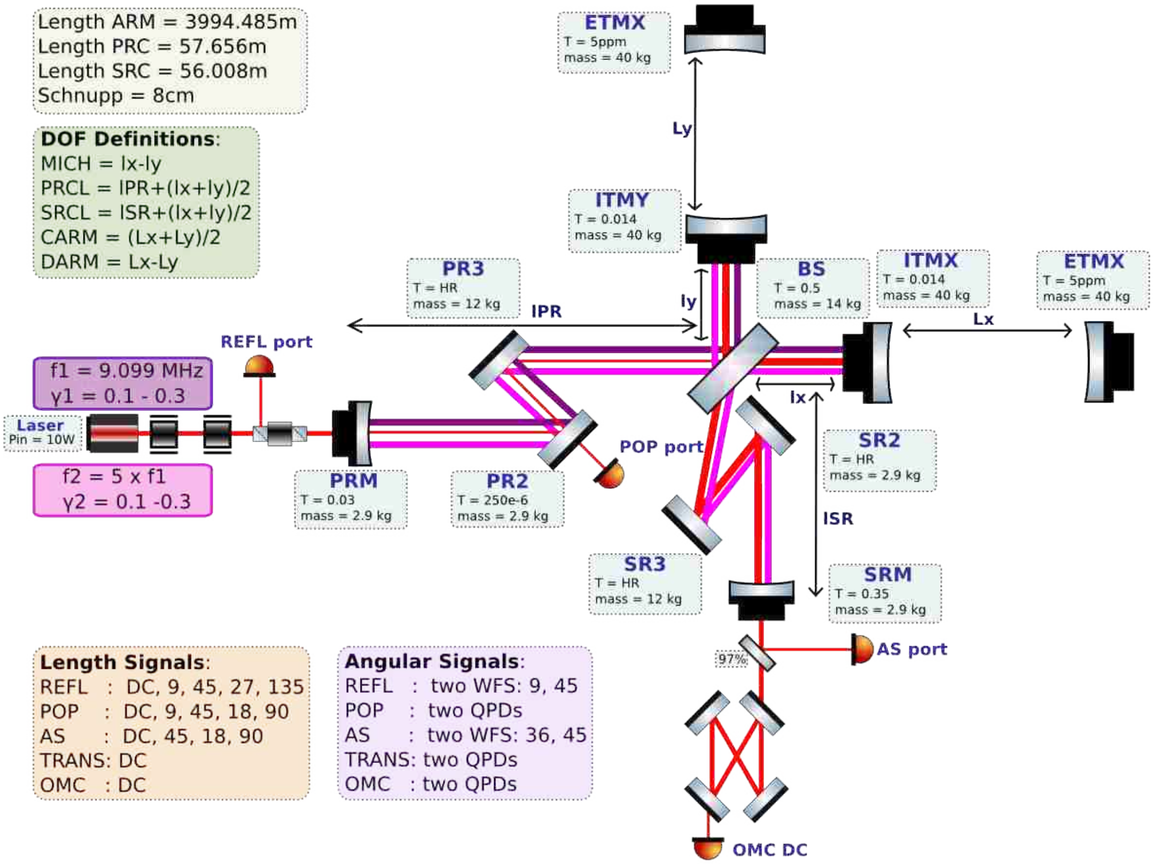

Figure 2.13: Advanced LIGO DRMI optical layout and signal ports.

are locked first, as the DRMI swings through resonance, it would disturb the arm control signals and they would lose lock.

The aLIGO locking sequence then becomes more complicated but deterministic. A set of green auxiliary lasers are used to lock the arms and then keep them off the infrared resonance. The DRMI is then locked using 3rd harmonic modulation signals, which are impervious to carrier changes, as will be explained in the following section. The arms are then brought into resonance in a controlled fashion and the DRMI is switched to more sensitive signals (further details in Chapter 4).

2.4 Length Sensing and Control

The basis for the control of optical cavities in LIGO is the Pound-Drever-Hall (PDH) technique explained in the beginning of the chapter. For the complex optical cavities of

LIGO extensive modeling was done[4] to ensure the availability of non-degenerate locking signals for all DOFs of the interferometer. Furthermore, the locking acquisition process involves temporary signals which are more stable for the various transitions which have to happen[39]. Table 2.2 shows which signals are used for which degree of freedom, both during lock acquisition and in the most sensitive state of full lock, called science mode. It also points out the actuators for each degree of freedom and the approximate unity gain frequency (UGF) of the feedback loop associated with that DOF.

Table 2.2: The various signals used for lock acquisition and science mode in the aLIGO detector. The signals are named by port, demodulation frequency and phase.

DOF	Sensor for Acquisition	Sensor for Locked	Actuator	Approx UGF
CARM	$\sqrt{TRX + TRY}$	REFL 9I	Laser frequency	10 kHz
DARM	TRX - TRY	OMC_DC	ETMX, ETMY	100 Hz
MICH	REFL 135Q	POP 45Q	BS + PR2, SR2	7-15 Hz
PRCL	REFL 27I	POP 9I	PRM	150 Hz
SRCL	REFL 135I, REFL 27I	POP 9I, POP 45I	SRM	50 Hz

2.5 Noise Sources and Full Interferometer Relevance

Dual-recycled Michelson interferometers have been studied in great detail before[40], but not with advanced LIGO hardware which allows for a different regime of sensitivity. One significant upgrade is the suspensions to be used in advanced LIGO. In initial LIGO the main optics of the interferometer (test masses and beam splitter) were suspended in a single pendulum attached to a passive seismic-isolation table made of four alternating spring-mass stages [35]. This gave the steep f^{-10} slope at low frequencies in Figure 2.5 in the blue sensitivity curve and was the limiting factor of initial LIGO at low frequencies. In advanced LIGO the seismic isolation tables are actively-controlled [36] and the test masses are suspended in a four stage pendulum, while the beam splitter is suspended by a three stage pendulum. The resonances of the pendula are much lower, allowing for the "seismic wall" to be pushed to much lower frequency. Given the very different controls of the suspensions and the different optical parameters, both the length and angular sensing and control of the interferometer was redesigned and reassessed[4, 41].

The isolation improvement can be seen in the red and black traces in Figure 2.5. As discussed in the introduction, higher sensitivity at low frequency will enable LIGO to statistically detect a wider range of sources, increasing the reach distance to binary neutron star systems by an order of magnitude (equivalent to three orders of magnitude in volume!).

In initial LIGO, the mirrors were controlled by a magnet-coil setup with a shadow sensor for reading the motion. The magnets were glued to the AR surface of each mirror. Aside from increasing the thermal noise of the mirror, there is evidence that the magnets and magnetic parts of the actuating coil created upconversion noise of seismic coupling at low frequency into the frequency band of interest possibly through the Barkhausen effect. The advanced LIGO test masses have an electrostatic drive setup. It is very weak, and so its noise cannot be tested outside of a sensitive interferometric layout.

Lastly, this configuration also tests further the performance of the input optics upgrades, as well as the new electronics and controls. It is vital that by the time the full interferometer is hardware ready, the controls have also been optimized at the same time. If the DRMI is not sufficiently robust, it is not feasible that the full interferometer will be. While the signal extraction and general feedback scheme is understood [4], as always the hard work and fun is in the fine details.

To prepare for this work it is obviously useful to model the response of the interferometer, including the control loops and all the noise sources as they couple into the interferometer GW signal. LIGO scientists have developed a Matlab extension named Optickle [42] which can calculate electric fields in a stationary optical setup including quantum noise (radiation pressure and shot noise); it has been used to design some of the advanced LIGO parameters, especially related to signal extraction. There are developments to this software to facilitate the inclusion of control loops.

The sensitivity of LIGO required to be able to detect gravitational waves brings into play a lot of hard to mitigate noise sources. A full length sensing and control noise budget has been done for the full interferometer in advanced LIGO [4], shown in Figure 2.14. My research includes doing a similar calculation for the DRMI and measuring these sources in situ. As stated before, the DRMI is the first chance to measure some of these noise sources in a sensitive enough configuration such that unforeseen issues can be addressed in a timely manner.

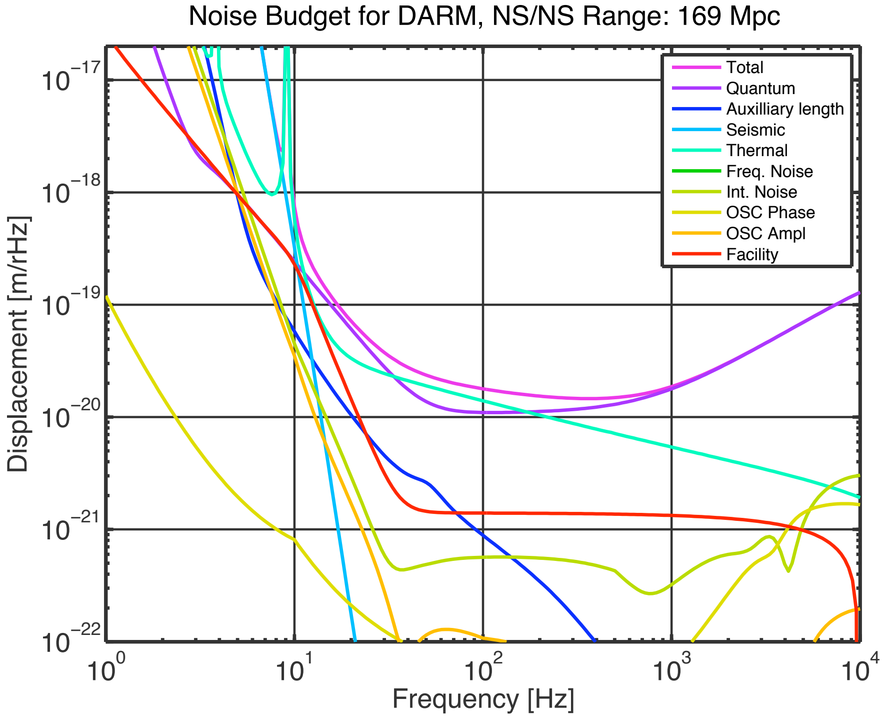

Figure 2.14: Advanced LIGO noise budget [4]

In order to illustrate how these noise sources couple into the interferometer, we can use a simple model of a power-recycled Michelson interferometer. The power at the antisymmetric port of a simple interferometer can be calculated to be approximately:

$$\mathrm{P_{AS} = P_{BS} sin^2(k\delta l)} \ \text{ with } \ \mathrm{k\delta l} \equiv \phi$$

where $\mathrm{P_{BS}}$ is the power incident on the beam splitter, or input power, k is the laser wave number, δl is the length difference and ϕ is the phase difference (of the arms). Then, adding the recycling mirror (RM), we form essentially a Fabry-Perot (FP) cavity between the RM and the simple Michelson, whose response is simply:

$$\mathrm{P_{AS}} = \mathrm{GP_{in}sin^2(k\delta l)} \left(1 + \mathrm{i}\frac{\mathrm{f}}{\mathrm{f_{cav}}}\right)^{-1} \tag{2.9}$$

where G is the recycling gain and $\mathrm{f_{cav}}$ is the cavity pole. r and t are the field reflectivity and transmission respectively. In general, for input mirror 1 and output mirror 2 of an FP cavity of length L:

$$\mathrm{G} = \frac{\mathrm{t_1^2}}{(1 - \mathrm{r_1 r_2})^2} \quad \text{and} \quad \omega_{\mathrm{cav}} = \frac{1 - \mathrm{r_1 r_2}}{\mathrm{r_1 r_2} \frac{\mathrm{L}}{\mathrm{c}}}.$$

Using the advanced LIGO parameters [4] we obtain a recycling gain of 60 and a cavity pole at 18 kHz. Given that the GW channel is only recorded at 16kHz, so we can only analyze up to Nyquist frequency of 8kHz, we can ignore this pole for the purposes of the DRMI and consider sensor responses to length changes (in units of Watt/meter) to be flat in frequency. When doing the more complex calculation for the full interferometer, the differential cavity pole will not be ignorable (in Figure 2.14 it is what causes the upward slope above 400Hz in the quantum noise curve) and can be changed by tuning the SRC.

What is important is the sensitivity to changes in the phase:

$$\frac{\mathrm{dP_{AS}}}{\mathrm{d}\phi} = 2\mathrm{GP_{in}}\sin(\phi)\cos(\phi) \tag{2.10}$$

Hence we have a linear readout with respect to changes in the differential phase of the light for very small offsets from the dark fringe, as explained in section 2.1.

2.5.1 Seismic Noise

In order to calculate its contribution, we must know the transfer functions from ground to test mass. In the advanced LIGO case, this includes the hydraulic seismic isolation for the vacuum chambers, the seismic tables and the suspensions. Then, using seismometer signals, we can compute the noise it would add to the sensitivity curve. This would be an involved calculation, so we can simply take the seismometer signals present on all stages of the seismic suspension and only have to propagate through the suspension transfer functions which have been well modeled. Seismic noise couples directly to the length measurement by moving the test masses.

At higher frequencies we can consider the different chambers as having uncorrelated noise and so we can add them in quadrature. At lower frequencies, the motion is mostly common, if the arms are left out. In the full interferometer there is a servo implemented to account for very low frequency tidal motion due to the Moon and Sun, which cannot be ignored on the scale of a few kilometers. For example, in initial LIGO, the interferometers could not stay locked on resonance for longer than a few hours before the servo was implemented.

2.5.2 Laser Frequency and Amplitude Noise

One of the main reasons to use an interferometer for GW detection as opposed to a simple length measurement is the influence of laser frequency and amplitude noise. In a Michelson setup aligned to be on the dark fringe frequency and amplitude noise is common to both arms and can be sensed at the symmetric port and attenuated by feedback. Of course, in reality, the arms are not perfectly identical, and there is some coupling outside of what this “common mode” servo can accomplish. In DC readout, a small offset (a few pm) is introduced between the arm lengths, to allow some carrier light at the AS port. This causes the laser intensity noise to couple in directly into the $\mathrm{P_{in}}$ factor. Frequency noise is not directly distinguishable from length noise; it shows up directly in the phase which is related to the wave number $\phi = \mathrm{k}\delta\mathrm{l} = 2\pi\omega/\mathrm{c}$.

2.5.3 Quantum Noise

Quantum noise is comprised in two effects, shot noise and radiation pressure noise. Shot noise is due to the quantized nature of photons, and is white. It simply depends on the power incident on the beam splitter, in the PRMI case this being $\mathrm{P_{BS}} = \mathrm{G\ P_{in}}$ [43]:

$$\delta\mathrm{P_{shot}} = \sqrt{\frac{2\mathrm{hc}}{\lambda}\mathrm{P_{BS}}\sin^2(\mathrm{k}\delta\mathrm{l})}. \tag{2.11}$$

This shows that shot noise is white but its effect will not be white in the full interferometer due to the coupled cavity pole.

Radiation pressure noise comes from two sources, one called technical radiation pressure and one quantum radiation pressure. Technical radiation pressure noise is caused by input power fluctuations which propagate to the output through imbalances in the mirror masses, reflectivities, arm cavity buildups, etc. It can be thought of as the fluctuation of the force exerted on each mirror by the photons which hit it discretely [21]. This force can be written in terms of the power of the incident field: $\mathrm{F} = \frac{\mathrm{P}}{\mathrm{c}}$ which gives a motion spectrum:

$$\mathrm{x(f)} = \frac{1}{\mathrm{m}(2\pi\mathrm{f})^2}\mathrm{F(f)} = \frac{1}{\mathrm{mf}^2}\sqrt{\frac{\hbar\mathrm{P_{in}}}{8\pi^3\mathrm{c}\lambda}}. \tag{2.12}$$

Radiation pressure noise is not white, but goes as f^{-2}. At low frequencies it will dominate the quantum noise spectrum, while at high frequencies, shot noise will take over.

2.5.4 Thermal Noise

Thermal noise comes from two main sources: the optic itself (especially the coatings which have ∼1000 times the loss compared to the optic) and the suspension wires [44]. In general, the noise introduced by thermal noise can be written as[43]:

$$\mathrm{S_x(f)} = \frac{\mathrm{k_B T}}{\pi^2 \mathrm{f}^2}\mathrm{Re[Y(f)]} \quad \text{with} \quad \text{admittance} \tag{2.13}$$

$$\mathrm{Y(f)} = \frac{\mathrm{v(f)}}{\mathrm{F_{therm}}} = \mathrm{i}\frac{2\pi \mathrm{fx(f)}}{\mathrm{F_{therm}}},$$

where v(f) is the velocity and $\mathrm{F_{therm}}$ is the thermal drive force. This force would be real if there were no losses in the material, and then Y(f) would be perfectly imaginary and $\mathrm{S_x(f)}$ would be close to zero. Fused silica is used for the LIGO test masses because it has very low losses. In advanced LIGO, the suspension wires are also made of fused silica.

There are other noise sources to consider. Newtonian noise caused by local accelerating (vibrating) masses in the detector buildings and residual gas pressure in the vacuum system are usually referred to as facility noise. There are several types of electronics noise, dealing with readout electronics (e.g. the dark noise of the photodiodes) and digital to analog, analog to digital conversions. Because the interferometer has to be kept locked on resonance to have a linear response, the control system will propagate and interlace these sources. Even though LIGO has used and will use DC readout, the RF modulation system is still needed to align, lock and stabilize the interferometer. Hence, the modulator amplitude and phase noise will be propagated into the interferometer control system and eventually the readout.

We have presented the enhanced and advanced LIGO detector configurations and detection schemes. In Chapter 3 we will present measurements done during enhanced LIGO to quantify the effects of environmental noise sources (e.g. acoustic, magnetic, etc). In Chapter 4 we will present models and measurements related to the advanced LIGO length sensing and its effects on the detector. Finally, in Chapter 5, we will present models and measurements related to quantifying the contribution of various noise sources to the detector background - known as noise budgeting.

CHAPTER 3
STUDIES OF ENVIRONMENTAL EFFECTS ON THE LIGO DETECTORS IN THE SIXTH SCIENCE RUN

This chapter is an article published in the Classical and Quantum Gravity journal for which I am first author. The first few paragraphs containing a general introduction to LIGO were removed. The full text of the paper can be found in reference [45]. The permissions regarding the publication of these results as part of this dissertation are found in Appendix B.

3.1 Introduction

The LIGO detectors have been carefully isolated from external non-astrophysical influences. Nevertheless, environmental disturbances can cause temporary or stationary contamination of the readout signal and reduce the sensitivity of the detector.

For this reason, the LIGO instruments are equipped with dedicated sensors to detect environmental noise such as seismic, acoustic, magnetic or radio frequency electromagnetic disturbances. Typically these sensors are referenced to the DARM signal by creating or simulating environmental excitations large enough to be measured by both the environmental sensors and the DARM. The sensors provide critical information for the search of potential astrophysical events as well as for making the LIGO detectors less prone to environmental noise coupling.

Firstly, environmental sensors are used to validate astrophysical events by vetoing false positive GW signals [46]. We must show that any candidate GW signal is extremely unlikely to have been produced by some environmental disturbance randomly coincident at both sites, or by a large scale effects affecting both detectors. During S6 (and before), for unmodeled burst searches,random coincident event triggers were frequent enough to be of concern.

Furthermore, we assess the level of the background environmental noise with respect to contaminating the DARM signal, typically in narrow frequency bands. Once the source and coupling mechanism is determined, we need to either remove the noise sources (e.g. shut down loud fans), attenuate the signal that propagates from the source to the coupling point on the detector (e.g. enclose the sensitive part of the detector in an isolation enclosure), or reduce the coupling at the detector (e.g. increase the size of the optics to avoid beam clipping). If we find a particularly high coupling location, we then add further monitors or relocate existing ones in order to ensure full validation of candidate astrophysical signals.

In this paper we describe the main environmental influences, their effect on the detector and present a subset of studies representative of the efforts [47] to reduce the environmental noise contribution to the detectors' background. In Section 3.2 we categorize the environmental influences by their coupling mechanisms into seismic, acoustic, audio frequency magnetic and radio frequency electromagnetic effects. For each class we discuss the possible sources, general mitigation approaches and the influence on the detector. In Section 3.3 we show a set of studies performed in S6 characterizing each of these categories. In Section 3.4 we discuss the results of the studies, how these methods will be used in the future and the implications for the more sensitive Advanced LIGO detectors.

3.2 Characterizing the Detectors' Physical Environment

The main categories of environmental influences on the detectors are seismic, acoustic and magnetic/electromagnetic field disturbances. We use accelerometers and seismometers to measure seismic motion, microphones to measure acoustic noise, magnetometers to measure audio frequency magnetic fields, radio receivers to track RF fields, temperature sensors to track temperature changes and voltage monitors to track the voltage of the electric power supplied to the site. Table 3.1 shows the details of some of the sensor types used in the LIGO Physical Environmental Monitoring (PEM) sub-system. For seismic effects we use two different types of sensors, seismometers (sensing velocity at low frequencies)and accelerometers (sensing acceleration at higher frequencies than seismometers) in order to cover a wider frequency range.

Table 3.1: Important PEM sensor types and the frequency ranges in which they are used. The frequency range is a combination of sensor calibration range from the manufacturer and the sampling rate at which they are recorded. The noise floor is the larger of the quote from the manufacturer for that sensor or the analog-to-digital conversion noise in the signal acquisition.

Type	Sensor	Operating freq.	Sampling freq.	Noise floor
seismometer	Guralp CMG-3T	0.1-20 Hz	256 Hz	20 pm/s
accelerometer	Wilcoxon 731-207	1-900 Hz	2048 Hz	20 μm/s^2
microphone	Brüel&Kjaer 4130	10-900 Hz	2048 Hz	20 μPa
magnetometer	Bartington 03CES100	0-900 Hz	2048 Hz	10 pT
radio station	AOR AR5000A	24.5 MHz	2048 Hz	5 μV

Figure 3.1 shows the PEM sensor number and locations in S6 at LLO (with a similar setup at LHO). The reflection (REFL) table, the anti-symmetric (AS) table, the laser table and the transmission (TRANS) tables are not in vacuum and contain important feedback sensors for interferometer control.

LIGO is designed to not be dominated by environmental noise at frequencies higher than approximately 50 Hz, the frequency band of interest for GW in initial LIGO. Most control systems of the interferometer must operate at low frequencies and can become unstable due to large environmental disturbances. If these disturbances are too large, the interferometer will not be operational because optical cavities cannot be kept on resonance due to limited dynamic range (i.e. the detector is not "locked"). The interferometer is a gravitational wave detector only in its linear operating regime, i.e. when all optical cavities are stably locked near resonance for long periods of time [48].

There are several ways in which environmental noise can couple into the detector readout. The most significant ways are: changing the length of optical cavities, causing laser beam jitter, modulating the path length of scattered light which then recombines with the main laser beam, and introducing frequency noise. However, environmental effects are often non-linear and cannot be removed offline in data processing.

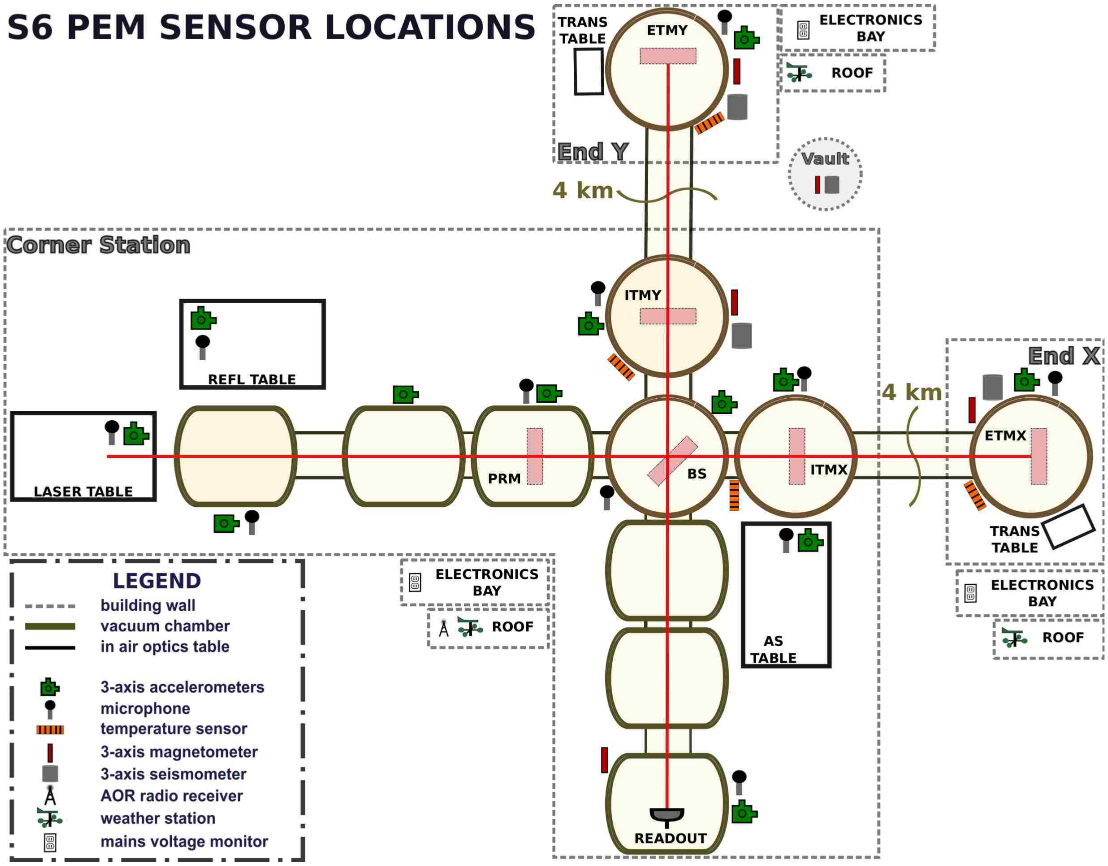

Figure 3.1: The Physical Environmental Monitoring (PEM) system layout at the LIGO Livingston detector during S6. The setup for LIGO Hanford was very similar. Shaded regions indicate the vacuum enclosure. Circles and rectangles indicate vacuum chambers where mirrors were suspended. Optical tables were surrounded by acoustic enclosures but were not in vacuum.

3.2.1 Seismic Influences

LIGO seismic isolation systems very efficiently reduce noise above 10 Hz, but amplify noise at the resonances of the mass-spring isolation stages. Feedback control systems keep the Fabry-Perot cavities locked on resonance, and low frequency seismic motion is the main contributor to the length and angular control signals. Moreover, large relative motion between mirrors in-vacuum suspended and out of vacuum sensing photodiodes can generate large control signals, which can cause upconversion [49].

The calibrated detector noise shows a steeply descending curve at low frequencies, called the “seismic wall”, due to the residual seismic noise attenuation by suspensions and seismic isolation, following roughly a slope of f^{-10} due to the five layers of isolation of the main optics [50].

Transient sources of seismic motion include earthquakes, winds, ground and air traffic. The two detectors in Livingston, LA and Hanford, WA have different seismic backgrounds due to the very different geological structure of their locations [51].

Distant earthquakes produce ground motion with frequencies of 0.03 to 0.1 Hz, and even higher the closer the epicenter is to the detector. The interferometer seismic isolation is largely ineffective at these low frequencies, and many times the detector cannot remain locked. In Figure 3.2 the "earthquake" curve shows the amplitude spectral density of a local seismometer signal during a 5.9 magnitude earthquake near Peru, with a peak around 0.05 Hz. Winds higher than 10-20 miles/hour will cause the buildings to sway enough to affect the detector output, even to the point where the detectors cannot remain locked. The effect of wind shows up mostly in the 0.5-15 Hz frequency range, but also as building tilt at lower frequencies.

Vehicular traffic at highway speeds produce ground motion in the 2-15 Hz band (depending on axel spacing and speed) and distant human activities produce motion in the 1-3Hz range. Because the sources are anthropogenic, there is a large difference between day and night in these bands at both sites, despite their location away from cities. Other sources can show up in this frequency range as well, for example dam operations, forest logging or large scale construction.

Another source of seismic noise for the interferometers is storms in the oceans resulting in low frequency peaks generally highest at twice the wave propagation frequency, which called "microseism peaks" [52]. These are seen in the range of 0.07 to 0.7 Hz and couple directly to detector motion. All traces in Figure 3.2 show this peak around 0.15 Hz, but the one labelled "microseism" showcases a particularly high motion instance caused by storms in the Gulf of Mexico and detected in seismometers at LLO. This effect is always present, but may vary by up to two orders of magnitude on the time scale of a few days.

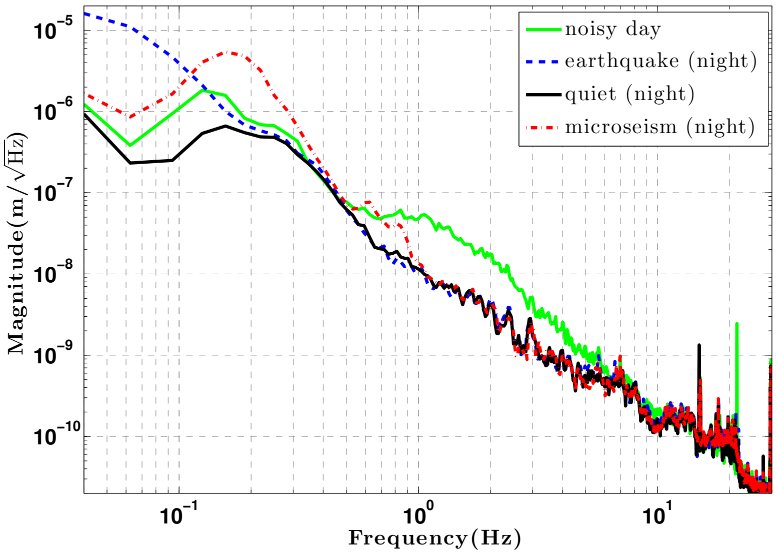

Figure 3.2: The LIGO Livingston Observatory (LLO) seismic background in different representative conditions, as seen by the horizontal axis of a seismometer located in the corner building. The "microseism" trace shows an instance where the oceanic microseism peak around 0.15 Hz was larger than average. The"noisy day" trace shows the effect of strong, nearby seismic disturbances due to human activity, in this particular case timber logging a few miles away from the detector. The "earthquake" trace shows an increased amplitude of seismic motion at very low frequency typical when large, far-away earthquakes occur. The "quiet" spectrum shows an instance of some of the quietest seismic environment we can expect.

Predictably, at LHO the Pacific storms have a larger influence. As with earthquakes, at these low frequencies there is little seismic attenuation, hence the motion couples directly to the detector's control systems. The seismometer signals were used to create a feedforward servo to reduce the coupling of seismic noise in this frequency band to the GW signal, with best results obtained mid-S6 when the coupling was reduced by a factor of 5 at the microseism with an overall RMS reduction factor of 2 on the DARM signal [49].

Because the detectors have 4 km long arms and operate nearly continuously during science runs, earth tides caused by the gravitational pull of the Moon and Sun cause significant changes in the distance between the optics which would exceed the actuator range on the mirrors on a time scale of a few hours. To correct for this, the detectors have a tidal feedforward system which adjusts the position of the chambers or the laser frequency; it is based on tidal predictions calculated from the position of the Sun and Moon with respect to the detectors.

The previously described sources cannot be removed, so we reduce their coupling into the detector, e.g. by seismic feed-forward. A notable exception was the repaving of the main highway near the LHO site, which reduced truck traffic coupling into the detector by about a factor of two. Further, we characterize them well enough to be able to veto transients seen in the GW channel as non-astrophysical signals in our analyses [53].

There are also sources of vibration local to each observatory building such as motors, the air conditioning system, chillers and pumps, which cause seismic motion and disturb the detector's output. Many such sources have been localized and mitigated either by seismically isolating them on springs or changing their operation.

3.2.2 Acoustic Influences

Acoustic influences refer to sound waves propagating through air and vibrating components of the detector. Some known sources are electronics fans (above 50 Hz), chillers (below 60 Hz), building air control (below 100 Hz), thermally induced building creeks and thumps (broad band), nearby vehicles (50 - 150 Hz), and wind (broad band) [47]. Propeller driven aircraft produce acoustic vibration in the range of 50-100 Hz if they fly close to the detector. A software monitor using data from microphones is used to veto such events seen in the GW channel [54]. Figure 3.3 shows ambient normal spectra of the microphones in the corner station at each site.

The in-vacuum systems of the interferometer including the photodiodes which read the GW signal are isolated to various degrees from direct acoustic wave propagation. However, several auxiliary systems are not in vacuum (see optical tables in Figure 3.1) and have been found to be the major sources of coupling acoustic noise into the readout of the detector. For this reason, all out of vacuum optical tables have been acoustically insulated with enclosures in order to minimize the propagation of acoustic noise.

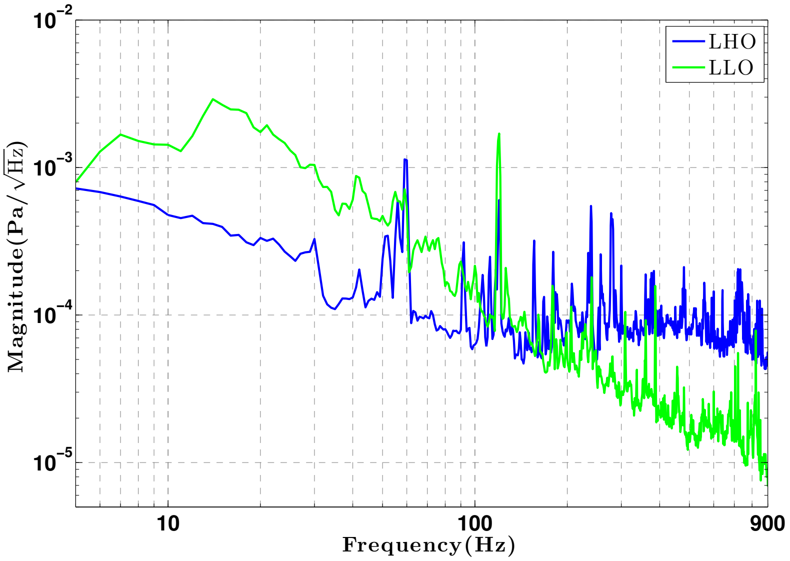

Figure 3.3: Representative microphone spectra in the corner station at both sites, showing the acoustic background for the detector. At low frequency LHO has lower ambient acoustic noise due to extra insulation on the air conditioning system (to lower acoustic correlations between the previously present two colocated Hanford detectors). At high frequency LHO has a higher ambient acoustic noise due to the electronics racks which are in the same room as the detector, while at LLO the electronics racks are in a separate location. For Advanced LIGO the electronics will also be removed from the detector space at LHO.

Furthermore, acoustic noise can vibrate the outer suspension points of the in-vacuum system which then couples to high-frequency resonances of the seismic isolation. This effect has to be taken into account for auxiliary in-vacuum optics, especially those pertaining to the readout port.

Acoustic noise has been found to couple primarily through beam jitter, beam clipping or scattering, all of which transform acoustically driven motion of the optical mounts into modulations on the primary and auxiliary photodiode signals. We have taken careful measures to reduce scatter, such as checking all optical surfaces for stray beams, using beam dumps for all stray light, removing not-needed protection windows from all photodiodes to prevent sensor prompt-reflection backscatter, setting lenses at an angle and using damping material on optical mounts.

3.2.3 Magnetic Influences

Magnetic noise sources relevant for LIGO are all of electric origin, such as building heaters, large motors, lights or relatively near-by high-voltage power lines up to 4km away from the site. These peaks are not stationary in frequency or amplitude, so they create noise in a wider frequency range than just a narrow peak at the respective frequency. Furthermore, since the 60 Hz harmonics from AC power lines are large in the GW signal as well as some of the control signals, other narrow-frequency peaks in the region of 0.1 to 10 Hz which are not in the LIGO frequency band of interest can modulate the GW signal producing sidebands around large peaks like the 60 Hz harmonics. Figure 3.4 shows the ambient spectra of the magnetic background for the LIGO detectors in S6 in the corner station.

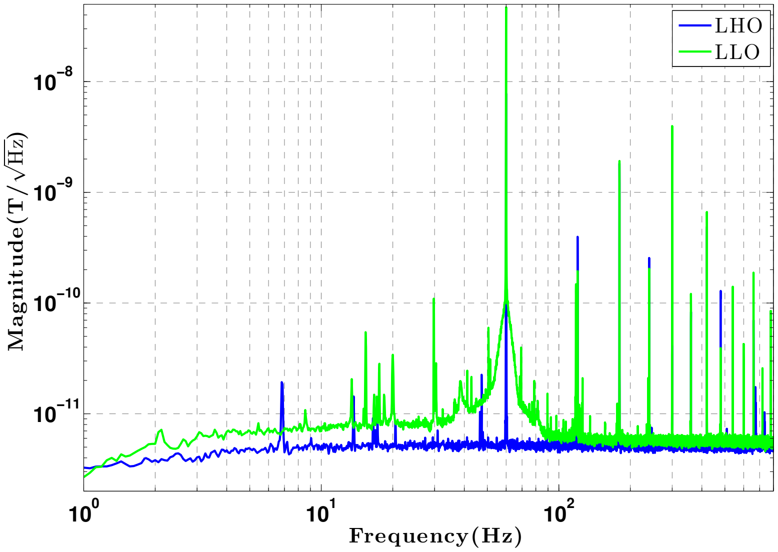

Figure 3.4: Representative magnetometer spectra in the corner station at both sites, showing the magnetic background for the detectors. The Livingston detector has a higher magnetic background, likely due to power lines present much closer to the site than at the Hanford detector site. Except for the 60 Hz harmonics, both background levels are low enough that they are not a significant limit to LIGO sensitivity, as described in Section 3.3. The broadening of the 60 Hz peak in the LLO spectrum is due to glitches in the 60 Hz amplitude, whose source we have not yet located.

The major coupling mechanisms for magnetic and electromagnetic noise involve electronic modules, cables and the magnets located on the interferometer optics (used as actuators for mirror position control). Each optic has four magnets glued on its back and one on the side surface, which are then actuated by coils mounted on the frame surrounding the optic. The magnets alternate in polarity so that uniform magnetic field gradients do not directly have a displacement effect on the optic (up to the level the four magnet strengths were matched). However, any magnetic field gradient comparable to the magnetic field produced by the actuation coil can introduce noise in the length measurement directly related to the detector output.

The Crab pulsar [55] would produce continuous GWs near 59.6 Hz (double its rotation frequency), which happens to be very close to the US electric power system frequency at 60 Hz. The possibility of detection or of a significant bound on the amplitude of its GW emission hinges on being able to take sensitive data for long periods of time, to resolve the coherent signal expected from a pulsar. Transients in current flow (such as motors turning on and off) reduce the sensitivity of the detector to the Crab pulsar by broadening the 60 Hz peak. For example, an unknown source of 60 Hz transients at LLO made the Crab pulsar search less sensitive than the LHO search by a significant factor of a few [47].

3.2.4 Radio Frequency Influences

LIGO uses a modulation-demodulation scheme, known as heterodyning, to generate error signals for controlling the length and angular degrees of freedom of the interferometer. In S5 it was found that radio frequency (RF) noise from the environment could couple to the modulation frequencies in the interferometer and produce noise in the output signal in the frequency band of interest for GWs. A major change in the upgrade from the fifth science run to the sixth science run was changing the readout from heterodyne detection to a DC homodyne scheme [56] [57]. The DC readout scheme for the main differential arm length signal used in S6 should have reduced this coupling, but it is important to continue to monitor this coupling since RF modulation is still used in the auxiliary length and alignment control system.

3.3 Injection Methods

To quantify the effect that environmental influences have on LIGO sensitivity it is necessary to measure both the noise and its coupling to the detector output. Here we describe a method of environmental injections which quantifies the coupling by injecting an environmental signal with known amplitude and spectral content and measuring its effect on the detector.

For seismic injections we use a weighted cart and shakers, for acoustic injections we use a large 500W speaker, for magnetic injections we use a 1m diameter, 100-turn copper coil and for RF injections we use an RF source far outside the buildings, set to 100 Hz near the main modulation frequency of our controls. We use a different power source than the one used for the detector electronics such that the current draws of our equipment do not couple through. For all measurements except the RF ones we place the noise source in the same room as the detector, trying to get large but equal distances both to the assumed coupling sites and the witness sensor. This presents some technical difficulty, since the coupling sites may not be known in advance.

We perform injections in various locations with respect to the detector in order to locate the largest coupling points and understand the measurement errors. This is not always possible and comparisons of coupling factors calculated for different injection positions suggest that the error in coupling factors can be as high as a factor of two. The measurements presented in this paper are part of a program of injections designed to determine the current status of the strongest couplings. Many other injections [47] were made to study coupling, e.g. along the beam tube, but the observed couplings were not great enough to be included in the standard set of injections, described here, that were performed multiple times during each science run.

The coupling function is the ratio of the calibrated environmental signal amplitude to the resulting differential arm length displacement. We choose an amplitude large enough that an effect can be produced and measured in the detector output. Because the LIGO detectors are well isolated, the limit to injection amplitudes is most often set by saturation in the sensor readout rather than excessive excitation in the GW readout. The injected environmental signal is typically a harmonic comb produced by a ramped sawtooth waveform. At each frequency multiple we divide the signal amplitude in GW readout by the amplitude in the sensor signal, in calibrated units, giving us a coupling function.

To estimate the level at which the ambient environmental noise couples into the detector, we multiply the measured coupling function by the normal ambient spectrum of the sensor. If this estimated background is an order of magnitude or more beneath the GW readout spectrum, we can say that for conditions close to those measured, this effect is not a significant or limiting noise source. We also track the coupling of these influences over long periods of time to look for variations and identify unwanted changes. In addition, we can also use natural sources of "injection signals", such as magnetic injections via lighting, seismic injections via nearby traffic or earthquakes, and acoustic injections via close airplanes.

A different method which has proven useful in the past is that of burst injections, which we briefly describe here. We apply a transient vibration to various locations around the detector, e.g. tapping an optical table, and look for large coupling sites. This method is hard to quantify due to variation in injection strength at the test location and closest relevant sensor, but in terms of relative effects on the GW signal we can narrow down and investigate suspected coupling sites.

Mitigation of either the source or the coupling is not always possible. Hence it is important to characterize and track the effect in question so as to introduce effective vetoes in the data for non-astrophysical events and quantitatively understand the limiting factors to the detector sensitivity [46].

3.3.1 Seismic Studies

Due to the strong attenuation provided by the LIGO seismic isolation, seismic noise limits LIGO's sensitivity at relatively low frequencies (under 50 Hz), below the band of best sensitivity around 100-200 Hz. However, nonlinear upconversion processes have the unwanted effect of converting low frequency seismic motion into noise in the frequency band of interest. Efforts to understand the mechanisms of upconversion have implicated Barkhausen noise in the magnets glued to the test masses themselves, or in the magnetic parts associated with the actuation on the mirrors [46] [58] .

Seismic injection studies were performed differently at the two sites because the higher ambient ground motion at LLO required the implementation of a supplemental active seismic isolation system. At the Hanford site we use a weighted cart moved back and forth at a frequency of 1.2 Hz. We are able to see an effect in the detector output both at the injected frequency and at higher frequencies, demonstrating upconversion, as shown in Figure 3.5.

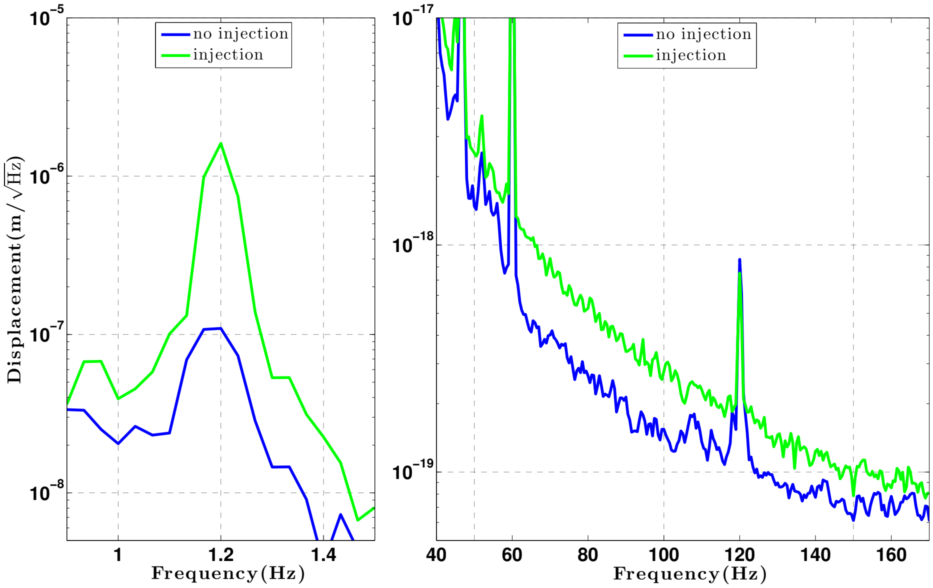

Figure 3.5: LHO GW readout displacement showing upconversion of a 1.2 Hz seismic injection. Both panels show the same data of the displacement in the GW channel, but in different frequency bands. The left panel shows the linear effect of the injected signal in the detector output, while the right panel shows that this injection produces noise at higher frequencies (known as "upconversion").

The 1.2 Hz frequency was chosen because it is at a resonance of one of the passive seismic isolation stacks, and hence even with a relatively small injection we can excite enough motion in the interferometer to see upconversion. Figure 3.5 shows the result of a 1.2 Hz injection an order of magnitude larger in the detector output than the usual level at 1.2 Hz. At LLO a signal injected with the same amplitude cannot be seen due to the extra seismic attenuation.

3.3.2 Acoustic Studies

To study the effect of acoustic noise coupling into the detector output we use a 500W speaker to produce an injection, and one or more microphones to measure the amplitude of the acoustic noise it produces. We ensure that the sensor is stationary and that the sound level at the studied coupling points and the sensors is about the same. In these studies, the approximate amplitude of the injection is $75\mathrm{mPa}/\sqrt{\mathrm{Hz}}$ or 40 mPa rms.

In the top panel of Figure 3.6 and Figure 3.7 we show the measured coupling of acoustic noise to the detector output by taking the ratio of the signal seen in the detector output to the signal seen in the microphone. Then we multiply this coupling function by the normal ambient spectrum of the microphones to obtain a predicted contribution of ambient acoustic noise to the detector output. In the corner station the coupling is expected to be higher due to more of the detector subsystems and auxiliary control signals being present (see Figure 3.1).

In the bottom panel of Figures 3.6 and 3.7 we show the predicted ambient acoustic noise contribution at LLO and LHO respectively in S6 (measured in June 2010). At low frequencies the acoustic noise has a 20-30% contribution to the noise in the detector output , while above 200 Hz it is more than 1 to 2 orders of magnitude lower than the strain noise and hence does not contribute significantly to the limit of the detector sensitivity. The amplitude variability is mostly due to the creation of nodes and antinodes of the sound waves in different locations around the detector room; we inject from different directions and placements to find the location from where the injection is the same in amplitude at the sensor and at the suspected coupling sites, but some mismatch remains.

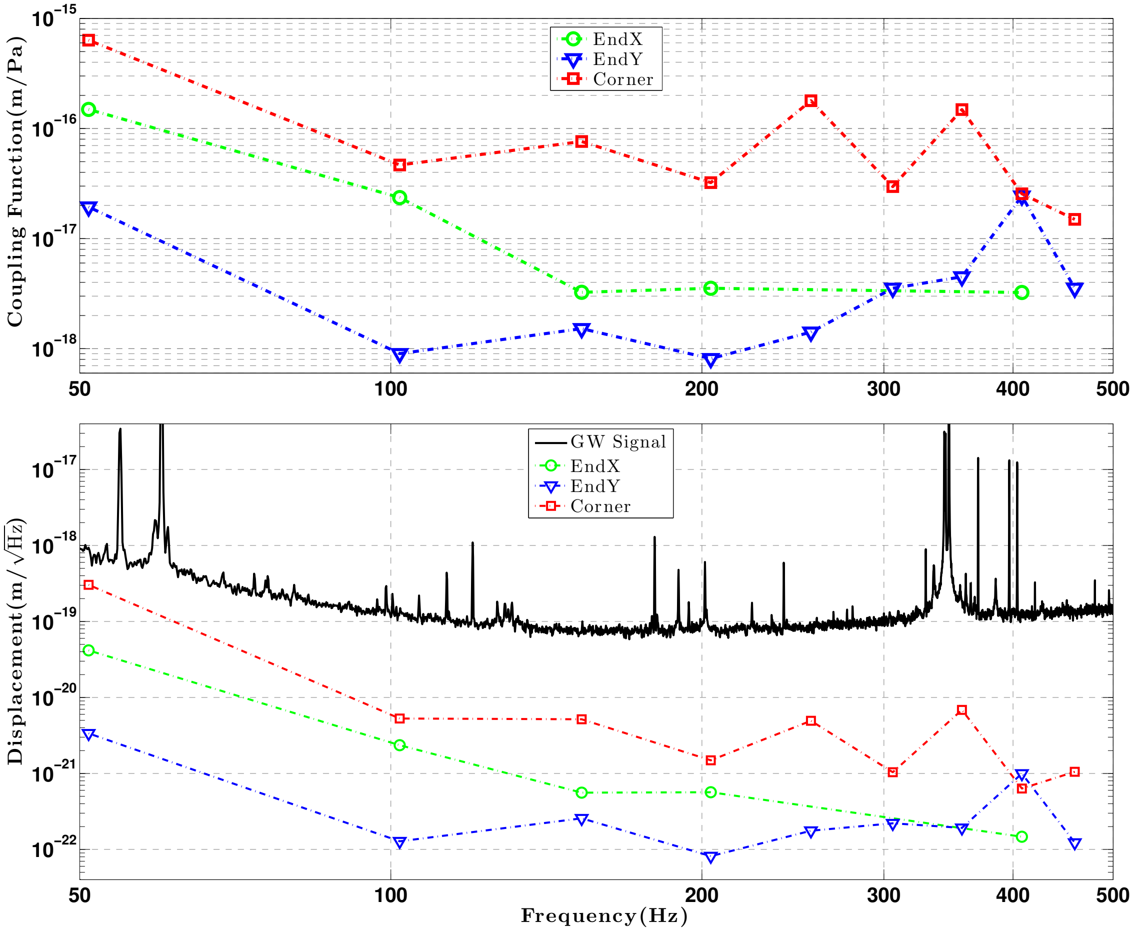

Figure 3.6: Acoustic injection results at LLO for each detector building. The top panel shows the measured acoustic coupling function obtained from injecting acoustic noise in each builing. The calculated points then get multiplied by the ambient background level sensed by the microphones in each building to obtain the background estimate shown in the bottom panel.The coupling is only estimated at the injection frequencies marked in the plot.

3.3.3 Magnetic Studies

To study magnetic noise coupling into the detector output we use a 1 meter diameter coil to create a magnetic field injection. We position the injection coil relatively far away (10-20 meters in the same room) such that the field produced would be the same at the studied coupling site (usually the magnet actuators on the optics) and the magnetometer. In these studies, the approximate injection amplitude used is 130nT/$\sqrt{\text{Hz}}$ or 70 nT rms.

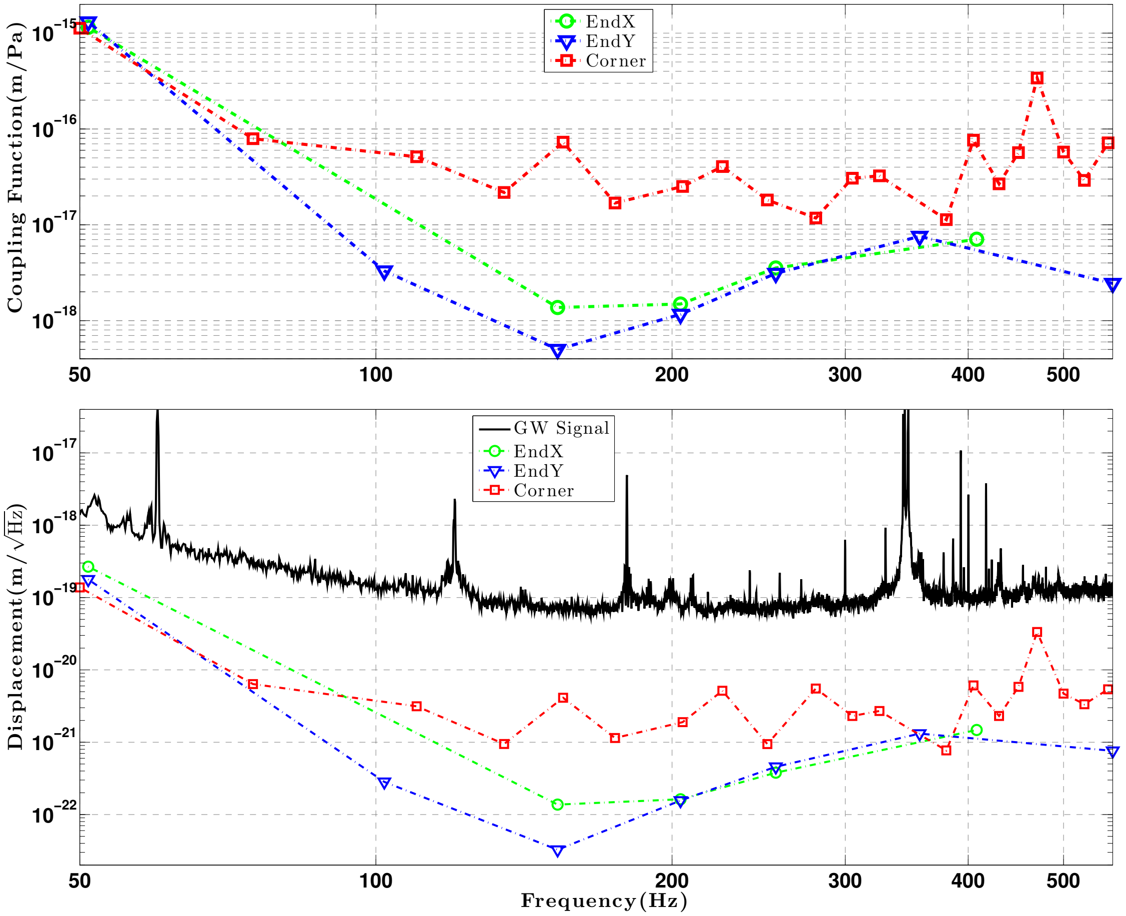

Figure 3.7: Acoustic injection results at LHO for each detector building, equivalent to Figure 3.6.

We use a calibrated magnetometer to read the size of the injections and compare to the signal amplitude in the detector output. This results in a magnetic coupling function, as the one shown for LLO in S6 in the top panel of Figure 3.8 and for LHO in Figure 3.9 . We expect the coupling to depend on frequency as f^{-3}, with two factors of $1/f^2$ from the pendulum response and one factor of 1/f from eddy current damping of the steel vacuum chamber.

The bottom panel of Figure 3.8 shows the predicted contribution of magnetic and electromagnetic ambient noise to the detector output. We conclude that, excluding the 60 Hz and its harmonics, ambient low-frequency electromagnetic noise did not significantly affect LIGO sensitivity in S6.

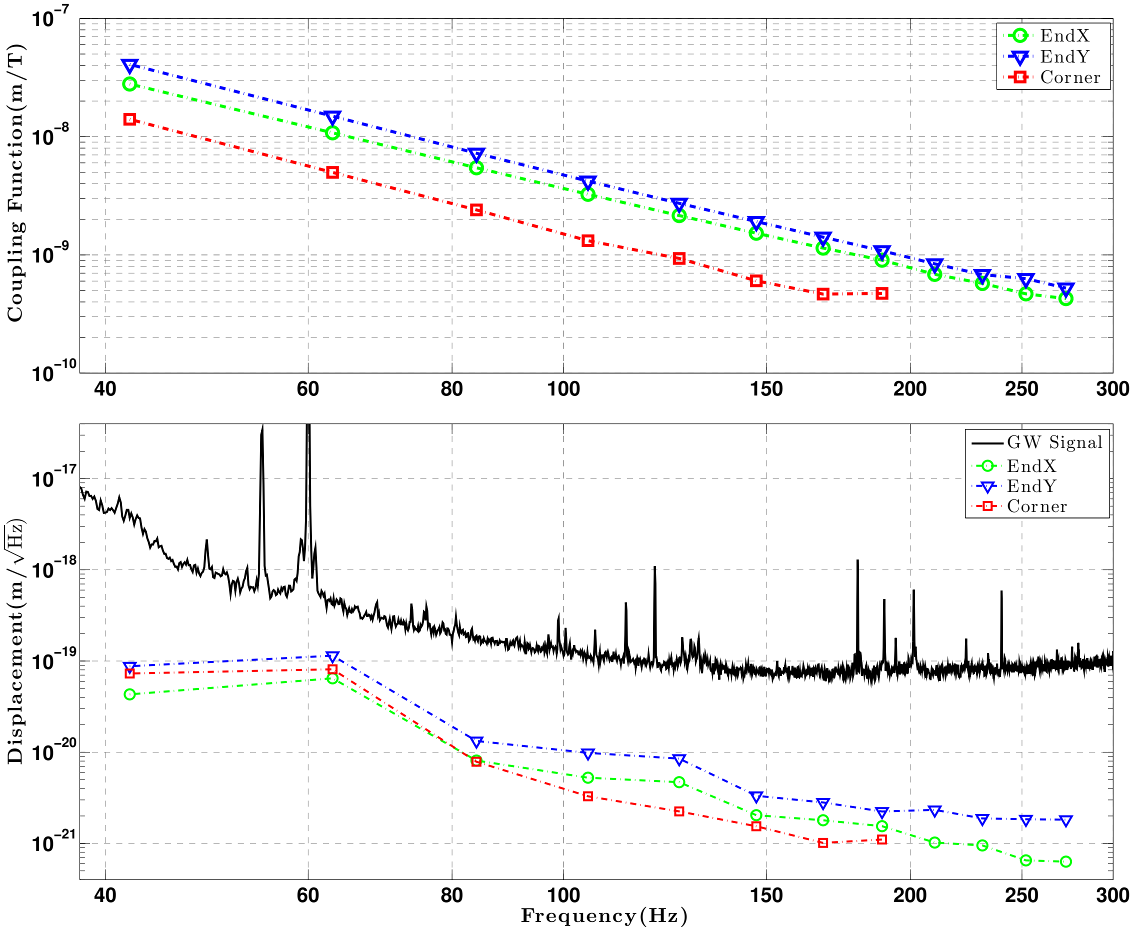

Figure 3.8: Magnetic injection results at LLO for each detector building. The top panel shows the measured magnetic coupling function obtained from injecting magnetic noise in each building. The calculated points then get multiplied by the ambient background level sensed by the magnetometers in each building to obtain the background estimate shown in the bottom panel.The coupling is only estimated at the injection frequencies marked in the plot.

3.3.4 Radio Frequency Studies

The readout of the detector is in the audio band, so RF noise in the range of 1-100 MHz cannot couple directly. However, RF signals are used for control in the detector in a PDH-like heterodyning scheme, and so noise within a few kHz of the RF frequency used could disturb the sensitivity of the detector by coupling through auxiliary controls. To study radio frequency electromagnetic noise coupling into the detector output we place an amplified RF signal generator outside the corner building, far enough away (approximately 250m)

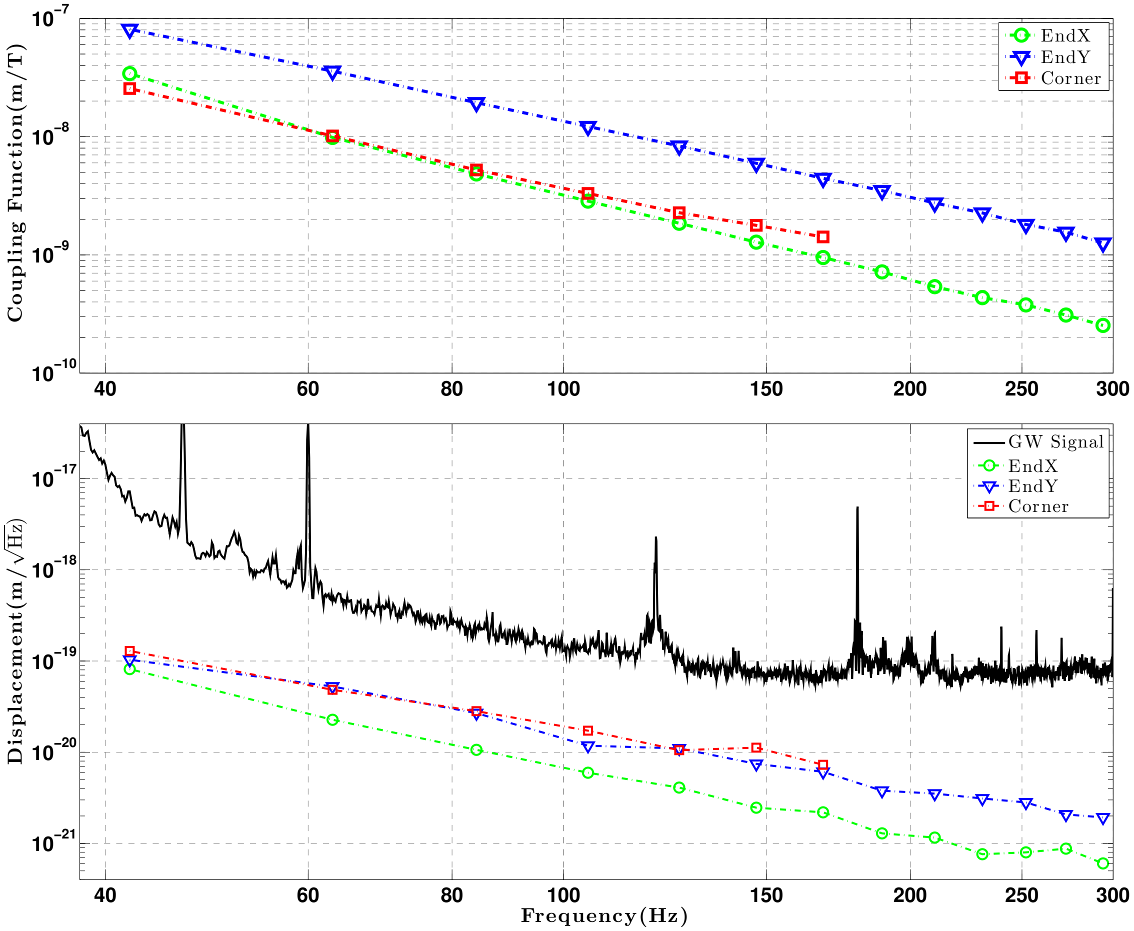

Figure 3.9: Magnetic injection results at LHO for each detector building, equivalent to Figure 3.8.

to produce the same amplitude RF injection on the length scale of the detector corner components (where the RF control signals are read). We tune the injection frequency close to 24.5 MHz (e.g. 24.5 MHz + 100 Hz), the main modulation frequency for the interferometer controls. We then measure the resulting injection strength with a radio antenna near the detector and compare to the signal we see in the detector readout at audio frequencies.

During the fifth science run, when RF readout was used, the RF ambient contribution was determined to be two orders of magnitude or more below the detector background. This was expected to become even lower with the use of DC readout, and was found to be 3 orders of magnitude below the detector output.

3.4 Conclusions and Future Studies

LIGO was designed to be isolated from environmental noise sources in its gravitational wave measurement band of 50 Hz to 7 kHz. Through injection studies we show that ambient stationary acoustic and magnetic sources do not contribute significantly to the noise limiting the S6 LIGO sensitivity. We have also shown the presence of seismic upconversion noise although the mechanism has not been fully understood. We prove that our PEM sensors are more sensitive to the environment than the detector output, making them essential in ruling out environmental causes for candidate GW signals. Furthermore, the PEM system has proven useful in investigating and eliminating undesired large couplings of acoustic, seismic and magnetic noise in various frequency bands.

The environment at the detector sites will remain the same for Advanced LIGO, but the vastly different design of Advanced LIGO will undoubtedly have very different coupling mechanisms and levels for the same environmental noise sources. The same level of environmental coupling as measured in S6 would however be a limiting noise source for Advanced LIGO and this has been carefully taken into account in the design of the seismic, suspension, optic actuation and other auxiliary systems. Advanced LIGO is not expected to be limited by environmental noise above 20 Hz. The improvement in seismic and suspensions isolation will lower the seismic coupling above 20 Hz by a few orders of magnitude. For acoustic coupling reduction, all control photodiodes have been moved inside the vacuum system and are located on seismically isolated tables. For magnetic coupling reduction, test masses will be controlled by electromagnets in upper stages of the suspension (with no magnets present on the optic itself) and as such providing additional filtering.

With the experience gained from initial LIGO we will perform similar investigations for the Advanced LIGO detector, measuring the environmental coupling levels, searching for the causes of unwanted features or noise limits we discover in the new detector output, and mitigate any sources or mechanisms we find in the process.

CHAPTER 4
DUAL-RECYCLED MICHELSON INTERFEROMETER (DRMI): SENSING MODEL AND MEASUREMENTS

As previously explained, the DRMI includes all optics and subsystems of the interferometer excluding the long arm cavities and end test masses. It is very useful for multiple reasons. First of all, at the Livingston site it was installed before the long arms of the interferometer. It not only provided a test bed for testing all the installed subsystems: seismic platforms, suspensions, actuation and readback electronics, digital controls software, etc but it also allowed for the commissioning of a simpler configuration (3 length degrees of freedom versus 5 in the full interferometer) while providing a sensitive measurement of some of the key noise sources in the interferometer. Some issues arose, as is the case with complex instruments, and they were diagnosed and fixed earlier.

In the DRMI there are other sub-configurations which can prove useful, depending on which mirrors are aligned to form resonant cavities. Figure 4.1 shows a few of these possibilities which are useful in the characterization of various subsystems. We will refer to these throughout this document for cross-checks of measurements, where possible. If the signal recycling mirror is misaligned, then we can lock a power-recycled Michelson interferometer (PRMI). Similarly, if the power recycling mirror is misaligned, we can lock a signal recycled Michelson interferometer (SRMI). If both recycling mirrors are misaligned, we can lock a simple Michelson interferometer, etc.

The power recycling cavity is a special case because, as explained in Chapter 2, in the full interferometer lock it resonates both the carrier and the sidebands. However, without the arms on resonance (in DRMI), there is a phase flip on the carrier, so the PRC can resonate either the sidebands or the carrier but not both at the same time. In the locking scheme for the full interferometer, one of the principal steps is locking the DRMI with the PRC resonating the sidebands. As such, having a stable sideband-locked DRMI on the 3rd harmonic (3f) signals was the first priority of the commissioning team after installation

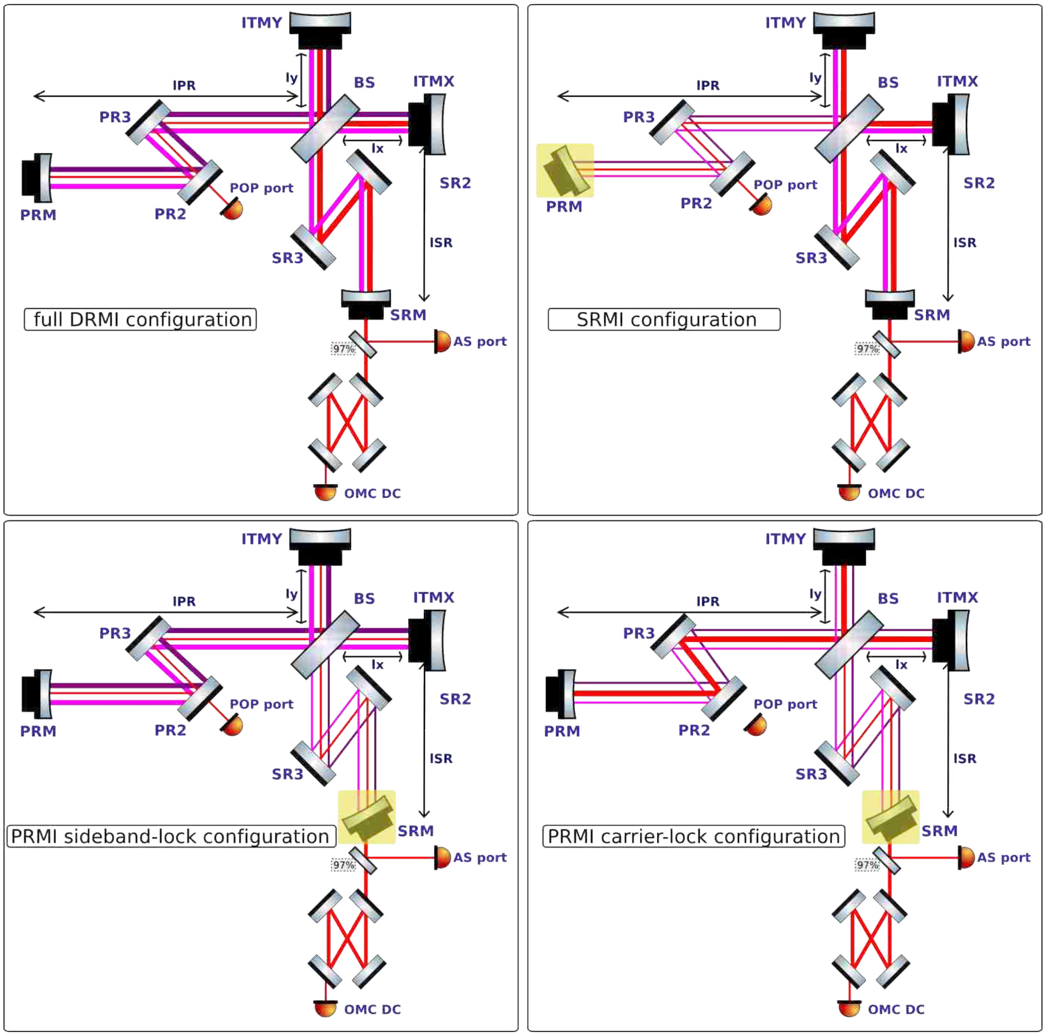

Figure 4.1: A few of the more important sub-configurations of the DRMI. The misaligned optics are highlighted. If we misalign the PRM, then the PRC cavity is no longer on resonance. This leaves only the SRC resonant in what is called the Signal-Recycled Michelson Interferometer (SRMI). Similarly, if we misalign the SRM, we are left with a Power-Recycled Michelson Interferometer (PRMI). Here we have the choice of locking it to resonate either the carrier or the sidebands in the PRC cavity.

was complete. However, locking the PRMI on carrier allows much more light to resonate in the cavity and provides a more sensitive configuration.

Figures 4.2 to 4.4 show the difference in 1f and 3f signals between DRMI and full interferometer lock. The 1f signals change by a factor of a few to tens and sometimes even change sign, while the 3f signals change by at most some 50%, which is well within the stability of the feedback loops.

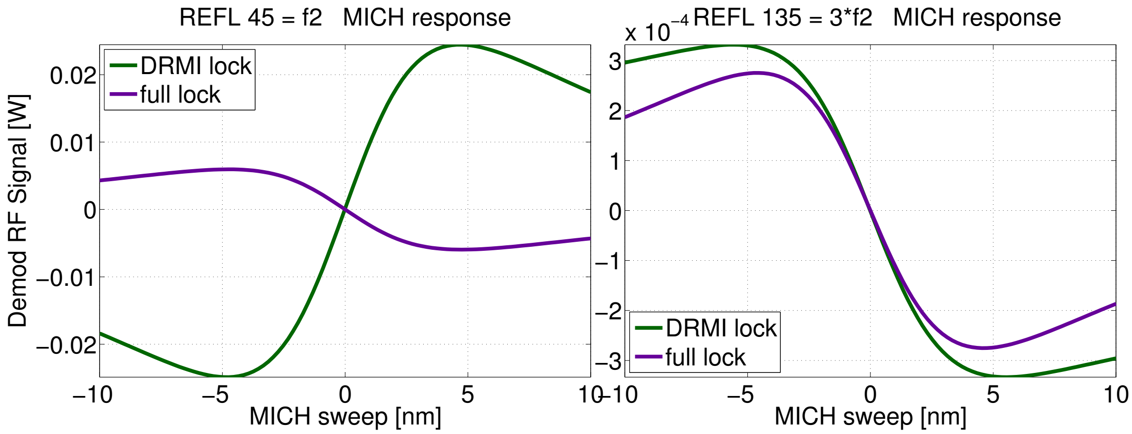

Figure 4.2: The change in slope of MICH locking signals from DRMI to full lock, comparing 1f to 3f signals. The x-axis is length change in the MICH degree of freedom, the y-axis is the response of the sensor to this length change and so the slope represents the sensing strength. The 3f signal barely change at all, so they are robust to use as the carrier becomes resonant in the arms and the PRC.

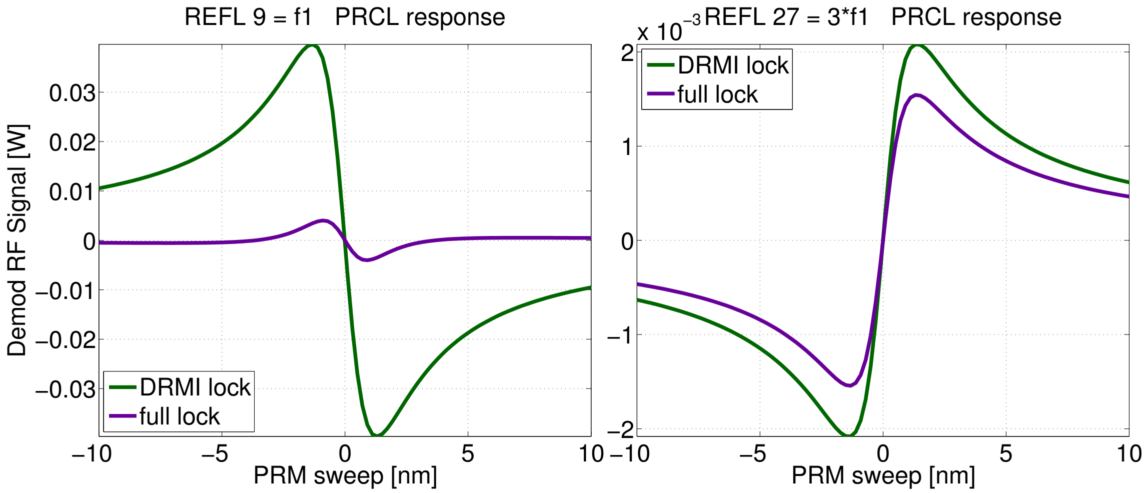

Figure 4.3: The change in slope of PRCL locking signals from DRMI to full lock, comparing 1f to 3f signals. The x-axis is length change in the PRCL degree of freedom.

4.1 DRMI Modeling in Optickle

4.1.1 The Model

The Optickle package for Matlab[42] was written for LIGO specifically to aid in laser field propagation calculations. Once given optics linked by distances and a laser source with amplitude modulation (AM) and/or phase modulation (PM), it will calculate the

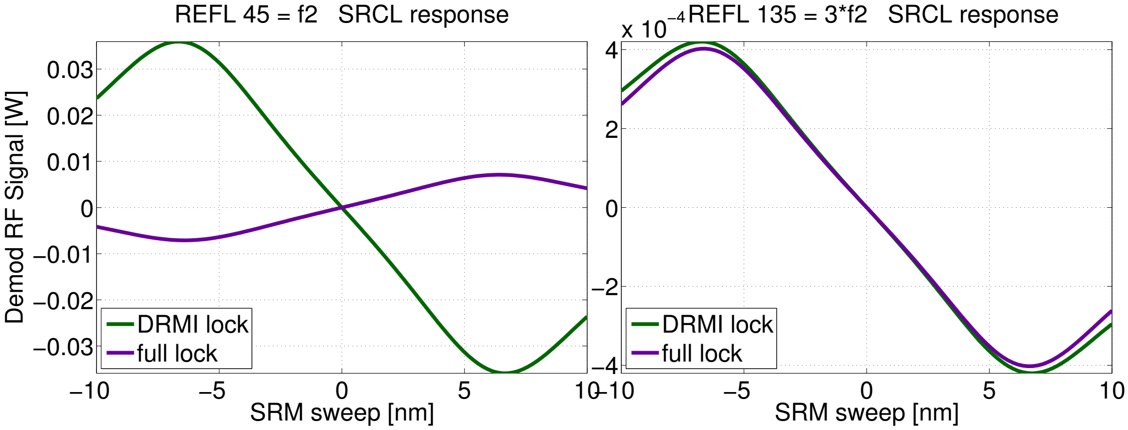

Figure 4.4: The change in slope of SRCL locking signals from DRMI to full lock, comparing 1f to 3f signals. The x-axis is length change in the SRCL degree of freedom.

fields everywhere, taking into account resonant conditions of optical cavities. Ports can be added to read demodulated signals at RF frequencies. Furthermore, it can calculate quantum noise at each of these ports. It does not however take into account higher order modes or mode-matching of beam sizes at mirrors.

I have built a model of the advanced LIGO DRMI, with parameters and ports as shown in Figure 2.13. In the model we can choose to excite one of the three degrees of freedom (MICH, PRCL and SRCL) and record the size of the signal at each port for each demodulation frequency available, in units of W/m (watts of power detected per meter of cavity motion). We are looking to find three independent sensors or combination of sensors to use in the feedback loops for keeping these cavities resonant. In other words we are looking for the *sensing matrix* given the sensor positions and demodulation frequencies.

The powers at a few key points in the DRMI are shown in Table 4.1, split into carrier and upper and lower sidebands to showcase the resonances. The 9 MHz sidebands are denoted as f_1 and the 45 MHz are denoted as f_2. Comparing the input power with the PRC, we see that both sidebands are resonant, while most of the carrier is anti-resonant (reflected by the cavity). The Michelson is kept “dark”, hence most of the power incident on the BS is not transmitted to the SRC. However, there is much more power in the 45 MHz sideband that in the 9 MHz one. This is due to two factors, one is the Schnupp assymetry and the second is that the SRC is resonant for the 45 MHz and anti-resonant for the 9 MHz.

Table 4.1: Optickle model powers in DRMI, by location and frequency, in Watts. REFL signifies all the power reflected from the PRM and AS signifies all the power leaving the SRC towards the OMC and the AS port. The code applies losses of 11% from input optics.

↓Frequency	Input	REFL	PRC	SRC	AS
-f_2	6.6e-2	9.7e-3	0.86	0.12	4.2e-2
-f_1	6.6e-2	6.7e-3	3.8	3.0e-4	1.0e-4
carrier	4.2	4.2	3.2e-2	7.9e-11	2.8e-11
f_1	6.6e-2	6.7e-3	3.8	3.0e-4	1.0e-4
f_2	6.6e-2	9.7e-3	0.86	0.12	4.2e-2

Figures 4.5 to 4.8 show all the RF fields present at the input, in reflection and inside the PRC. This is another way to look at which fields resonate in the cavities and which are promptly reflected. Because the modulations are applied in series, other fields are also significant, such as the difference and sum of the two modulation frequencies. This is one reason to use resonant circuit photodiodes to extract only the RF frequency signal of interest.

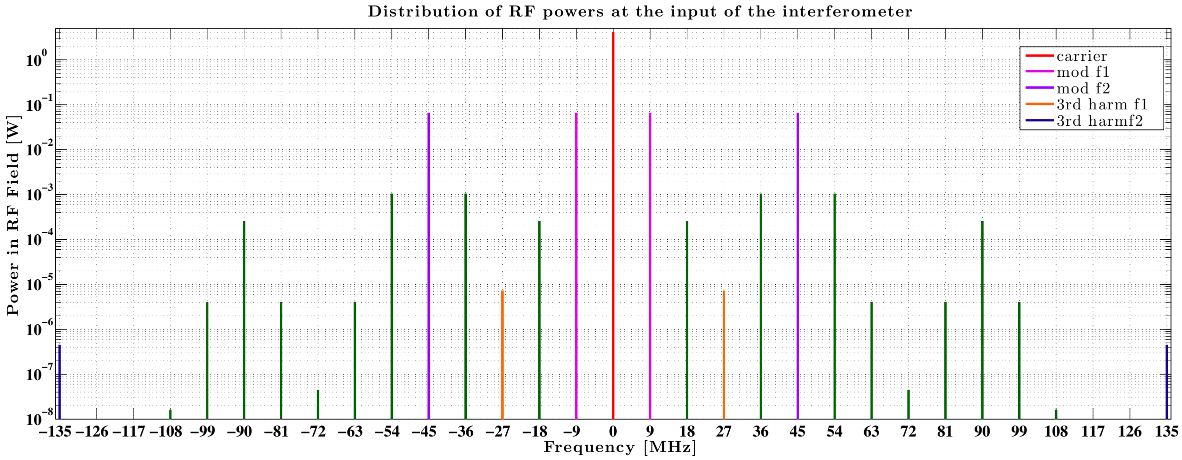

Figure 4.5: RF field powers at the input of the DRMI with 4.45W input, and modulation strength of 0.25 for both 9 and 45 MHz.

The amount of amplification by a cavity is given by its finesse depending on the reflectivities of the mirrors which form it. One way to easily quantify it is to calculate the buildup, the ratio of the power inside the cavity to the power going into the cavity. From the table above we can calculate that the buildup in the PRC for the 9 MHz sideband is about 58 and for the 45 MHz sideband it is 13.

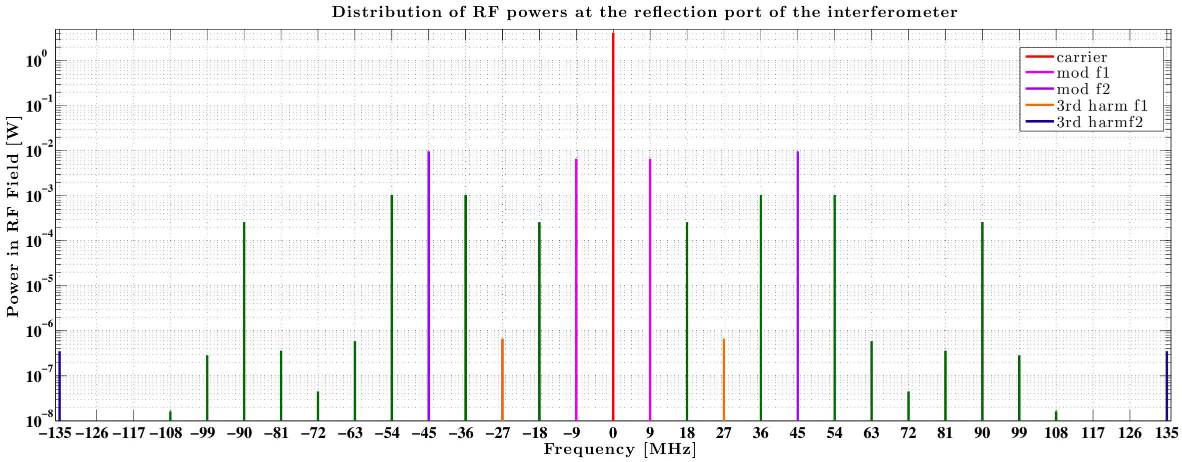

Figure 4.6: RF field powers at the reflection port of the DRMI with 4.45W input, and modulation strength of 0.25 for both 9 and 45 MHz.

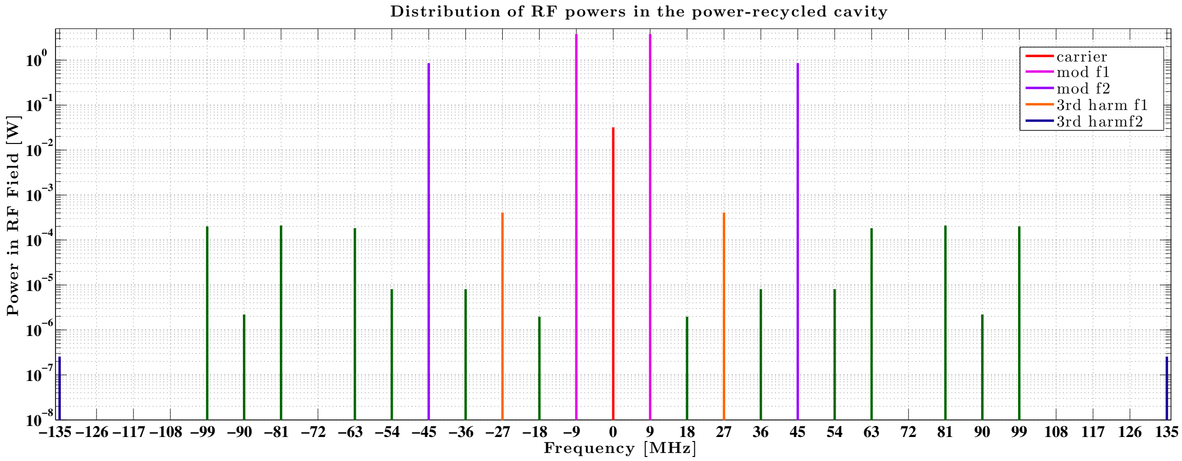

Figure 4.7: RF field powers inside the PRC of the DRMI with 4.45W input, and modulation strength of 0.25 for both 9 and 45 MHz.

One caveat about showing complex RF fields as power is that a photodiode would actually sense the beat of these fields and so the power at some frequency shown in the plots above may not correspond to what a photodiode would read. But the figures give a sense of which components of such beats may be significant. For example, for detecting the third harmonic of the 9 MHz modulation (29 MHz) we have to be careful to account

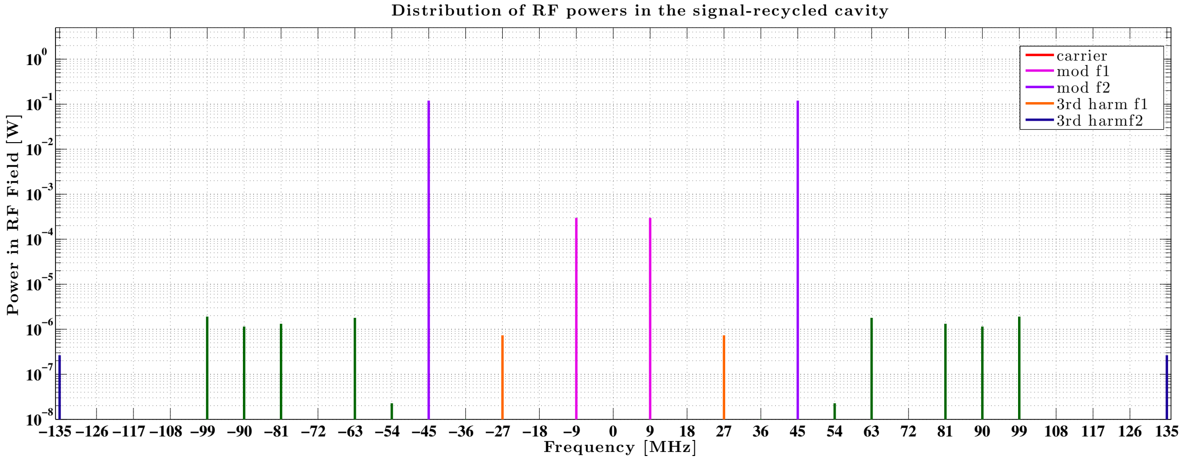

Figure 4.8: RF field powers inside the PRC of the DRMI with 4.45W input, and modulation strength of 0.25 for both 9 and 45 MHz.

for the "fourth harmonic" which arises from the beat of the first and second modulation frequencies at the input.

4.1.2 The Sensing Matrix

An example sensing matrix is shown in Table 4.2 for a DRMI of input power 5W and modulation depth of 0.25 for both the 9 MHz and the 45 MHz sidebands. The sensors are named by port, then they receive "AIR" if they are on in-air tables instead of in vacuum, and the demodulation frequency in MHz.

Table 4.2: LSC sensing matrix for a DRMI with input power of 5W and modulation depths of 0.25. The magnitudes are expressed in W/m and the phases in degrees. The phase by itself has no meaning (given by cable lengths and so on), but the relative phase between two degrees of freedom is important. If they are orthogonal, they can be extracted from the same sensor in the I and Q demodulation phases. The demodulation phases can be rotated digitally.

↓Sensor	MICH m.	PRCL m.	SRCL m.	PRCL-MICH ϕ	PRCL-SRCL ϕ
ASAIR 45	9.6e3	4.7e2	54	88	1
REFL 9	4.6e4	1.7e7	1.6e4	22	179
REFL 45	1.4e6	3.3e6	4.5e5	91	1
REFLAIR 27	1.4e4	6.2e5	3.3e3	60	5
REFLAIR 135	1.1e4	2.7e4	4.0e3	90	1
POP 9	57	2.2e4	20	22	179
POP 45	1.7e3	4.0e3	5.7e2	91	1

A different way to look at these numbers is to put them on a radar-type plot, where the I and Q phases define the axes at 0° and 90°, as shown in Figure 4.9. When we refer to I and Q phase rotation, we refer to rotating the axes in these plots but keeping them at 90° from each other. In practice this is done by exciting some actuator and maximizing the signal in one of the phases while minimizing it in the other.

There are a few things to notice about the signals. If the relative amplitudes in the same sensor are larger than a factor of 100, we cannot hope to use that sensor but for its strongest component. This is due to the fact that we probably cannot phase the I and Q rotation phase to better than 1% in the long run. The POP port has much weaker signals than the other ports, it is only quoted here for completeness. Its usefulness comes into play only in the full interferometer configuration.

PRCL is the strongest signal in most sensors, while MICH and SRCL are obviously stronger in 45 MHz demodulation signals. This is due to the optical arrangement that the SRC only resonates 45 MHz. MICH is orthogonal ($\approx$ 90 degrees apart) from PRCL and SRCL in most signals. Its signal is largest in REFL 45, so this is the signal used for its control loop. Due to the comparable sizes of PRCL and SRCL in that sensor, the phasing has to be done carefully to ensure that the PRCL and SRCL contributions to that demodulation phase are small. Traditionally the Q phase has been used for MICH.

SRCL is a hard signal to extract because it is in the same phase as PRCL, and always smaller. As such, we would like to use a subtraction of signals for its sensor. Since PRCL is largest in REFL9, we will use REFL 9 for its sensor, and then use a combination of REFL9 and REFL45 for SRCL, such that the PRCL contribution is minimized. In the full interferometer a similar scheme is used for these DOFs, but using the POP sensors. In conclusion, it is much more important to understand the behavior of signals in 45 MHz (and harmonics) sensors because from these we have to extract multiple diagonalized sensing signals, while the 9 MHz sensors are sensing mostly PRCL.

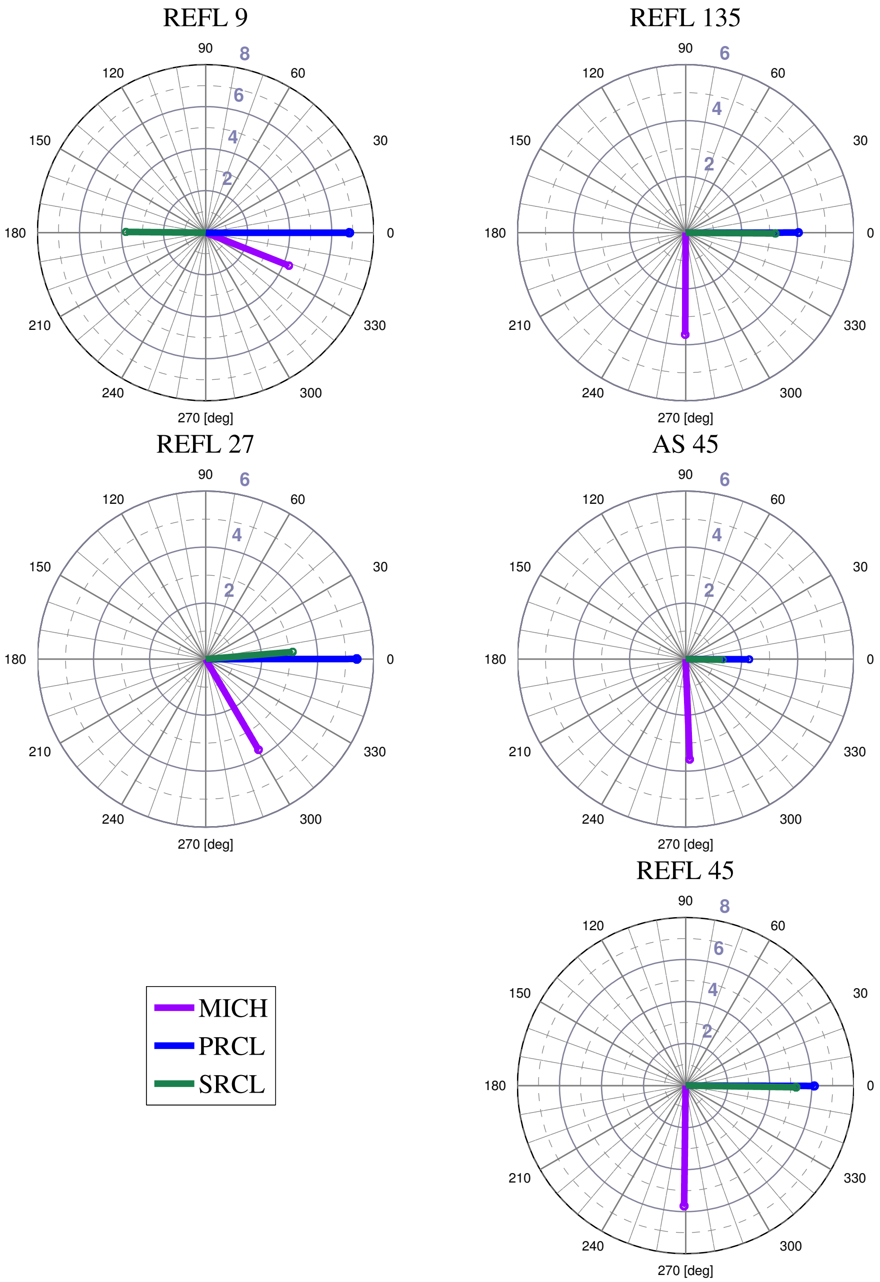
REFL 9

REFL 135

REFL 27

AS 45

REFL 45

Figure 4.9: DRMI sensing matrix obtained from Optickle model, shown in radar form for the most important sensors. The amplitude is logarithmic and the phase is in degrees.

The 3f signals (27 and 135 MHz) are much weaker than their 1f counterparts. However, as explained in Chapter 2, they are needed for the lock acquisition process. Since they are an intermediary step, they are allowed to be weaker, which results in higher electronics noise contribution to the control of the DOFs when they are employed as sensors. Similarly to the argument above, for the 3f-locked configuration we use one phase of REFL135 for MICH, REFL27 for PRCL and a combination of the two for SRCL.

To illustrate this better, Figure 4.10 shows the effect of sweeping the three DOFs in the two sensors of interest, REFL 9 and REFL 45. The slope of the signal near resonant is the magnitude in the sensing matrix in units of W/m. Also to be noticed is that the PRCL linear signal range is much narrower than the other DOFs, as is to be expected from the higher finesse.

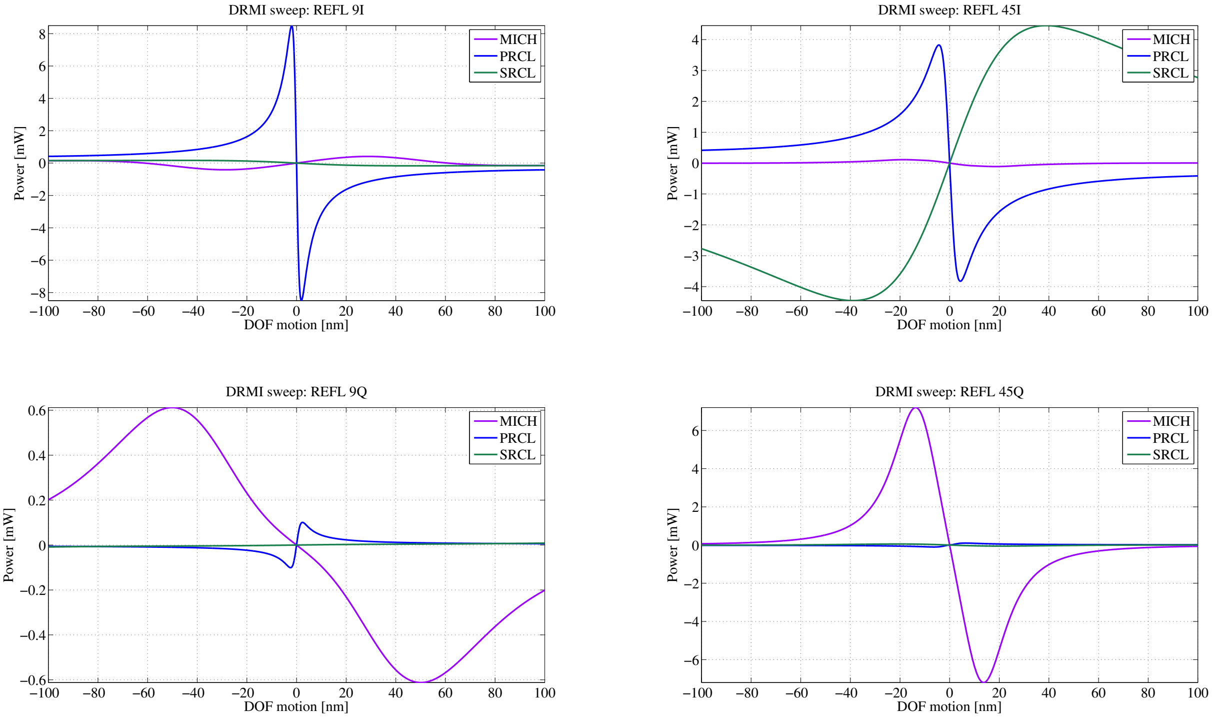
DRMI sweep: REFL 9I

DRMI sweep: REFL 45I

DRMI sweep: REFL 9Q

DRMI sweep: REFL 45Q

Figure 4.10: Sweeps of MICH, PRCL and SRCL (separately) and the response in the REFL9 and REFL45 sensors. At 0 the cavity is on resonance, and then each DOF is swept by the x-axis length amount to study the signal behavior.

For completion, we show here the model derived sensing matrices for the other configurations of interest. Even though only DRMI sideband is used in the locking procedure of the full interferometer, some of the other configurations may be more sensitive (the carrier-locked DRMI and PRMI) or simpler to control for diagnostics of a certain subsystem.

- DRMI carrier locked in Tables 4.3 and 4.4;

- PRMI sideband locked in Tables 4.5 and 4.6;
- PRMI carrier locked in Tables 4.7 and 4.8;
- SRMI sideband locked in Tables 4.9 and 4.10.

Table 4.3: Optickle model powers in DRMI carrier-locked, by location and frequency, in Watts.

↓Frequency	Input	REFL	PRC	SRC	AS
-f_2	6.6e-2	6.6e-2	5.2e-4	7.3e-5	2.6e-5
-f_1	6.6e-2	6.6e-2	5.1e-4	4.0e-8	1.4e-8
carrier	4.2	0.42	240	5.9e-7	2.1e-7
f_1	6.6e-2	6.6e-2	5.1e-4	4.0e-8	1.4e-8
f_2	6.6e-2	6.6e-2	5.2e-4	7.3e-5	2.6e-5

Table 4.4: LSC sensing matrix for a DRMI carrier-locked with input power of 5W and modulation depths of 0.25. The magnitudes are expressed in W/m and the phases in degrees. This would be the most sensitive configuration for the DRMI but notice that the SRCL DOF is impossible to extract, since it is much smaller than all other DOFs in all sensors.

↓Sensor	MICH m.	PRCL m.	SRCL m.	PRCL-MICH ϕ	PRCL-SRCL ϕ
ASAIR 45	2.0e4	72	32	103	15
REFL 9	1.7e3	1.7e7	1.0e3	55	6
REFL 45	6.7e3	1.7e7	1.3e3	106	177
REFLAIR 27	8.2e3	7.3e5	4.4e2	174	175
REFLAIR 135	3.1e3	4.6e4	2.1e3	271	1
POP 9	2.0	2.1e4	2.2	73	4
POP 45	96	2.1e4	31	91	180

Table 4.5: Optickle model powers in PRMI sideband-locked, by location and frequency, in Watts.

↓Frequency	Input	REFL	PRC	SRC	AS
-f_2	6.6e-2	1.9e-3	3.0	0.17	6.0e-3
-f_1	6.6e-2	6.4e-3	3.8	8.6e-4	3.0e-4
carrier	4.2	4.2	3.2e-2	3.2e-12	1.1e-12
f_1	6.6e-2	6.4e-3	3.8	8.6e-4	3.0e-4
f_2	6.6e-2	1.9e-3	3.0	0.17	6.0e-3

From these different configurations we can extract further information about the fields in the cavities. For example, it is interesting to note the differences between the buildups

Table 4.6: LSC sensing matrix for a PRMI sideband-locked with input power of 5W and modulation depths of 0.25. The magnitudes are expressed in W/m and the phases in degrees.

↓Sensor	MICH m.	PRCL m.	PRCL-MICH ϕ
ASAIR 45	760	73	86
REFL 9	1.4e5	1.7e7	90
REFL 45	5.4e5	1.3e7	90
REFLAIR 27	7.0e3	6.9e5	88
REFLAIR 135	5.2e3	1.2e5	90
POP 9	170	2.1e4	90
POP 45	680	1.7e4	90

Table 4.7: Optickle model powers in PRMI carrier-locked, by location and frequency, in Watts.

↓Frequency	Input	REFL	PRC	SRC	AS
-f_2	6.6e-2	6.6e-2	5.1e-4	2.9e-6	1.0e-6
-f_1	6.6e-2	6.6e-2	5.1e-4	1.2e-7	4.1e-8
carrier	4.2	0.42	240	2.4e-8	8.3e-9
f_1	6.6e-2	6.6e-2	5.1e-4	1.2e-7	4.1e-8
f_2	6.6e-2	6.6e-2	5.1e-4	2.9e-6	1.0e-6

Table 4.8: LSC sensing matrix for a PRMI carrier-locked with input power of 5W and modulation depths of 0.25. The magnitudes are expressed in W/m and the phases in degrees.

↓Sensor	MICH m.	PRCL m.	PRCL-MICH ϕ
ASAIR 45	8.5e2	38	87
REFL 9	4.0e3	1.7e7	96
REFL 45	2.2e4	1.7e7	92
REFLAIR 27	7.3e3	6.9e5	88
REFLAIR 135	4.6e3	1.0e5	89
POP 9	6.9	2.1e4	94
POP 45	37	2.1e4	91

in the DRMI sideband-lock and PRMI sideband-lock. The 45 MHz sideband buildup goes from 13 in DRMI to 45 in PRMI (no SRC). This is because the SRC resonates the 45 MHz sideband as well, but reflects the 9 MHz sideband. So to switch in between the two configurations, we need to change the loop gains by an approximate factor of 4.

Table 4.9: Optickle model powers in SRMI, by location and frequency, in Watts.

↓Frequency	Input	REFL	PRC	SRC	AS
-f_2	6.6e-2	5.6e-5	2.0e-3	2.8e-4	9.7e-5
-f_1	6.6e-2	5.9e-5	2.0e-3	1.6e-7	5.4e-8
carrier	4.2	3.7e-3	0.13	3.1e-10	1.1e-10
f_1	6.6e-2	5.9e-5	2.0e-3	1.6e-7	5.4e-8
f_2	6.6e-2	5.6e-5	2.0e-3	2.8e-4	9.7e-5

Table 4.10: LSC sensing matrix for an SRMI with input power of 5W and modulation depths of 0.25. The magnitudes are expressed in W/m and the phases in degrees.

↓Sensor	MICH m.	SRCL m.	SRCL-MICH ϕ
ASAIR 45	930	0.36	75
REFL 9	0.72	1.0	203
REFL 45	94	32	90
REFLAIR 27	0.78	0.25	72
REFLAIR 135	6.4e-2	6.3e-2	92
POP 9	6.0e-2	8.7e-2	203
POP 45	7.8	2.7	90

The most sensitive configuration of the DRMI would be the carrier-lock of all three DOFs. But, as shown above, in that configuration we cannot easily extract an RF signal to use for the SRCL DOF. This is somewhat intuitive since the sidebands are not resonant in the PRC and so there is little sideband power in the SRC. However, due to the high 35% transmission of the SRM, the SRC cavity does not have a high buildup. Looking between the PRMI and DRMI configurations at the 45 MHz power in the SRC, we can derive that the SRC buildup is about 3. This means that using a carrier-locked PRMI instead will only take the desired sensitivity down by a factor of 3.

The SRMI configuration is quite weak because the PRM is misaligned to obtain it, and its 3% transmission makes it such that very little power goes into this configuration. Nonetheless, the configuration can be locked and useful as a diagnostic of the SRC.

4.1.3 Ideal Feedback Setup

If we were to normalize the actuator and sensor responses, the design of the feedback loops would look as shown in Figure 4.11. For PRCL and SRCL, the actuator choice is easy:

the PRM and SRM are respectively diagonal actuators for these two DOFs. For the MICH the perfect diagonal actuator would be sending the feedback signal with opposite signs to the ITMs. This is not done for two reasons: one is that the range of the ITM actuators is too small (a choice to reduce background electronics noise from the actuator) and that we do not want to couple the MICH feedback loop to the mirrors involved in the readout of DARM, the gravitational wave signal. The next choice is the BS, but moving only this mirror also creates changes in the PRC length and SRC length, and to compensate this we choose to send the geometrical opposite coupling factor to the PRM and SRM, actuators for PRCL and SRCL.

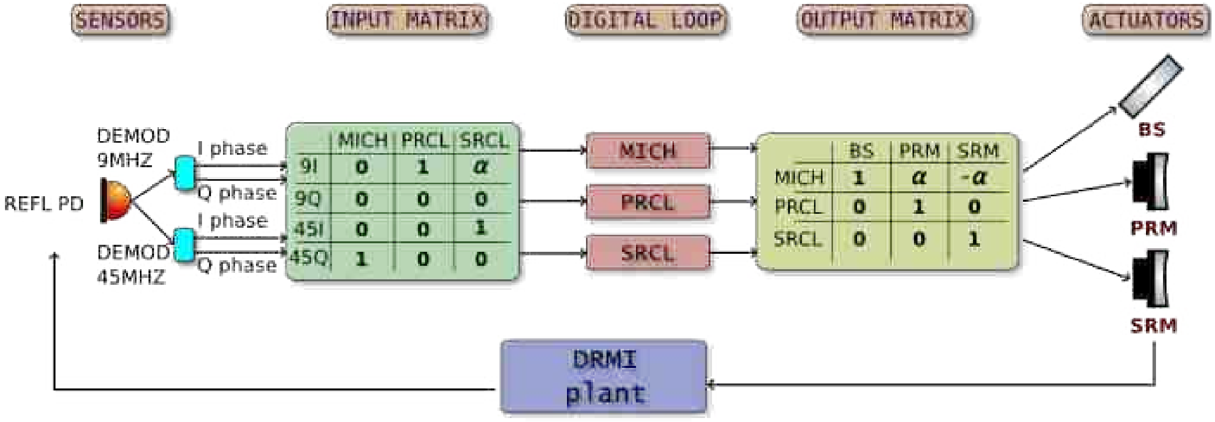

	MICH	PRCL	SRCL
9I	0	1	α
9Q	0	0	0
45I	0	0	1
45Q	1	0	0

	BS	PRM	SRM
MICH	1	α	$-\alpha$
PRCL	0	1	0
SRCL	0	0	1

Figure 4.11: The ideal signal flow for the control of the three DRMI DOFs. In the input matrix, the α parameter is the ratio of the PRCL response in REFL 45I to REFL 9I, in order to subtract PRCL contribution from SRCL sensing. In the output matrix, the α parameter is the geometrical factor needed to cancel the effect of actuation on the BS making PRCL and SRCL motion. This is $\sqrt{2}/2$.

4.2 Power-recycled Michelson Interferometer Sensing Matrix Measurement

The straightforward way to measure the sensing matrix is to choose a frequency above the UGF of the loops and apply a length excitation to an actuator for the DOF to be measured. Then we can read the signal strength in all sensors. It is preferable to choose different frequencies for the different DOFs such that the measurements can be done at the same time; not only for faster measurements but also for measuring the DOFs in the exact same conditions (e.g. the buildup in some cavity may vary on time scales of tens of minutes).

In the PRMI configuration, as shown in Figure 4.1, we have simplified the measurement by having only two DOFs, MICH and PRCL. The model then has to be changed to match this configuration by "removing" the SRM (in practice setting its losses to be the reflection coefficient and keeping the transmission coefficient to get the correct power measurement at the AS port). Also, we need to match as well as possible the input power and the modulation strengths used, so the expected numbers will be somewhat different from those in Table 4.2.

To measure the modulation strengths for the two sideband frequencies we used a scan of the OMC length in what is called a single-bounce configuration. In this configuration, none of the cavities are near resonance, and a small amount of the input power leaks to the OMC. By scanning the cavity length we can see many peaks in the transmitted power photodiode, as we reach the correct length for the resonance of the carrier, the sidebands or other higher order modes. The carrier is the largest peak, and the two sidebands are the next two largest peaks, and their ratio gives us the modulation strength for each sideband.

The results of this measurement are shown in Table 4.11. Variations from model of less than a factor of 2 is considered accurate enough for auxiliary degrees of freedom. On one hand, it is only important to precisely calibrate the GW readout signal, and on the other hand, if we find noise contributions which are within a factor of 2 from limiting the GW sensitivity it means something is wrong and must be investigated. Aside from the fundamental noise sources, all other noise contributions should be by design a factor of 10 at least from affecting DARM. The calibrations for the photodiodes and actuators are derived from their electronics chain design and the powers on the photodiodes are deduced from the DC power values.

Notably, the actuators used for these measurements were the ITMs and PR2 for MICH and PRCL respectively. This allowed us to notch the actuators in the feedback loops at the

Table 4.11: LSC sensing matrix in LLO PRMI sideband lock. Each DOF is shown twice, one being the measured element, denoted as"meas." and one being derived from the model. The phase difference is as measured, and is expected to be close to 90 degrees. The input power was 2.9W, adjusted in the model by a factor of 2 down, due to lower buildup in the PRC cavity (~ 30 vs ~ 60 for the 9 MHz sideband). The modulation strengths were 0.24 and 0.29 for the 9 MHz and 45 MHz sidebands respectively.

↓Sensor \ W/m →	MICH (meas.)	MICH	PRCL (meas.)	PRCL	Phase Δ deg
ASAIR 45	5.4e2	5.5e2	2.4e3	7.0e1	86
REFL 9	2.1e4	2.8e4	2.6e6	3.5e6	83
REFL 45	1.3e5	1.3e5	3.1e6	3.4e6	88
REFLAIR 27	6.8e3	1.6e3	5.6e5	1.6e5	81
REFLAIR 135	3.3e3	1.8e3	7.8e4	4.1e4	81

drive frequencies. Furthermore, the ITMs have to be driven differentially to create MICH motion and they must be matched to 1% or better in order to not create PRCL motion as well. This was especially important to do because the ITMs are weak actuators, and at the time of the measurement only the stage above the optic could be used. This means that the actuator strength drops as f^{-4}, and so a relatively low frequency had to be used for this drive (33 Hz), which is well below the PRCL feedback loop UGF (150 Hz).

With the above considerations, we can conclude that the REFL 9 and REFL 45 sensors match the model well for both DOFs, as well as the ASAIR 45 for MICH. The PRCL element for ASAIR 45 is much higher than the model, but this is to be expected because the model has very good contract defect ($\sim 10^{-12}$) while in reality, without any thermal compensation, the contrast defect was measured closer to 10^{-3}. The 3f photodiodes show a larger deviation from model, which is not yet understood. But the response is still within factor of 2 or at most 3, which allows us to successfully use these sensors for locking the DRMI DOFs.

4.3 Loop Couplings Modeling and Results

4.3.1 Simulink Model

As usual, in the real world, the idealized model doesn't always match measurements because there are other parameters involved, which may not be easy to model or even known beforehand. In the case of the DRMI sensing matrix, it was found that the orthogonality from the model (PRCL and SRCL in the same phase and MICH orthogonal to them) was not the reality. Furthermore, the MICH loop was designed to be the weakest, so the actuation decoupling to PRM and SRM was not applied since it was not necessary in the beginning of commissioning. Because these three loops are then coupled both in sensing and in actuation, we could not measure the sensing matrix by the intuitive procedure of applying an excitation to each loop and measuring the response in the sensors. Instead, I built a simulink model of the three loops, then measured the 3 by 3 transfer functions of the loops and optimized the sensing matrix to make them all match.

The results are shown in Figures 4.12 to 4.15. The open loop gain (OLG) measurements are taken as the ratio of two readouts around the excitation point at the error point of the digital loop. The unity gain frequencies are 7Hz, 150 Hz and 45 Hz respectively for MICH, PRCL and SRCL. The next three plots, showcasing the cross-couplings, are taken from excitation point of the loop being excited to error point of each of the three loops. For the same DOF (e.g. MICH to MICH) we expect that TF to be G/(1+G) and so 1 below the UGF. For MICH, this is not true because of extraneous PRCL coupling.

4.3.2 Sensing Matrix

Table 4.12 shows the sensing matrix derived from matching all 3 by 3 DOF transfer functions while Figure 4.16 shows the sensing numbers in radar chart form. Because the two sensors used in the feedback loops (REFL 9 and REFL 45) do not have the expected relative DOF phasing from the model, there are additional cross-couplings which explain the 3x3 transfer functions. The REFL9 elements for MICH and SRCL are so much smaller than PRCL that the REFL9 sensor can only be used for PRCL, as expected. However, there is no way to rotate the axes such that we can use either the I or Q phase (the 0° and 90° vectors) for only MICH or only SRCL in REFL45 without getting a high contribution from the other two DOFs. As such, the desired model input matrix shown above might have to be modified.

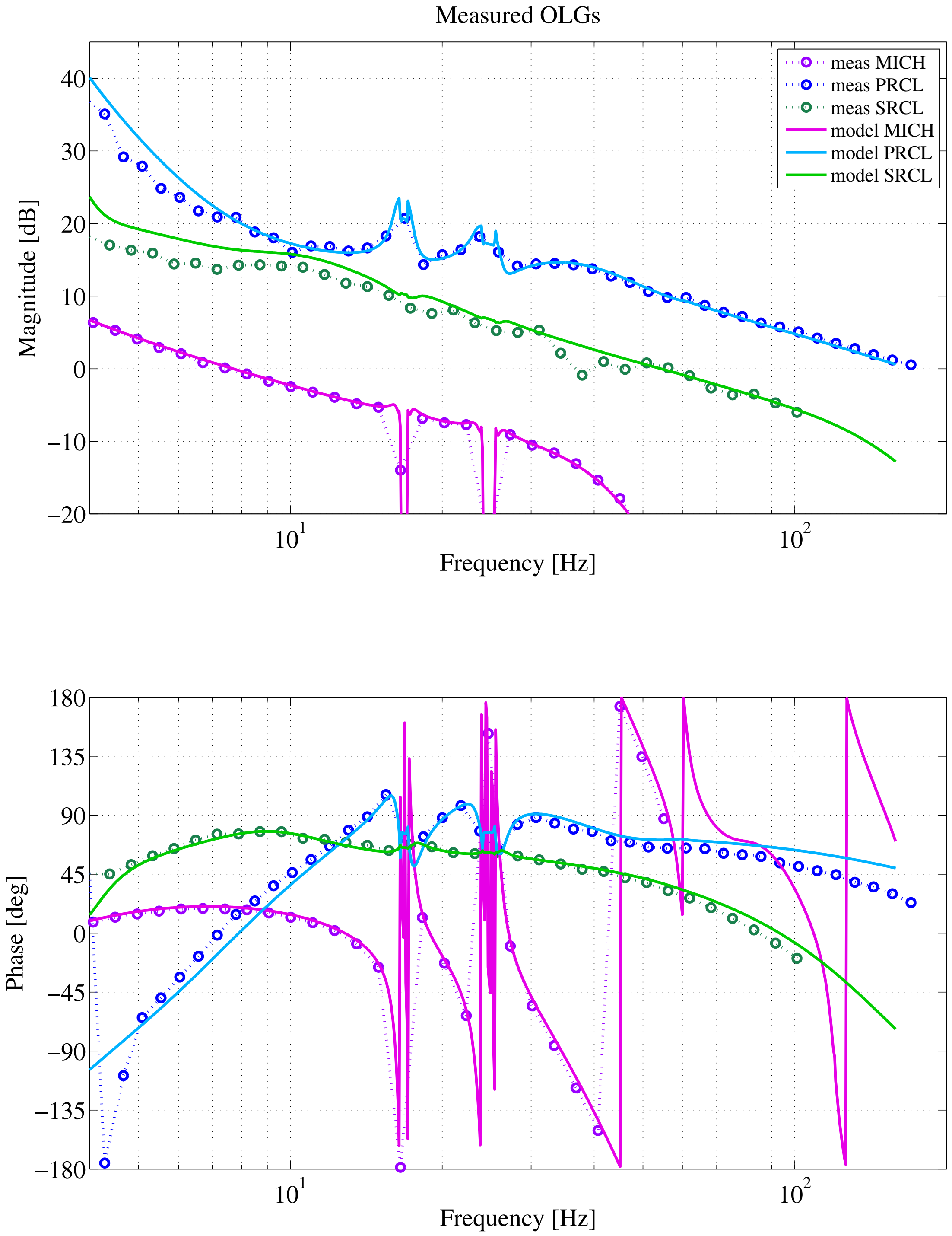

Figure 4.12: Measured and modeled open loop gains (OLG) of the three DRMI DOFs. Note that the “flattening” of the PRCL and SRCL transfer functions at lower frequencies is due to the uncompensated BS MICH actuation.

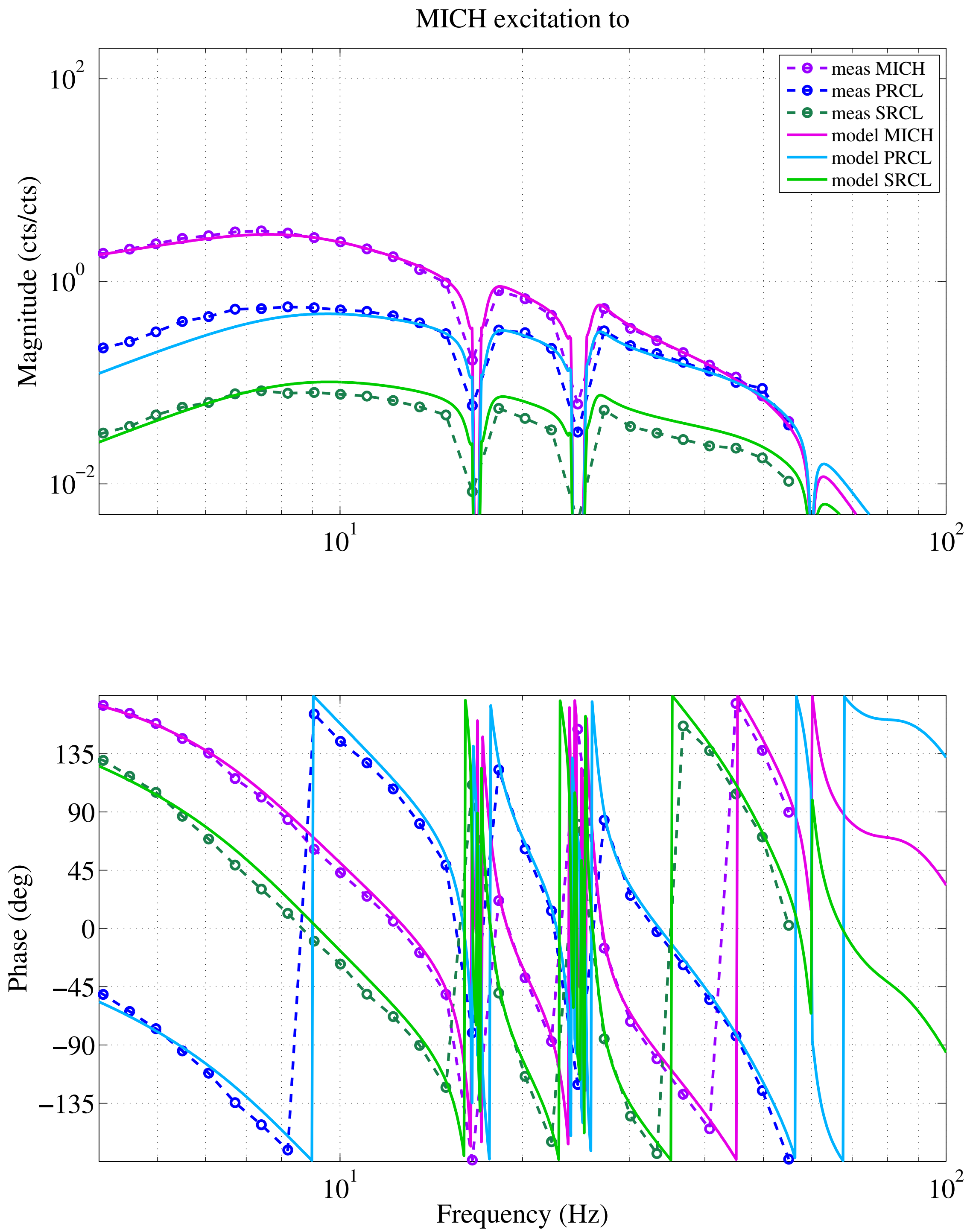

Figure 4.13: Measurement and model comparison of MICH drive effect on all three loops. The MICH to MICH TF is not 1 below the UGF, and so it means another loop is acting on the MICH sensing (specifically PRCL).

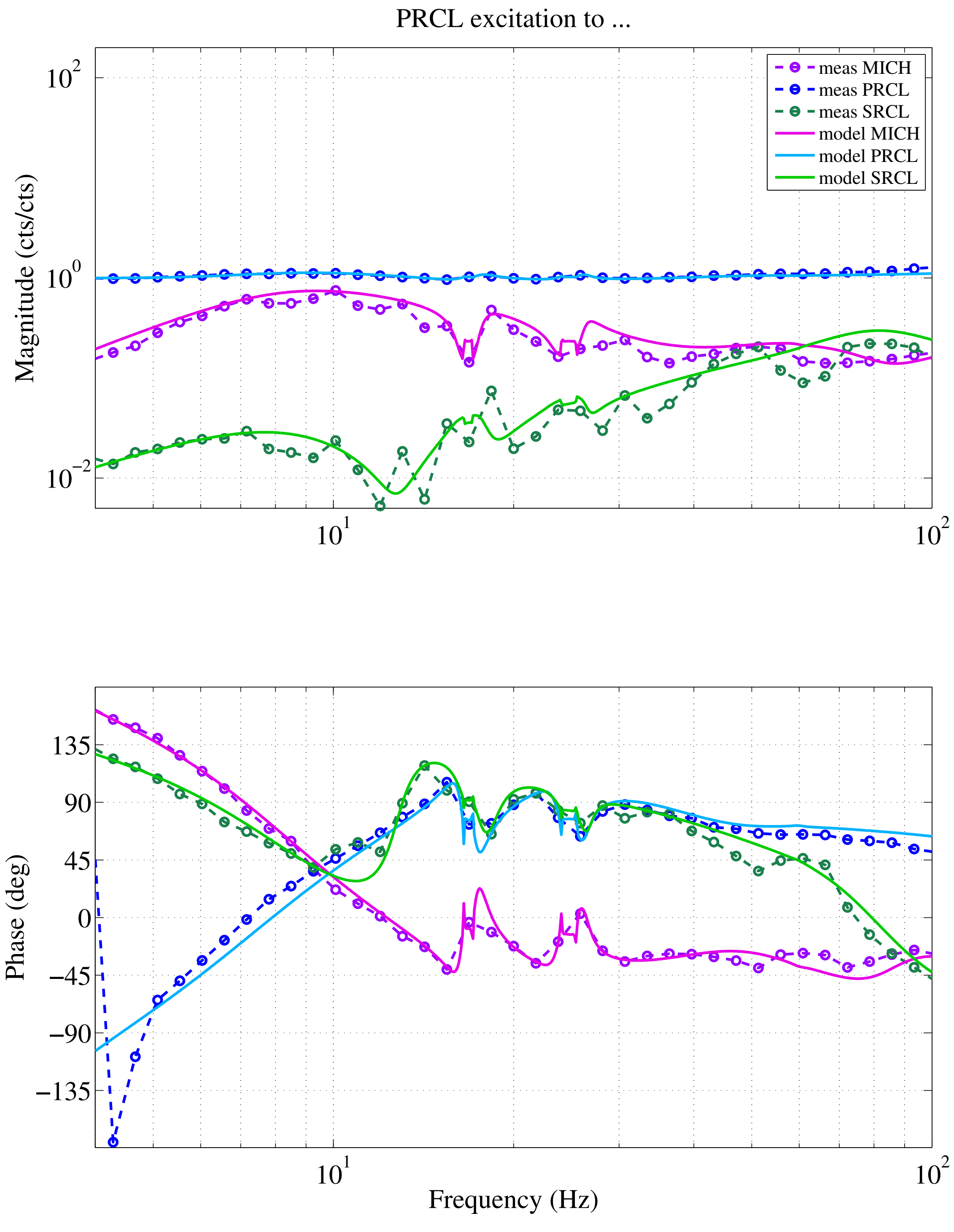

Figure 4.14: Measurement and model comparison of PRCL drive effect on all three loops. We can see that the PRCL to MICH coupling is large, due to sensing non-diagonalization.

One known issue with the detector at the time of the measurements in Figure 4.12 was an imbalance in the lenses of the two ITMs, which results in a large contrast defect

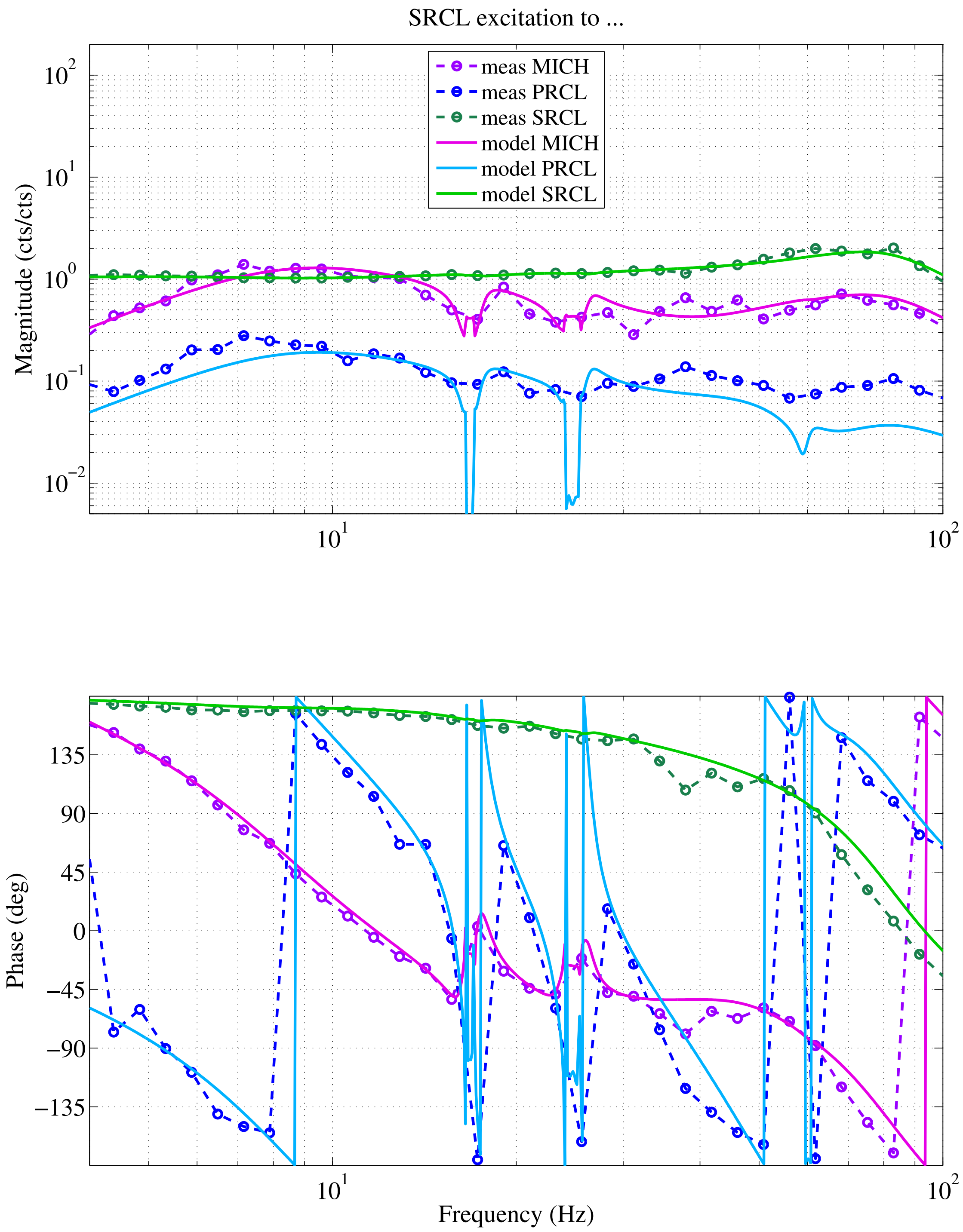

Figure 4.15: Measurement and model comparison of SRCL drive effect on all three loops. The MICH contributions here is large, and is in fact magnified by the PRCL to MICH coupling.

Table 4.12: Measured sensing matrix calculated from matching the 3x3 DOF transfer functions for the DRMI with input power of 1.8W and modulation depths of 0.24 and 0.29 for the 9 and 45 MHz sideband frequencies respectively. The magnitudes are expressed in W/m and the phases in degrees.

Sensor→	ASAIR 45	REFL 9	REFL 45	REFLAIR 27	REFLAIR 135
MICH meas.	8.2e3	1e4	7.2e5	3.2e4	1.9e4
MICH model	4e3	1.6e4	5.6e5	5.3e3	6.1e3
PRCL meas.	1.7e3	3.6e6	1.5e6	7.4e5	3.4e4
PRCL model	2.6e2	6.0e6	1.4e6	2.3e5	1.5e4
SRCL meas.	20	4e3	8.0e4	2.8e3	2.8e3
SRCL model	30	7.0e3	1.9e5	1.2e3	2.2e3
PRCL-MICH ϕ meas.	34	48	102	71	117
PRCL-MICH ϕ model	88	22	91	61	90
PRCL-SRCL ϕ meas.	58	23	117	163	142
PRCL-SRCL ϕ model	1	179	1	5	1

($\sim$ 1e-3 at the time) and a large sideband imbalance (the upper and lower sidebands do not have the same buildup). The sideband imbalance was roughly estimated at 20%. The thermal compensation system was engaged to fix this, by applying central heating to one of the ITMs for better mode matching. The contrast defect was reduced by about a factor of 10 and the sideband imbalance was measured to be close to 1%. I then remeasured the sensing matrix, and the results were very different from the first measurement, and much closer to modeled phase differences. The model versus measurement transfer functions are shown in Figures 4.17 to 4.20. The re-derived sensing matrix is shown in Table 4.13 with the corresponding radar chart in Figure 4.21.

The important question to answer is if this difference between model and measurement is a problem for either the stability of the loops or the noise introduced ultimately in DARM, the GW readout. Geometrically, of these three auxiliary DOFs we are studying, only MICH has direct coupling to DARM, which is inversely proportional to the finesse of the arm cavities ($\sim$ 450). The other DOFs, PRCL and SRCL, should couple by at least a couple orders of magnitude less. So the two items to consider are the stability of the SRCL

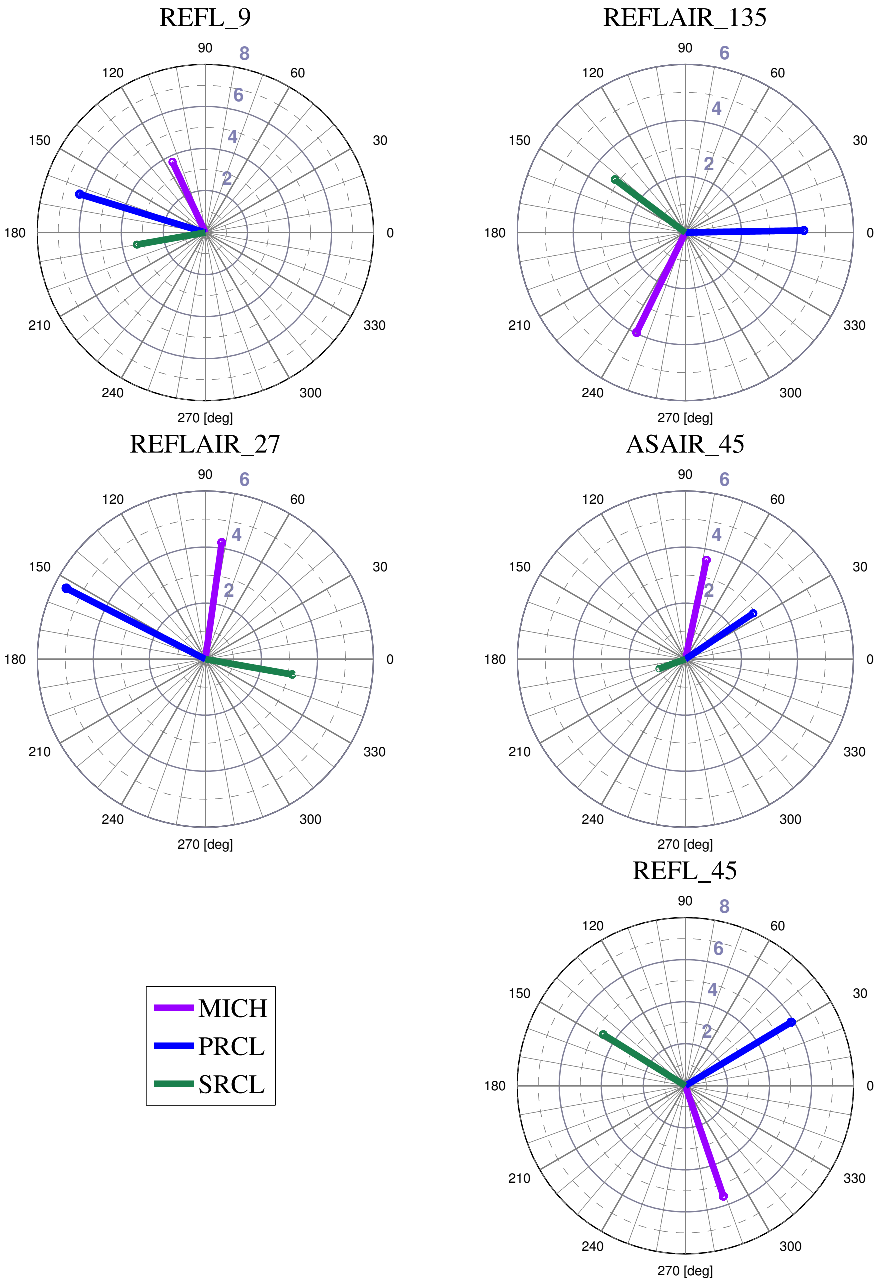

REFL_9

REFLAIR_135

REFLAIR_27

ASAIR_45

REFL_45

Figure 4.16: DRMI sensing matrix in radar form of Table 4.12. The amplitude is logarithmic and the phase is in degrees. The amplitude scale may vary and is labelled every 2 orders in gray.

loop, which is the hardest to sense (smallest element), and the noise in MICH introduced by these extraneous couplings.

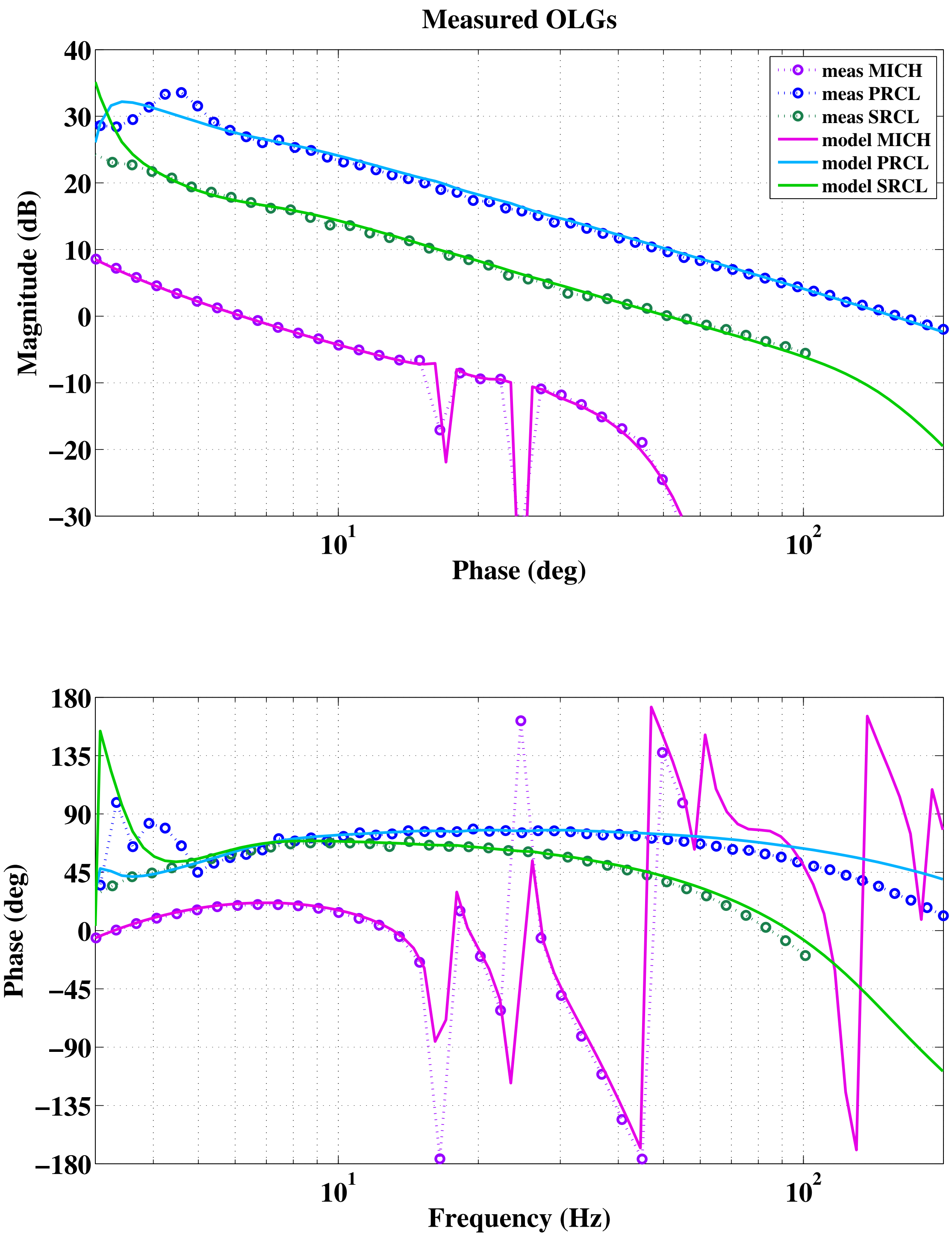

Figure 4.17: Measured and modeled open loop gains (OLG) of the three DRMI DOFs post contrast defect improvement.Notice that the loops shapes of PRCL and SRCL are much closer to the expected 1/f of their designed shape when compared to Figure 4.12.

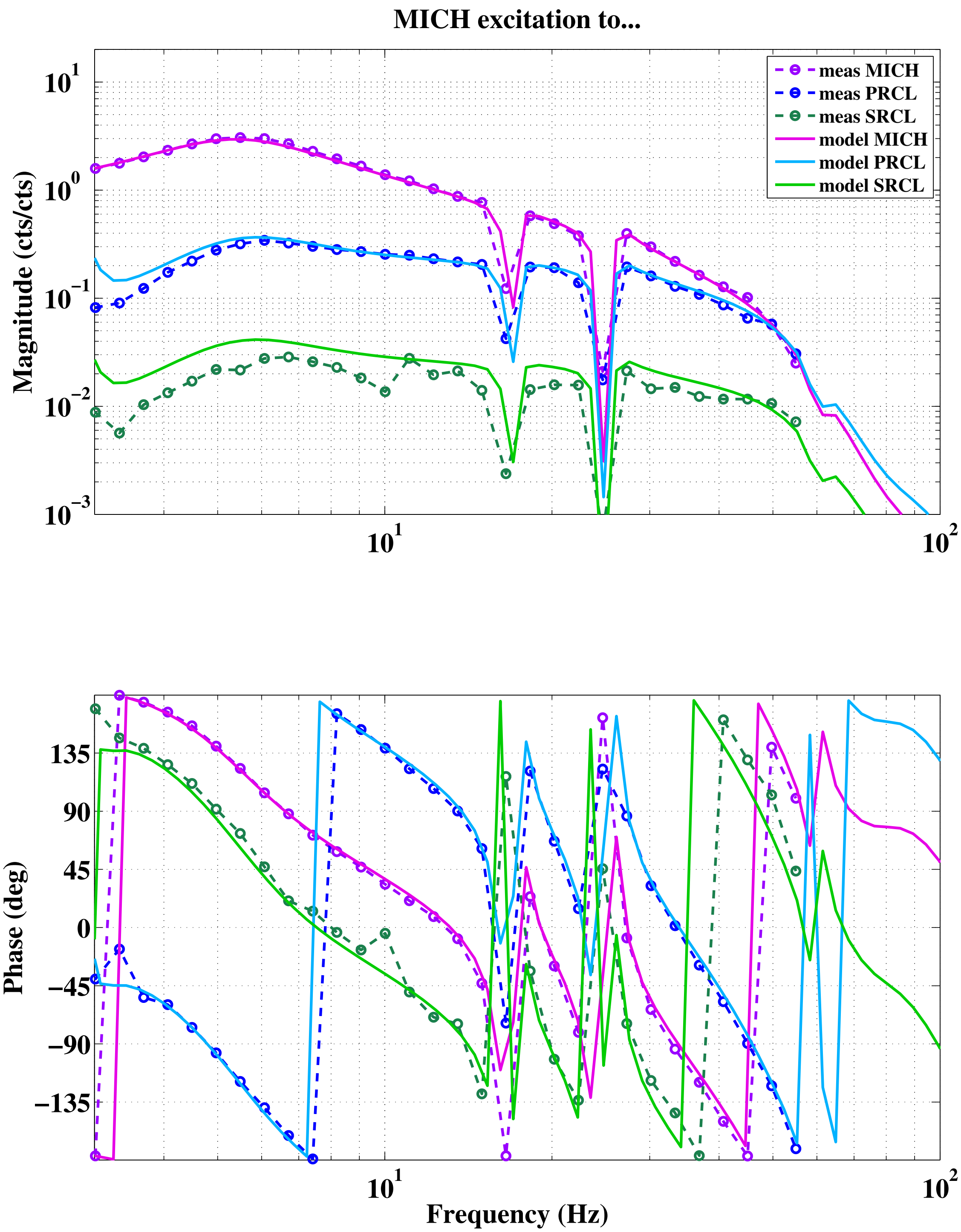

Figure 4.18: Measurement and model comparison of MICH drive effect on all three loops post contrast defect improvement. Notice that the excitations to PRCL and SRCL are smaller indeed, as well as the deviance from 1 of the MICH transfer function when compared to Figure 4.13.

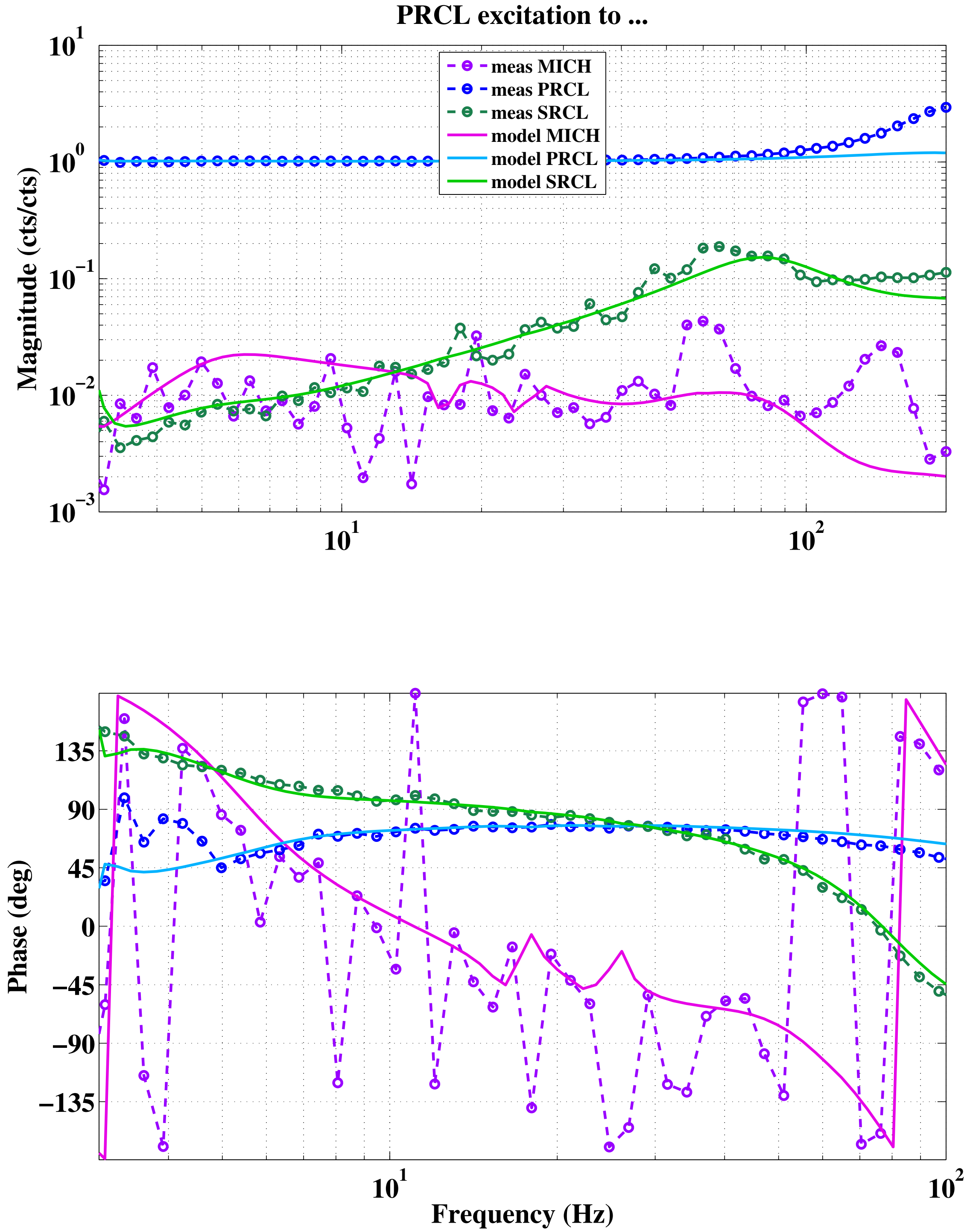

Figure 4.19: Measurement and model comparison of PRCL drive effect on all three loops post contrast defect improvement. Notice that the coupling to MICH is much smaller due to the reduction of PRCL in REFL45Q. Also, the coupling to SRCL is a bit smaller when compared to Figure 4.14.

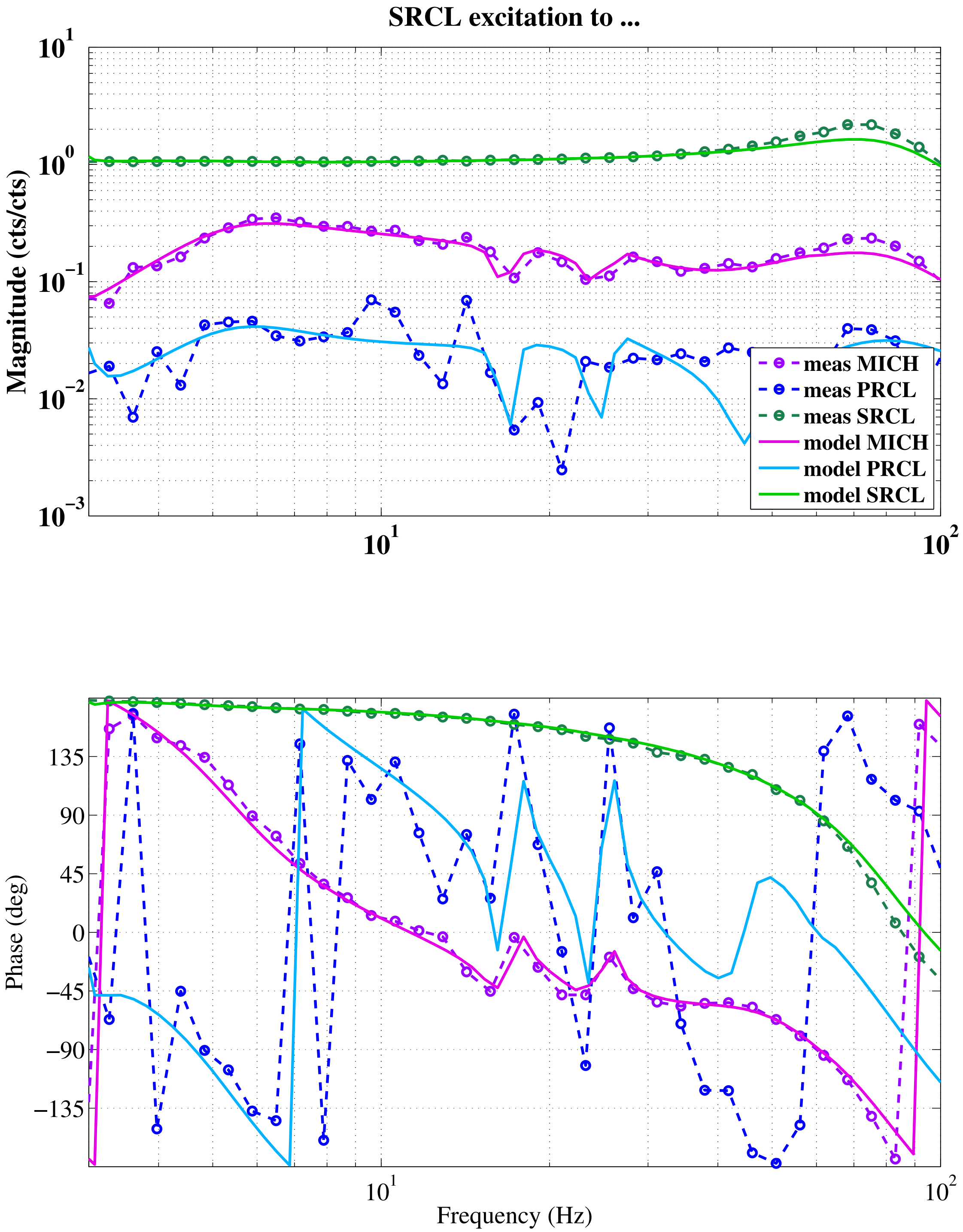

Figure 4.20: Measurement and model comparison of SRCL drive effect on all three loops post contrast defect improvement. Notice that the coupling to PRCL is much smaller, and the coupling to MICH is greatly reduced when compared to Figure 4.15. This is due to having MICH and SRCL much more orthogonal in the sensing.

Table 4.13: Measured sensing matrix calculated from matching the 3x3 DOF transfer functions for the DRMI with input power of 1.8W and modulation depths of 0.24 and 0.29 for the 9 and 45 MHz sideband frequencies respectively. The magnitudes are expressed in W/m and the phases in degrees. The contrast defect improvement was implemented for this measurement.

Sensor→	ASAIR 45	REFL 9	REFL 45	REFLAIR 27	REFLAIR 135
MICH meas.	1.5e4	5.8e3	7.8e5	2.4e4	4.2e4
MICH model	4e3	1.6e4	5.6e5	5.3e3	6.1e3
PRCL meas.	3.2e2	3.6e6	1.1e6	3.8e5	7.0e4
PRCL model	2.6e2	6.0e6	1.4e6	2.3e5	1.5e4
SRCL meas.	82	6e3	1.1e5	4.2e3	6.4e3
SRCL model	30	7.0e3	1.9e5	1.2e3	2.2e3
PRCL-MICH ϕ meas.	125	71	108	69	90
PRCL-MICH ϕ model	88	22	91	61	90
PRCL-SRCL ϕ meas.	102	169	-159	8	3
PRCL-SRCL ϕ model	1	179	1	5	1

4.3.3 Decoupling Solutions

Since in the full interferometer configuration, the sensing of these three DOFs is done through a similar setup with the POP sensor (using POP 9 for PRCL and POP 45 for MICH and SRCL), we can propagate the DRMI solution to the full interferometer setup. It only requires a few additional measurements, similar to the ones used for the Simulink loop modeling above. Measurements have confirmed that the cross-couplings are similar in full interferometer lock.

Further, we have to consider decoupling the actuation. If the MICH, PRCL and SRCL actuators were the same, this issue would be very simple to resolve, as shown in the output matrix of Figure 4.11: we simply put in the geometrical factor of BS motion to PRCL and SRCL motion. If we pick the BS positive motion to be north-west, and the PRM and SRM towards the BS, then 1nm of positive BS motion will change the PRC length by -$\sqrt{2}/2$ nm and the SRC length by $+\sqrt{2}/2$ nm. So we would want to send the MICH feedback signal to PRM and SRM as well, with the opposite sign of their corresponding factors.

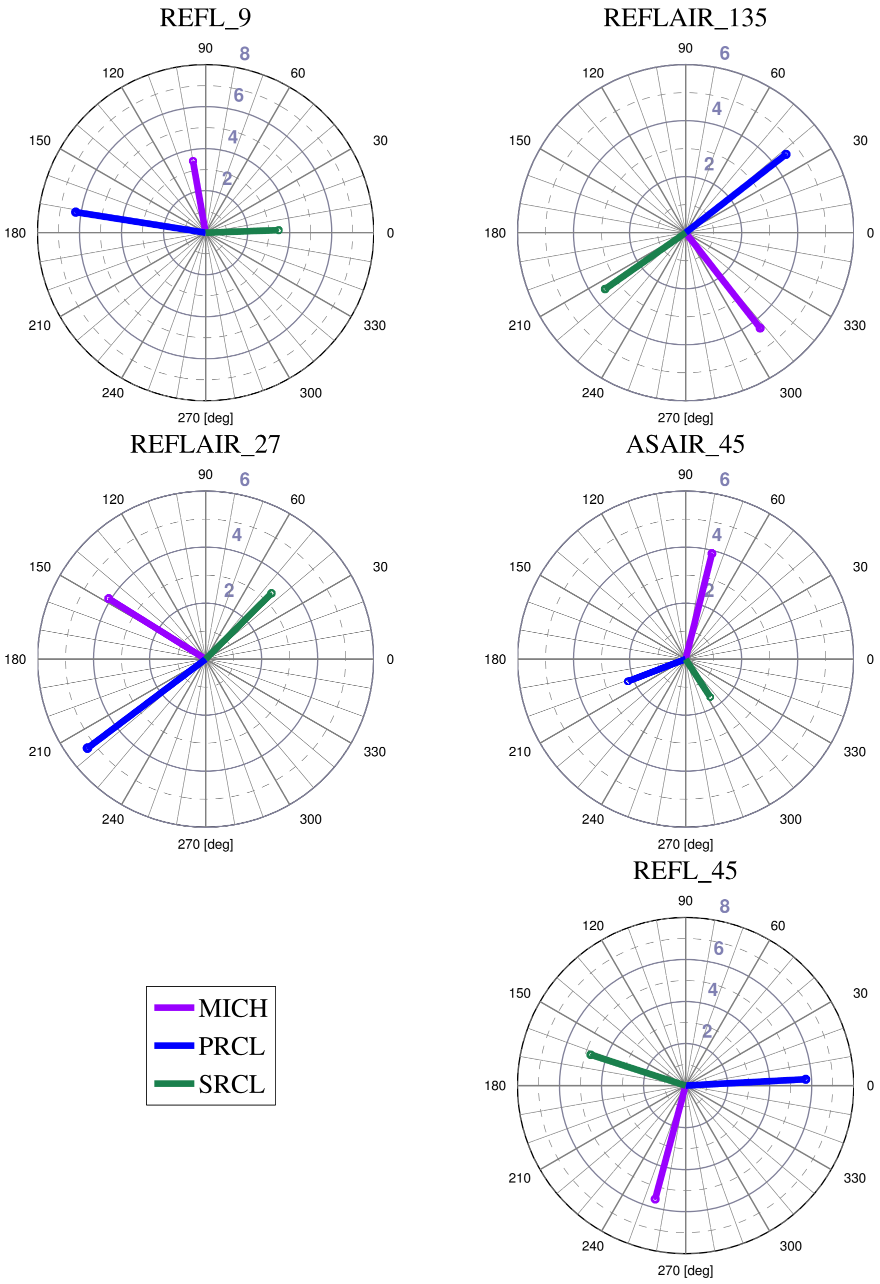
REFL_9

REFLAIR_135

REFLAIR_27

ASAIR_45

REFL_45

Figure 4.21: DRMI sensing matrix in radar form of Table 4.13. The amplitude is logarithmic and the phase is in degrees. The amplitude scale may vary and is labelled every 2 orders in gray.

However, while the suspensions and electronics are the same for PRM and SRM (HSTS = HAM Small Triple Suspension), they are not the same for the BS (BSFM = Beam Splitter and Folding Mirror suspension, also a three stage suspension). Furthermore, the BS does not have actuation on the optic itself, only on the stage above, so different filtering is required for these two suspension types. Furthermore, the drive to the suspension goes to the lowest stage first and then to the higher stages, such that we cannot choose to drive only the middle stage with one input while driving the bottom stage with another.

A simple solution is then to not drive the PRM and SRM but other optics in the PRC and SRC which would serve the same purpose, such as PR2 and SR2 (which are also of the HSTS type). Then we could turn off their bottom stage and only drive the middle stage (as is the "forced" case for the BS) and employ the same filters as for the BS suspension. By implementing two off-diagonal elements in the actuator output matrix equal to the ratios of the driver strengths, a factor of 10 was achieved, as shown in Figure 4.22. If needed, these factors can be tuned to better than a factor of 10, and a frequency dependent matching could be implemented easily.

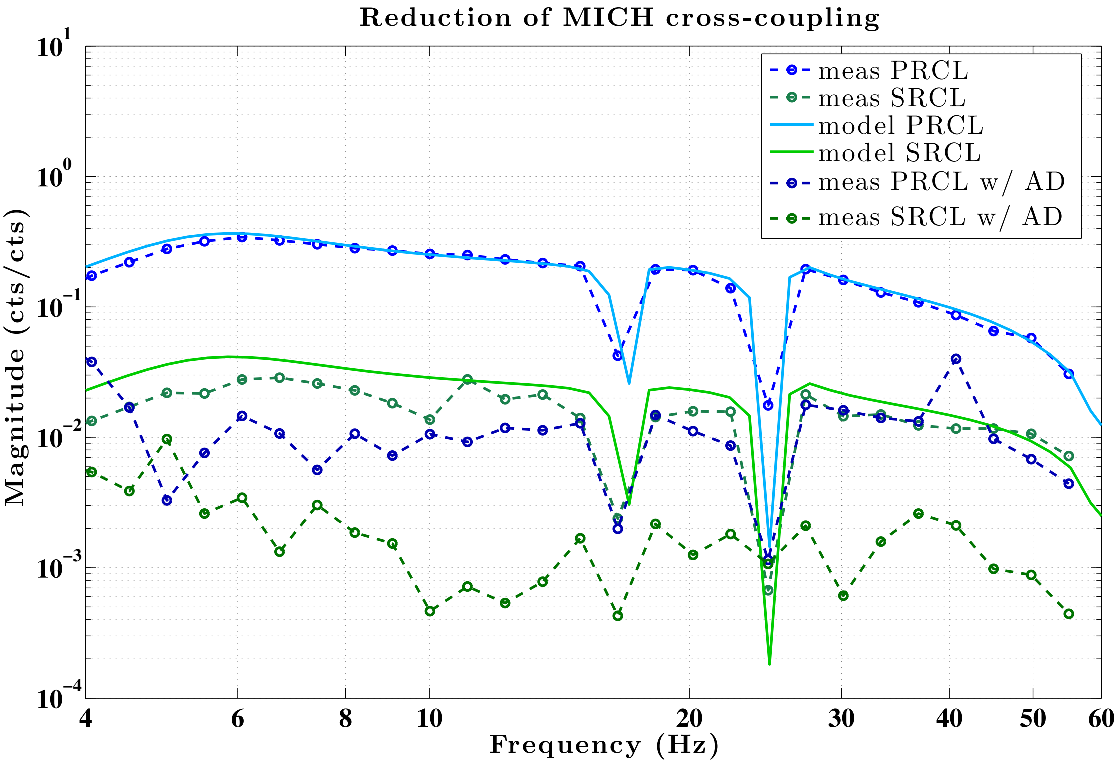

Figure 4.22: Improvement in MICH cross-coupling to PRCL and SRCL by implementing output matrix coefficients to counteract the geometrical coupling due to driving the BS. The MICH drive was sent to PR2 for PRCL reduction and SR2 for SRCL reduction. The measurement and model traces are the same as in Figure 4.18; "w/ AD" stands for actuation decoupling.

In order to decouple the sensing, if we have the modeled phasing of signals such that MICH is orthogonal to PRCL and SRCL in the sensor to be used (REFL45 or REFL135, or POP45 for full interferometer), then we are done and can employ the simple solution explained above (MICH in the Q phase, SRCL in the I phase with PRCL cancellation, and PRCL on a different sensor). The second set of measurements after the TCS implementation would allow us to do so. In the case of the first set of measurements, we would have to consider some phase of the sensor used for MICH and SRCL (e.g. REFL 45) to minimize the cross-coupling of PRCL and SRCL into MICH. Given that the PRCL element is so much bigger than the SRCL one, the simplest solution is to phase the sensor to minimize the PRCL contribution (e.g. rotate the phase such that PRCL is all in I phase) and live with the smaller SRCL coupling. Then in SRCL we could implement an off-diagonal element in the input matrix using REFL 45Q to minimize the MICH to SRCL coupling and recalculate the element canceling the PRCL coupling using, for example, REFL 9.

4.4 Macroscopic Length Modeling and Measurements

We would like to be able to measure the macroscopic lengths of our power recycling cavity (PRC), signal recycling cavity (SRC) and Schnupp asymmetry to ensure the optics have been installed close enough to the designed position in order to achieve the desired optical performance. We will now showcase how to do this for the PRC and then extend the model to the SRC and Schnupp asymmetry.

Firstly, we have to set some thresholds of what is acceptable in terms of length variation from the perfect designed length. One simple requirement to consider is that if the PRC length is not optimal, the sidebands will not be fully transmitted through the PRC. From modeling we obtain that the PRC length has to be within less than 5mm of the design value in order to transmit 90% of both the 9MHz and 45MHz sideband power.

In a simple Optickle configuration (no control loops) of the DRMI, an offset of 5mm in the PRC length does not affect the sensing matrix much. Some signals may lose up to 1%

of strength and the diagonalization of the degrees of freedom remains the same relative to each other.

However, there are many other factors which can vary, such as other degree of freedom lengths, etc, so we feel that a few mm should be a good, conservative but also attainable goal. We would like to measure the PRC length to a precision of some fraction of a mm. This number comes from full interferometer modeling, where changing the PRC length by 1mm does not affect the noise budget visibly. Offsetting the PRC length by 5mm changes the full interferometer sensing matrix and results in some higher couplings on the order of a few percent.

We can model the PRC as a Fabry-Perot cavity where the input mirror has 3% transmission (PRM) and the end mirror has 0.14% transmission (Michelson formed by the ITMs and BS). We will refer to the two phases of the demodulated Pound-Drever-Hall signal as REFL_I and REFL_Q. For locking, the signal in one quadrature is maximized, such that only REFL_I (pick one) has a slope passing through resonance. If the macroscopic length L of the cavity is perfect, then whether we lock on carrier or sideband, the signal will be maximized in the same quadrature, differing only by a sign flip (π phase flip).

If L is not perfect, then say we maximize the signal in REFL_I in the carrier lock. When switching to a sideband lock (achieved only by a microscopic length change), the signal will no longer be maximized in REFL_I and we will see some signal in REFL_Q. Figure 4.23 shows an analytical calculation of the PDH signals for a Fabry-Perot cavity comparable to the aLIGO PRC, where $t_1 = 0.03$ and t_2=0.014 and Ω=2*π*45,497,355 Hz.

For a simple Fabry-Perot cavity we can define the reflection coefficient F:

$$\mathrm{F}(\omega) = \frac{\mathrm{r}_1 - \mathrm{r}_2 \mathrm{e}^{-2\mathrm{i}\omega \mathrm{L}/\mathrm{c}}}{1 - \mathrm{r}_1 \mathrm{r}_2 \mathrm{e}^{-2\mathrm{i}\omega \mathrm{L}/\mathrm{c}}} \tag{4.1}$$

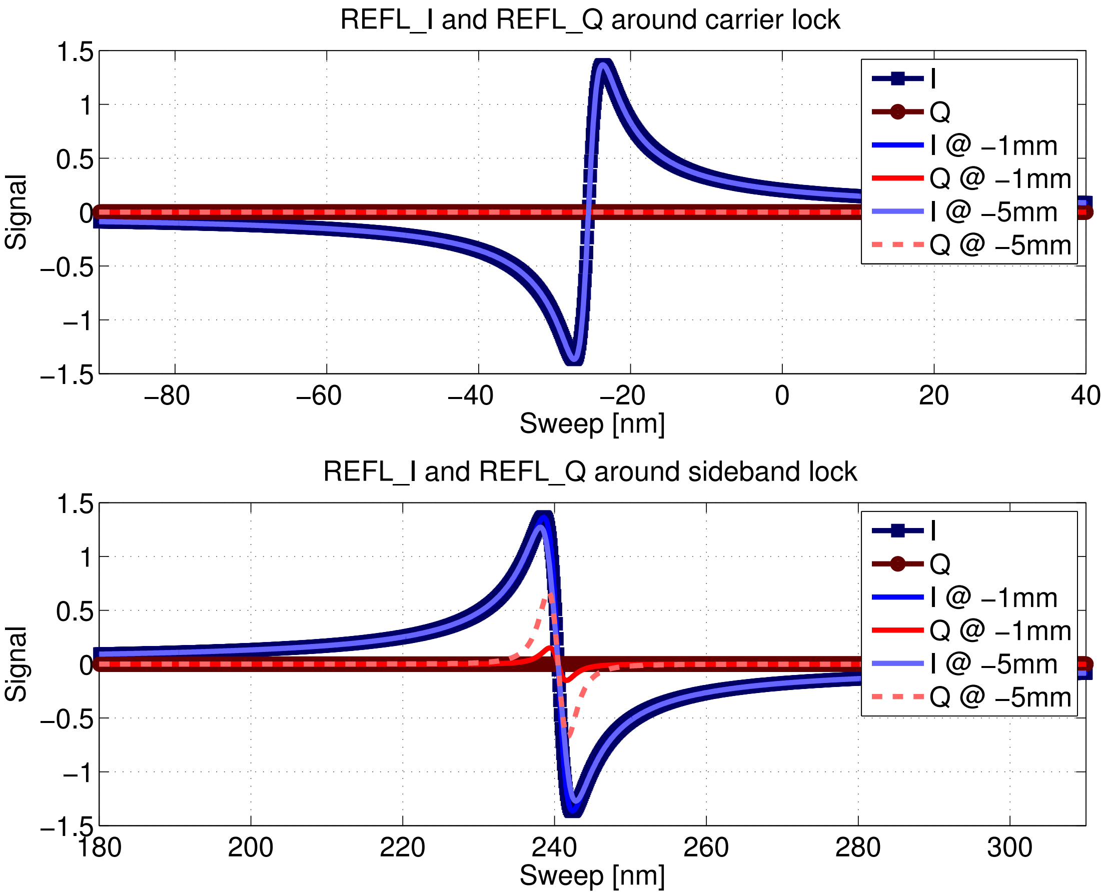

Figure 4.23: Difference in REFL_I and Q passing through carrier lock (top plot) and sideband lock (bottom plot) if the length of the cavity is perfect or (cyan and magenta) if the length is 5mm off from perfect (blue and red)

And then the demodulated signals can be written as (ignoring a mutiplicative overall factor):

$$\begin{aligned} REFL\_I &= \Im[F(\omega)F^*(\omega+\Omega) - F^*(\omega)F(\omega-\Omega)] \\ REFL\_Q &= \Re[F(\omega)F^*(\omega+\Omega) - F^*(\omega)F(\omega-\Omega)]. \end{aligned} \tag{4.2}$$

If we apply this to the more realistic Optickle model of the PRMI, with 10W input power (coming out of the IMC), we see this effect at the REFL_45 PD, as shown in Figure 4.24. Plotted are several calculations such as the one above for various macroscopic length offsets of the PRC, from which the phase of the I and Q signal content was extracted and plotted.

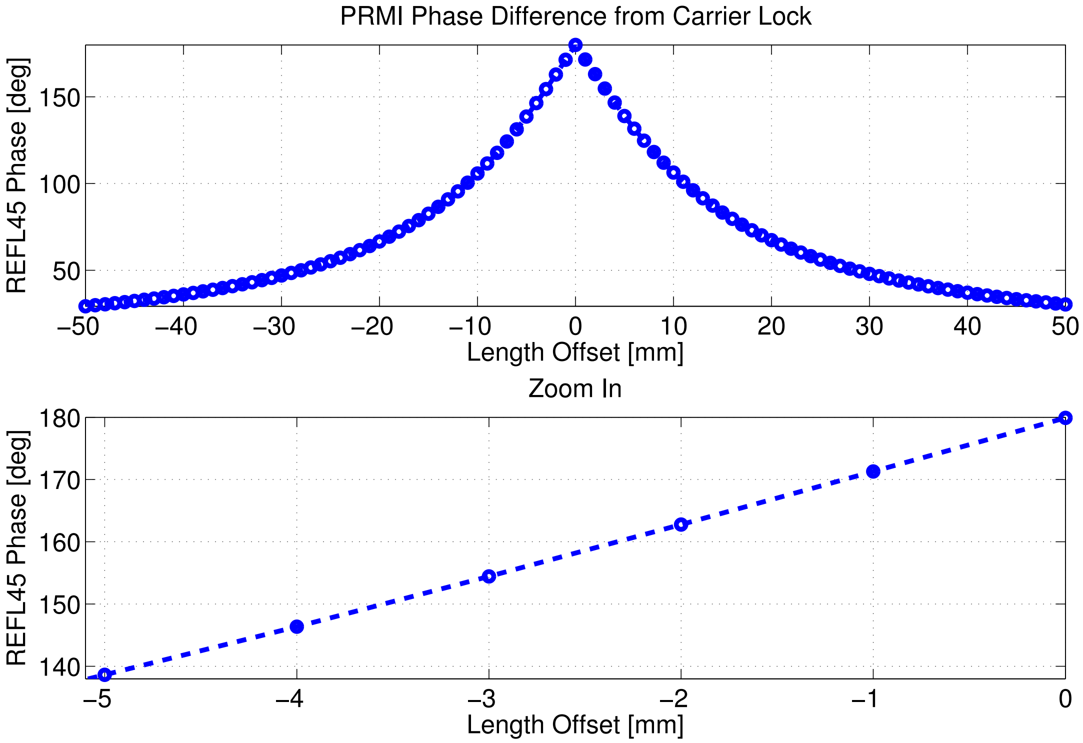

Figure 4.24: Variation of phase between carrier lock and sideband lock (expected 180 if perfect PRC length) as we vary the length of the PRC in the Optickle model; the bottom plot is just a zoom in of the top plot.

So we expect to see about 8° of phase for each mm we are off in length of the PRC. In order to resolve a measurement to 4° of phase, we have to maximize REFL_I to about 1% error which is easily done. So we can measure the PRC length to the level of half a mm, or even a bit less.

For measuring the SRC length, the best comparison is between the DRMI locked on sideband and the PRMI locked on sideband. The PRMI phasing will not change with SRC length, of course, while the DRMI will. Since the 45 MHz sideband is resonant in the SRC, it will be the most affected so the best sensor to use is again REFL 45. Using the Optickle model, we obtain the plot in Figure 4.25 showing that the slope is approximately 0.6 degrees of change per mm offset in SRC length. This measurement is not as accurate as the one for the PRC, but the SRC length requirements are less strict since it is a low finesse cavity.

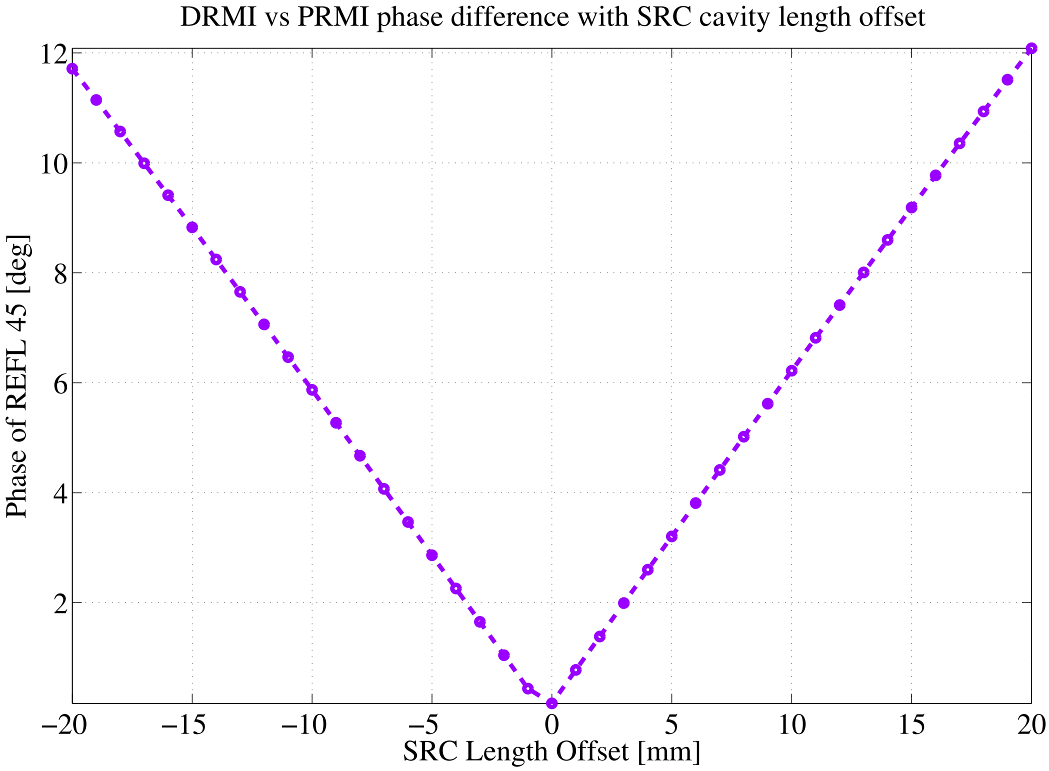

Figure 4.25: Variation of phase of REFL45 in DRMI lock compared to PRMI lock (expected 0 if perfect SRC length) as we vary the length of the SRC in the Optickle model.

For measuring the Schnupp asymmetry, we can employ a few other configurations, such as the low finesse cavities formed by the PRM and one of the ITMs. These are referred to as PRX (PRM + ITMX) and PRY(PRM + ITMY). They are ideal because the Schnupp asymmetry is between the distances from the BS to the two ITMs. Similarly, we can use as a cross-check the equivalent cavities formed by the SRM and the ITMs, SRX and SRY, but they are much weaker cavities. Figure 4.26 shows the phase variation in PRX and PRY as the Schnupp asymmetry is changed.

Measurements were performed using these methods by D. Martynov and L. Barsotti [59]. The results found are shown in Table 4.14. While the results are encouraging and we believe that we can estimate the phase phase measurement to a fraction of a degree,

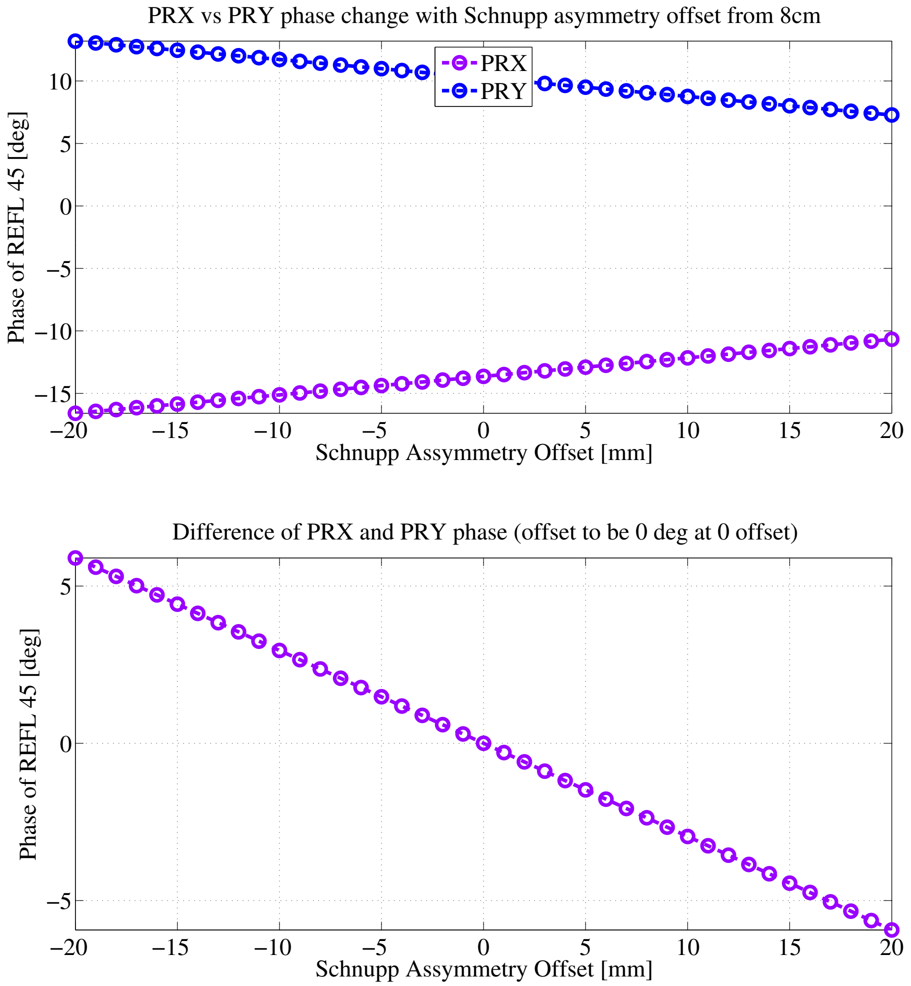

Figure 4.26: Variation of phase of REFL45 in PRX and PRY configurations as we vary the Schnupp asymmetry in the Optickle model. The bottom plot shows the difference between the two with an offset to make it 0 at perfect length. The 0 phase corresponds to a PRMI or DRMI lock.

resulting in sub-mm precision, we don't fully understand the systematics. These measurements were performed before the contrast defect reduction, so the sideband imbalance might change the relation entirely. In the future we plan to repeat these measurements and furthermore try to model the effects of sideband imbalance on this measurement.

In this chapter I have shown that we can use optical as well as loop modeling to check the sensing matrix of the interferometer and assess the cross-couplings of the DRMI degrees of freedom. While in the end the sensing matrix is close to model and design, we did not anticipate the large effect that a high contrast defect would have on the performance of

Table 4.14: Lengths measured by phase methods

↓Length	Difference from perfect	Configs Used
PRCL	1mm	PRX vs PRY; PRMI sb vs PRMI car
SRCL	3mm	SRX vs SRY
Schnupp	1mm	PRX vs PRY; SRX vs SRY

the DRMI, as can be seen between the two measurements presented. Using a combination of the various configurations attainable within the DRMI, I have devised a method to measure the three macroscopic lengths in the DRMI (the PRC cavity length, the SRC cavity length and the Schnupp asymmetry) which have to be within a few mm of nominal for the resonance conditions of the various optical cavities to be satisfied.

CHAPTER 5
DUAL-RECYCLED MICHELSON INTERFEROMETER (DRMI): NOISE MODEL AND MEASUREMENTS

5.1 Noise Budget Introduction

We wish to quantitatively understand what limits the sensitivity of the detector in the detection frequency range (10 Hz - 7 KHz). In different frequency bands, different sources may be the dominant noise terms. This is especially important in the commissioning phase of the detector, since reaching the design sensitivity is an incremental process achieved by identifying and mitigating expected or unexpected noise contributions from the various components of the detector. In Figure 5.1 we reproduce the designed advanced LIGO full interferometer noise budget shown in Chapter 2. Each of these noise sources will have to be measured in order to assess if their contribution is acceptable i.e. does not deteriorate the instrument sensitivity.

We can draw the conclusion that there are three fundamental limitations to the Advanced LIGO sensitivity:

- seismic noise at low frequencies, which falls off as $\sim \mathrm{f}^{-11}$ due to the several stages of seismic and suspension isolation;
- thermal noise and radiation pressure at middle frequencies, depending on the mirror quality and mass;
- and shot noise at high frequencies, depending on the amount of power circulating in the arms.

Considering the installation schedule of Advanced LIGO at the Livingston observatory of installing all corner station components first and end stations later, it was beneficial to produce similar calculations for the simpler configuration of the DRMI. The noise couplings are not the same as the ones for the full interferometer due to the different resonant conditions as explained in Chapter 2, but the DRMI is the most sensitive configuration

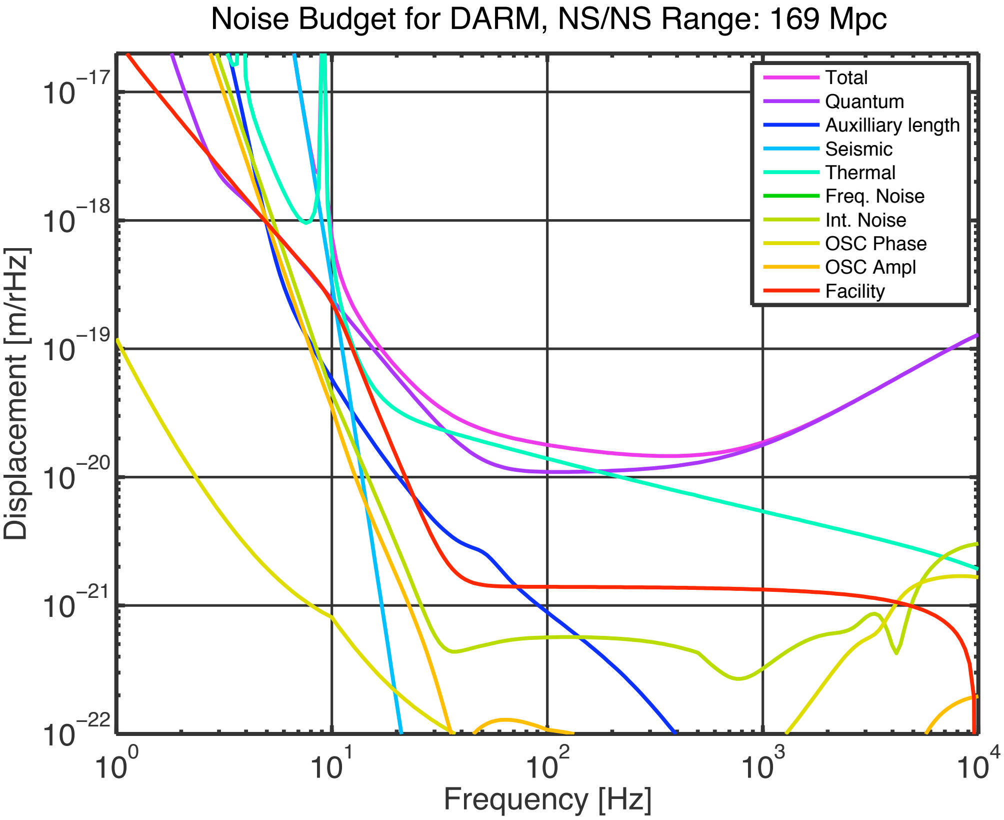

Figure 5.1: Advanced LIGO design noise budget [4]

before the full interferometer. As such, noise sources too small to measure independently for each subsystem could now be measured. The model was also refined with later known parameters of the optics. It is vital to assess any unexpected noise sources or unexpected couplings early on, and the DRMI allows for the best configuration for this. The measurements I will present will not be of the best performance, but chosen to showcase some of the issues the detector has run into and that were addressed early on.

5.2 Model Setup and Predictions

The modeling is done in Optickle, the same as the sensing matrix calculations in Chapter 4, but adding the feedback control loops using an add-on LIGO specific code named Lentickle developed by Nicolas Smith-Lefebvre [60]. The code can calculate transfer functions from any point to any point in the system (e.g. from control point to error point of loop) and so noise from various sources can be propagated to the desired DOF taking into account all cross-couplings. Figure 5.2 shows an example of such a noise budget with 5W input power to the DRMI.

5.2.1 DRMI Noise Budget

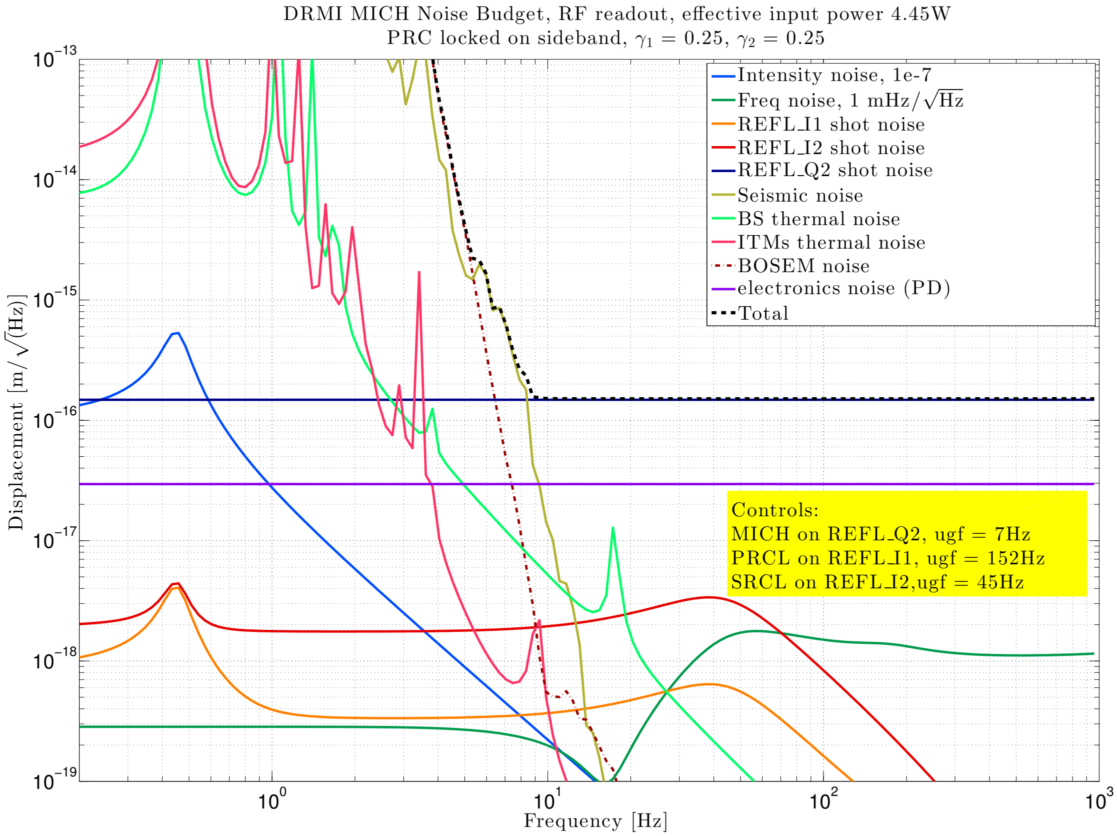

Figure 5.2: Modeled DRMI noise budget for MICH, including the three feedback control loops with current UGFs. The shot noises of the used sensors are propagated through the loops of the ideal model. The input power is 5W but input optics losses reduce the effective power to 4.45W.

Noise can enter through various paths and can manifest itself as optic motion or laser amplitude or phase fluctuations. The general approach is to use to the model to calculate the transfer function from the source of the noise to the desired DOF displacement. The details of the noise calculations are as follows:

- intensity noise: relative intensity noise (RIN) is injected using an amplitude modulator (AM) at the input to the DRMI by multiplying this noise by the transfer function from this AM to the MICH DOF. I use 10^{-7} as a baseline noise input;
- frequency noise: similar to intensity noise, a phase modulator (PM) is used to inject frequency noise. 1 mHz/$\sqrt{\text{Hz}}$ is used as input noise which is a reasonable number for higher frequencies of the DRMI;
- shot noise: Optickle automatically calculates the quantum noise at each sensor, which can only enter if that particular sensor is used in a feedback loop. The noise of each sensor used is propagated through the loops to obtain the effect on the DOF;
- seismic noise: A representative spectrum of the seismic table motion is used as input noise. This noise is then propagated through the suspension transfer function to each relevant optic;
- thermal noise: This noise has been calculated by the advanced LIGO suspension group [37] [61], and we take it as input of that particular optic motion;
- BOSEM noise: BOSEM (optical sensor and electromagnetic actuator) damping noise is injected because we need to use these local suspension sensors at the top stage of each suspension to damp its resonances. The noise is an average of measured BOSEM noise, then propagated through the damped suspension transfer function and entered as optic motion in the model;
- PD electronics noise: Each PD has some electronics noise, usually referred to as dark noise, measured in situ. This noise is applied to each sensor, then propagated to the desired DOF.

MICH is the most relevant DOF for thinking of effects on full interferometer, since its coupling to DARM is only reduced by the arm finesse. However, the other DOFs can also give us relevant information about noise levels. For example, above some 100 Hz both the

PRCL DOFs should only be limited by frequency noise as shown in Figure 5.3. As such, PRCL becomes the best measurement of the true frequency noise in the interferometer. Figure 5.4 shows the similarly constructed SRCL noise budget.

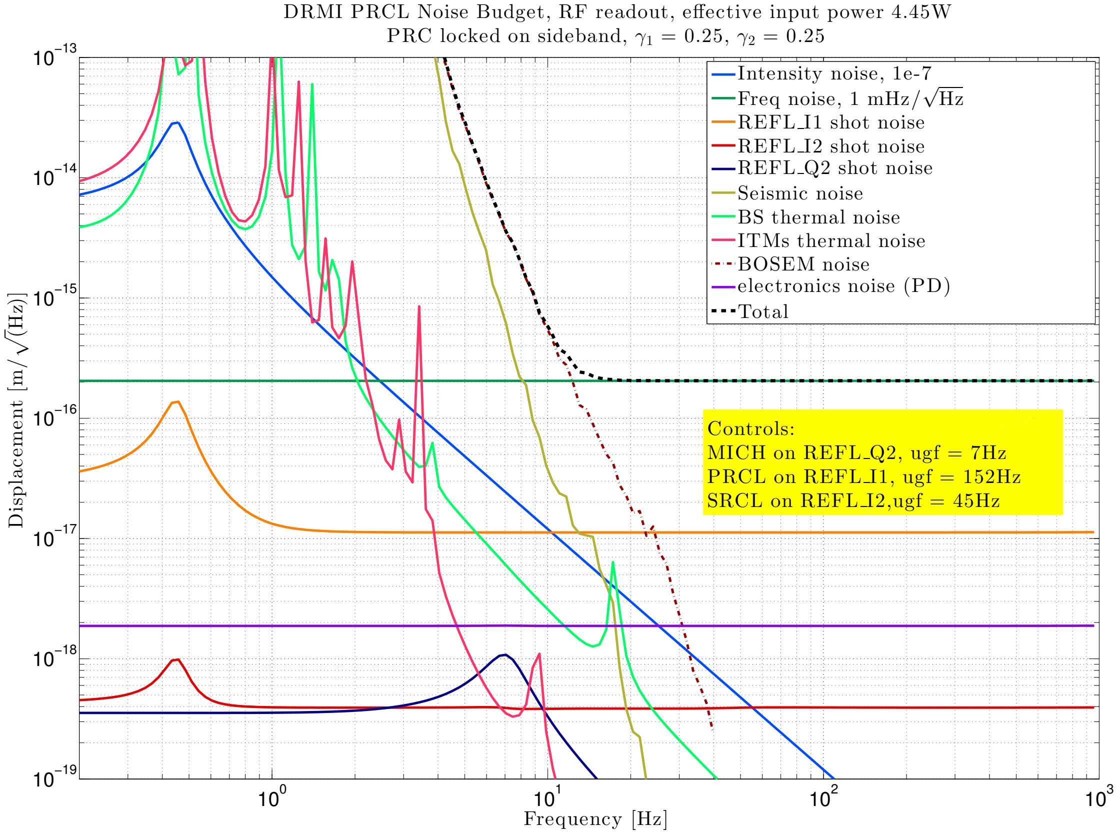

Figure 5.3: Modeled DRMI noise budget for PRCL, including the three feedback control loops with current UGFs. The input power is 5W but input optics losses reduce the effective power to 4.45W. This shows that above 10 Hz PRCL is a good sensor for frequency noise.

In the DRMI sideband lock configuration, MICH is limited at higher frequencies by shot noise, followed by the electronics noise of the sensor. Electronics noise will only be dominant if the power on the sensor is equivalent in shot noise to the electronics noise. Then the only requirement is that we choose the power on the sensor to be larger. For reference, in Table 5.1 we show the approximate dark noise levels of the three types of photodiodes (PDs) used at two different modulation frequencies as well as at DC. We will refer to them as LSC PD (length sensing and control), which is an InGas photodiode with a resonant circuit for the frequencies of interest, as BBPD (broadband PD) which is a broadband silicon photodiode and as OMC PD, a specially designed InGas photodiode for the gravitational wave signal readout.

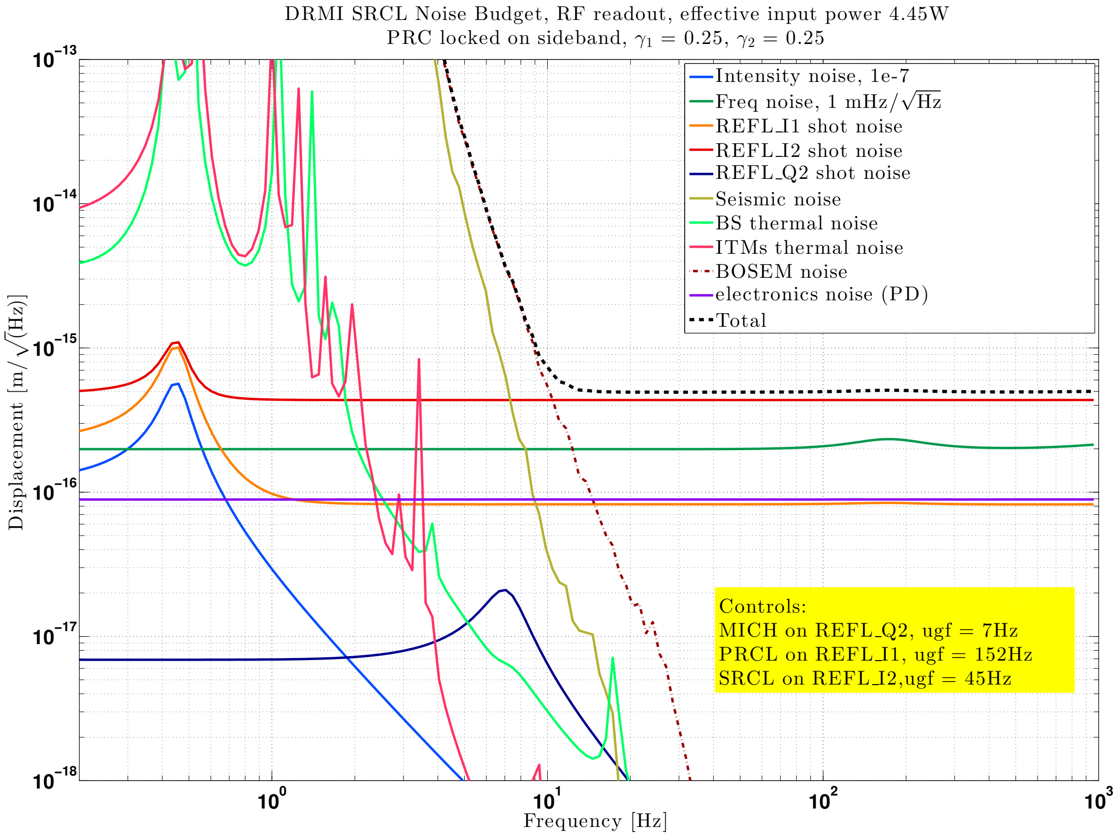

Figure 5.4: Modeled DRMI noise budget for SRCL, including the three feedback control loops with current UGFs. The input power is 5W but input optics losses reduce the effective power to 4.45W.

Table 5.1: Table of approximate electronics noise for the photodiodes used in length sensing and control.

PD & frequency	Current noise (mA)	Equivalent PD power (mW)
LSC PD at 9 MHz	1.4	1.6
LSC PD at 45 MHz	2.0	2.4
BBPD at 27 and 135 Mhz	4.0	40
OMC PD at DC	0.2	0.23

5.2.2 PRMI Noise Budget

The most sensitive configuration of the DRMI is when the PRC is locked on carrier, since it supplies much more light to be recycled and can be used in the DC readout configuration. However, as shown in Chapter 2, this configuration cannot be locked because of weak sensing of the SRCL DOF, as shown in Chapter 4. The PRMI carrier lock becomes the next best thing, its sensitivity only reduced by a factor of 3 due to the SRM transmission of 35%.

Using the same parameters as the DRMI noise budget above, but misaligning the SRM and setting the locking condition for carrier in the PRC, we obtain the noise budget in Figures 5.5 and 5.6. This requires setting a DC offset in the MICH degree of freedom to allow some carrier light to be sensed at the AS port. On the dark fringe, the carrier is minimized and as such no signal would reach the DC photodiodes. The DC offset is chosen to minimize the total background noise curve for MICH, in this case around 0.1 nm.

In order to choose the optimal DC offset for the PRMI and even for the full interferometer, there are a few conditions to be satisfied. First of all, the power on the DC photodiodes cannot exceed 100 mA. Secondly, given some intensity noise and electronics noise, there is an optimal setting where the total noise is minimized by balancing the intensity noise, electronics noise and shot noise contributions to the noise budget.

The model has a pitfall in that it does not properly model the contrast defect (the ratio of light at the AS port to the light incident on the BS on perfect dark fringe) and as such will not correctly indicate what DC offset is actually achievable. Given a contrast defect of some 10-100 ppm, which is the case in the real interferometer, in the DRMI we cannot use a DC offset much smaller than on the order of 1nm or the “junk” light at the AS port would dominate instead of the light which we allow to leak to the AS port and which carries the GW signal.

All DOFs in all configurations are limited at low frequencies by a combination of seismic noise and damping loop noise injection. The latter is not too worrisome because in a long

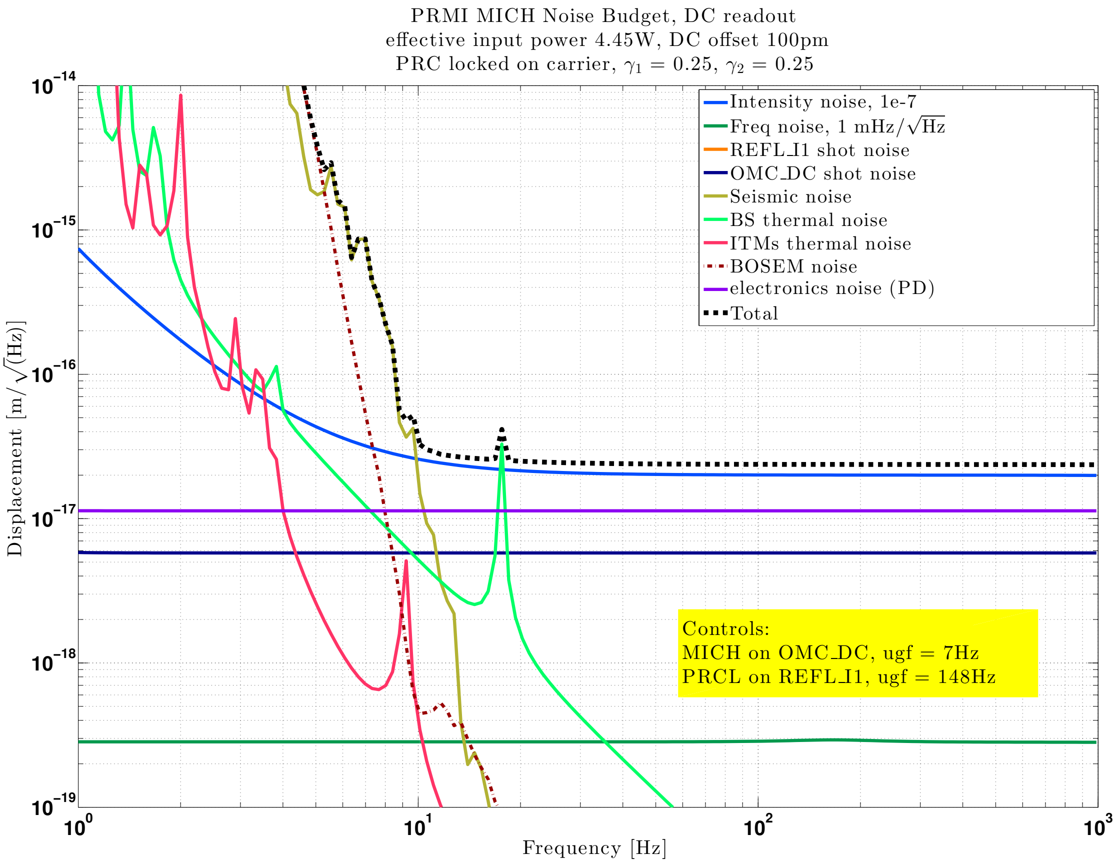

Figure 5.5: Modeled PRMI noise budget for MICH, including the two feedback control loops with current UGFs. The shot noises of the used sensors are propagated through the loops of the ideal model. The input power is 5W but input optics losses reduce the effective power to 4.45W.

full interferometer lock we can reduce the damping gains. However, in times of short locks, the lock loss transients would ring up the optics if they were not strongly damped.

The PRCL and SRCL DOFs are limited by frequency noise at higher frequencies, while the next candidate would be shot noise and electronics noise, depending on the input power used. Shot noise scales inversely with $\sqrt{\mathrm{P_{in}}}$ so (depending on the level of the frequency noise at the input of the interferometer) even a low input power of a few watts would ensure that those noise contributions are lower than that of frequency noise. The sensing matrix element scales proportionally with power, i.e. the conversion from Watts on photodiode to motion of DOF which translates to the electronics noise contribution scaling down proportionally with power.

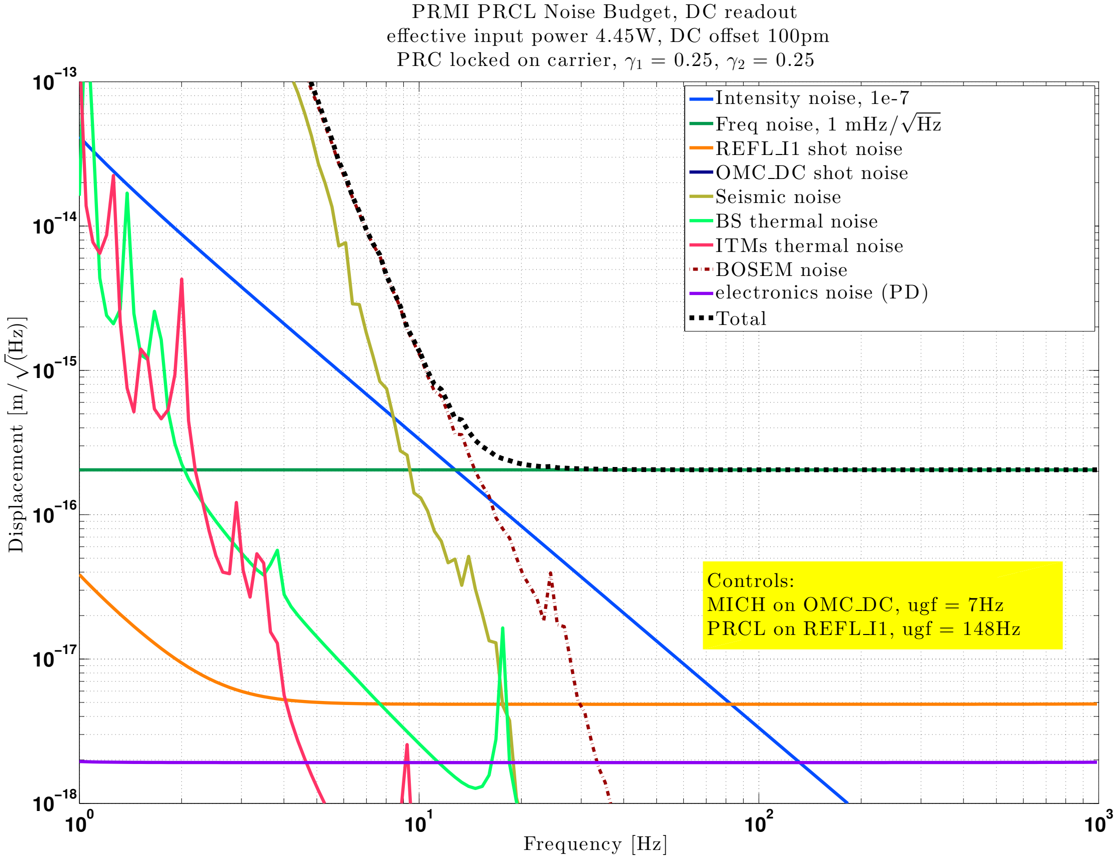

Figure 5.6: Modeled PRMI noise budget for PRCL, including the two feedback control loops with current UGFs. The shot noises of the used sensors are propagated through the loops of the ideal model. The input power is 5W but input optics losses reduce the effective power to 4.45W.

A high contribution of frequency noise to the DRMI noise budgets is not too worrisome because in the full interferometer configuration the input mode cleaner length is no longer used as a reference, but instead the common arm length feeds back to IMC length and frequency servo. The arm cavities provide a much more stable frequency reference.

5.3 Measurements

5.3.1 Power-Recycled Michelson Noise Budget

The measured noise budget for the two DOFs in the PRMI carrier-lock configuration with DC readout are shown in Figures 5.7 and 5.8. It is not the best performance of the

PRMI but I will use to showcase how noise budgeting is used in commissioning to identify and fix issues.

The calibration of the DOFs is done in by putting together the control signal sent to the optics and the readback of the error signal. The control signal is calibrated to meters of displacement by using the known electronics conversion of the driver and the transfer function of force to displacement of the particular suspensions used. Then the error signal is scaled such that the control and error signals cross at the measured UGF of the particular feedback loop. This may lead to some 20% inaccuracy especially near the UGF but for auxiliary degrees of freedom, this is sufficient.

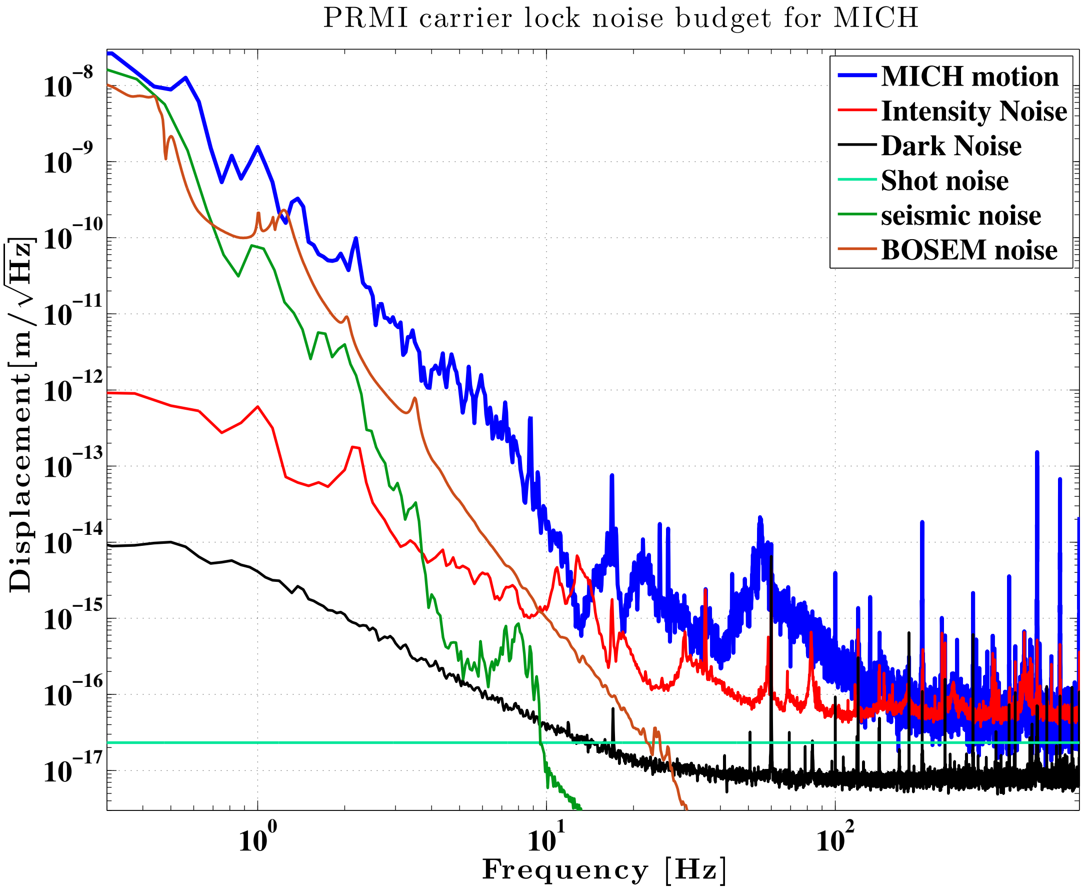

Figure 5.7: Measured PRMI noise budget for MICH, 1W input power (0.85 W effective), 1nm DC offset in MICH.

The MICH noise budget is shown in Figure 5.7. As expected, we are limited by intensity noise at higher frequencies. The DC offset used is much above the optimal one, but this is due to having a much larger contrast defect in reality than the model. This means that we have to offset the MICH enough to have the signal light dominate over the “junk” light due to this contrast. This translates in a larger intensity noise coupling. Relative intensity noise (RIN) is measured using the OMC in an un-locked configuration where one of the ITMs is misaligned to allow the input power to be sensed stably at the AS port. Then this is taken as the input intensity noise to the PRMI and scaled by the measured RIN/m at the readout when locked.

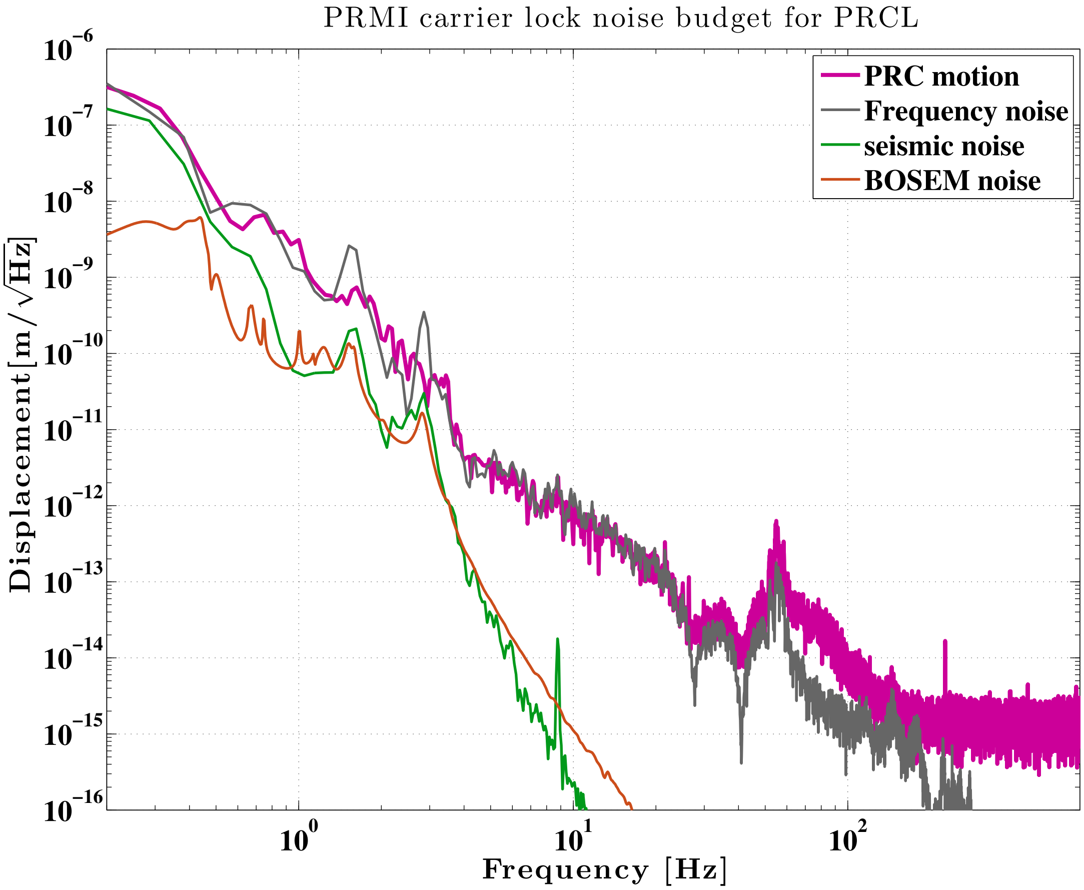

Figure 5.8: Measured PRMI noise budget for PRCL, 1W input power (0.85 W effective), 1nm DC offset in MICH.

The seismic noise is estimated exactly like in the model, where we take the relevant DOFs of the last stage of the seismic isolation, filter them through each suspension transfer function and add them together in time series. This allows for cancellations at low frequencies where we expect some of the motion to be common mode to the chambers. For example, for MICH we use the BS X and Y directions, the ITMY Y direction and the ITMX X direction. Because MICH is defined as the difference of the distances of BS to ITMX and BS to ITMY we use: $\mathrm{MICH_{sei}} = \mathrm{ITMX_x} - \mathrm{ITMY_y} + \mathrm{BS_y} - \mathrm{BS_x}$.

The BOSEM damping noise dominates over the seismic noise because we are using very strong damping loops at the top stage of each suspension. As stated before, we are not very concerned about this contribution since we can reduce the damping loop strength when locked (which means the mirrors are not moving enough to ring up the suspension resonances). The electronics noise of the sensor is below the MICH spectrum and below shot noise which means we are using sufficient power on the sensors. It is measured with no light going into the DRMI.

The sharp lines present in the measured spectrum at the 60 Hz harmonics are indicative of a grounding problem in the OMC cabling. This was found and fixed after this measurement. The three high peaks between 10 and 70 Hz show that there is some extraneous scatter present near the OMC. This was fixed by implementing shutters for the beams exiting the vacuum (for diagnostics) and slightly altering the optical paths near the OMC. The discrepancy at low frequencies is not understood well, but given our simplistic calculation of the seismic noise and BOSEM noise (we only use the length degrees of freedom), we can forsee that it could relate to other degrees of freedom of the seismic isolation and suspension cross-coupling into the length degree of freedom.

The PRCL noise budget for this configuration is shown in Figure 5.8. As explained in the model section the PRCL DOF should be limited by frequency noise. The frequency noise is measured using the input mode cleaner length control signal scaled by the loop gain and added to the dark noise of the IMC sensing which is the limiting noise source for the mode cleaner performance above a few tens of Hz. It is then scaled by the ratio of the lengths of the two cavities ($\sim 57/16$).This estimation matches the measured spectrum quite well in the mid-frequencies. As in the case of MICH, the seismic noise is calculated based on the geometry of the definition of the DOF and using the seismic isolation sensors filtered through the suspension transfer function. It is also comparable to the BOSEM damping noise. The extraneous noise above 60 Hz is due to the same scatter source as in MICH, which was fixed later.

5.3.2 Dual-Recycled Michelson Noise Budget

While the PRMI carrier-lock is the most sensitive achievable configuration of the DRMI, in the end what matters is that the DRMI sideband lock is stable enough in the locking sequence of the full interferometer. Furthermore, we can use it to assess if the auxiliary DOFs of the DRMI will be a source of noise in the full interferometer. The noise budget for this configuration DOFs is shown in Figures 5.9 to 5.11 for an input power of 1.8 W. The noise sources are estimated as for the PRMI carrier-lock case except for a few differences we will point out.

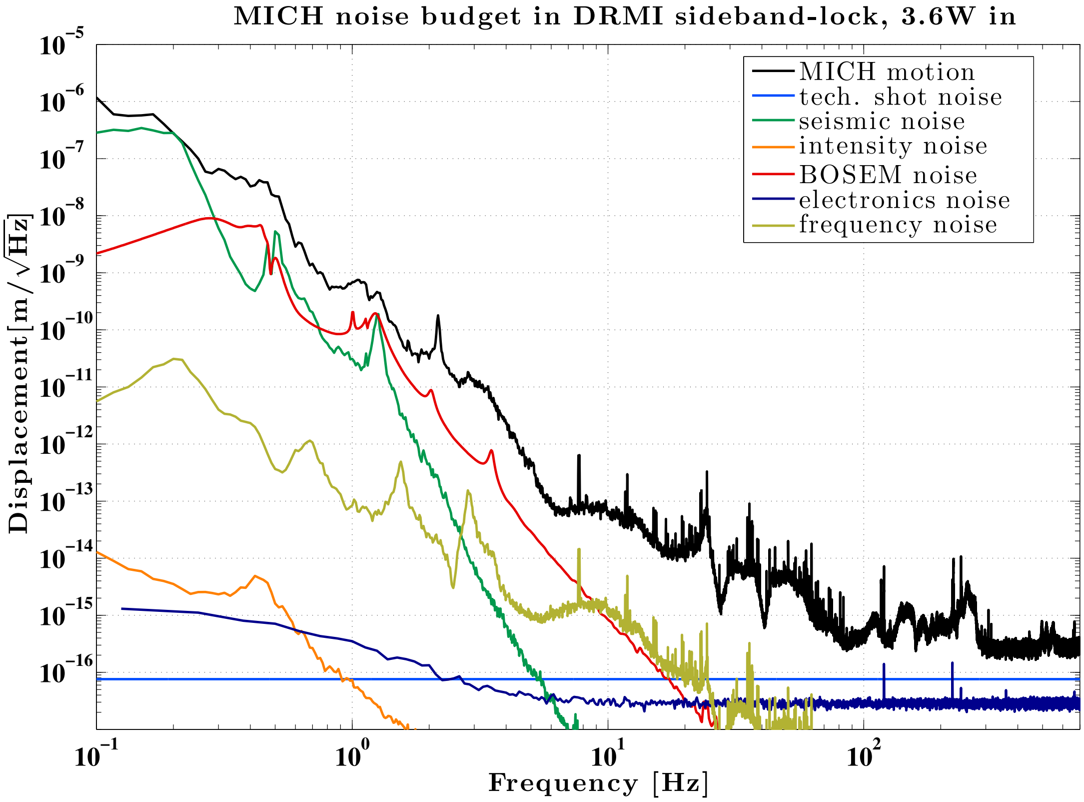

Figure 5.9: Measured DRMI sideband-locked noise budget for MICH, 3.6W input power.

The MICH noise budget changes the most between the two configurations since its sensing changes from DC to RF (OMC PD to REFL45Q). From the model, we expect to be limited by seismic noise at low frequencies and shot noise at higher frequencies. The shot noise is calculated by using the sideband power incident on the BS obtained from the POP sensors. Again, the BOSEM damping noise is above the estimated seismic noise, which is not a big problem. The seismic noise reproduces the motion around 0.2 Hz quite well. This is a check that the calculation is correct, since we know that at the microseism this motion is large and should dominate the DOF control signals above everything else.

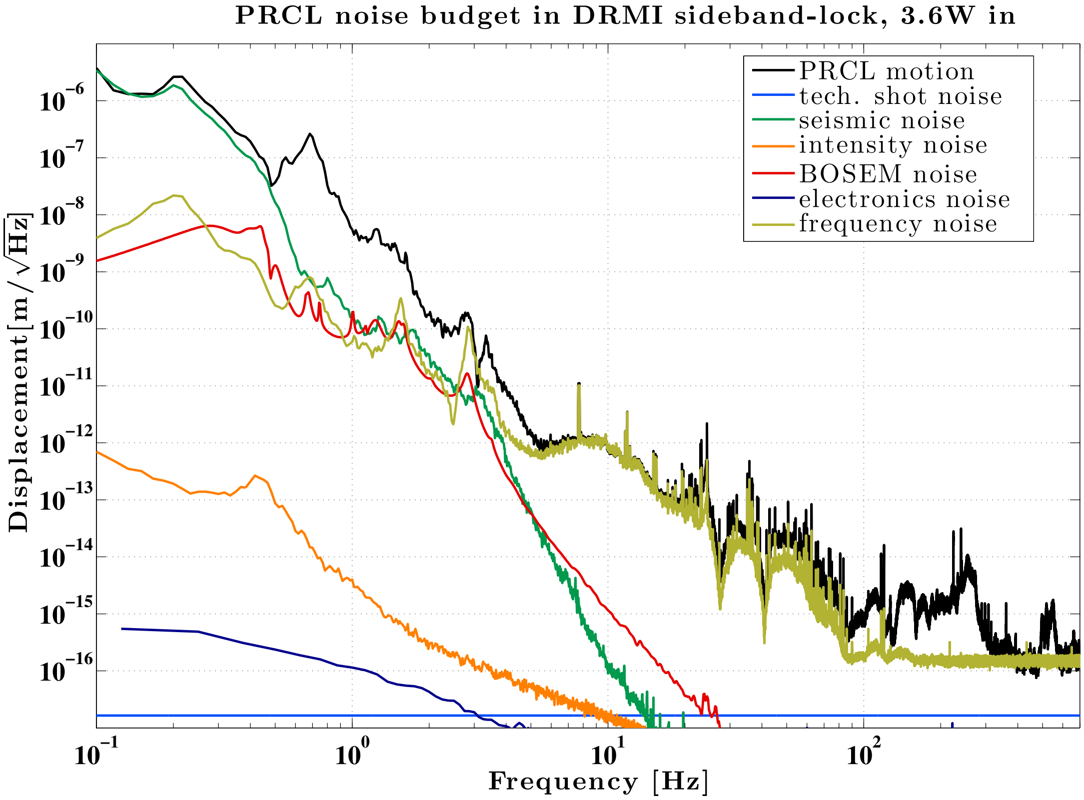

Figure 5.10: Measured DRMI sideband-locked noise budget for PRCL, 3.6W input power.

In the case of the DRMI sideband-lock, the intensity noise has a very different coupling function because the coupling mechanism is through radiation pressure of the laser light on the optics. We measure the input RIN using the intensity stabilization servo out-of-loop sensors and propagate it through the model coupling. For MICH this may not be accurate, due to the contrast defect perhaps allowing more intensity noise to couple to MICH but no coherence was found between intensity noise and the MICH DOF so we consider it to not be a dominant noise source. As before, there is excess noise in the band between 1 and 100 Hz which may be due to extraneous cross couplings of other degrees of freedom of the seismic isolation platforms and suspensions.

The frequency noise coupling can be estimated through the Schnupp asymmetry. MICH is on the dark fringe in the sideband-lock case, and so frequency noise is cancelled except for any asymmetries present. This estimation relies on the fact that we cannot distinguish between frequency and length fluctuations since we are making a phase measurement. So we can write: $\delta\phi = 2\pi\mathrm{f}\delta\mathrm{l}/\mathrm{c} = 2\pi\delta\mathrm{f}\Delta\mathrm{L}/\mathrm{c}$, where ϕ is the phase, k is the wavenumber, f is the frequency of the laser, c is the speed of light and ΔL is the Schnupp assymmetry.

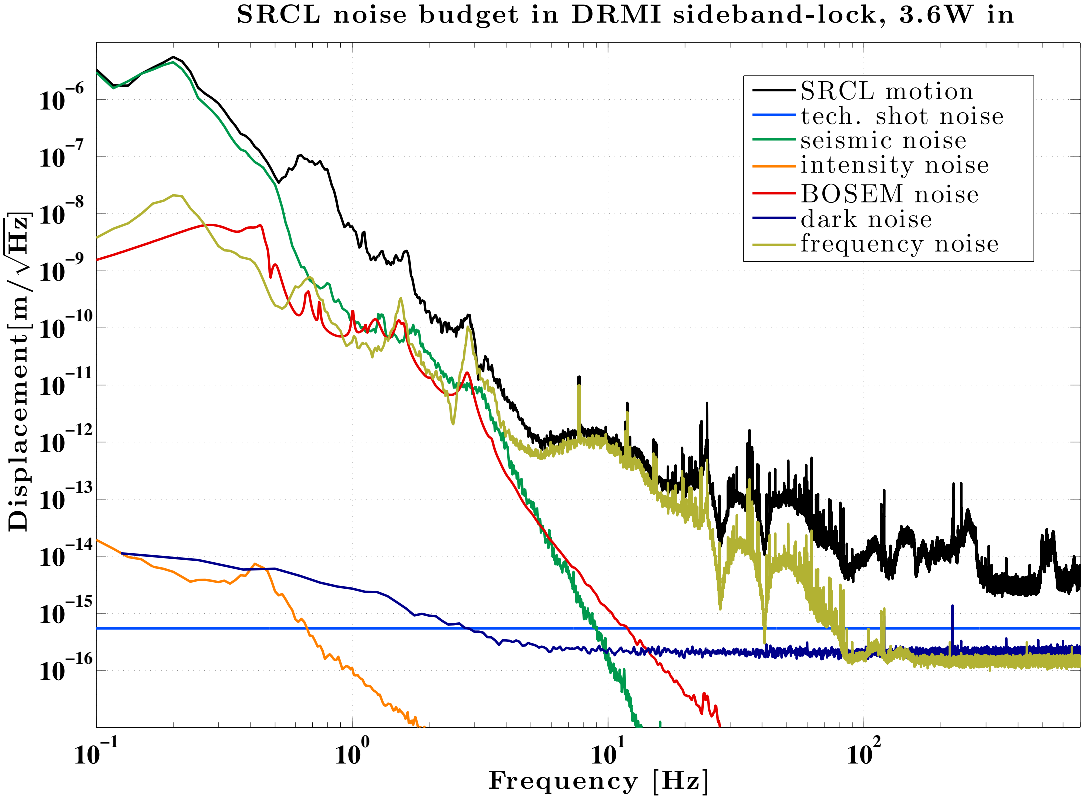

Figure 5.11: Measured DRMI sideband-locked noise budget for SRCL, 3.6W input power. THe excess motion is due to a malfunction of one of the seismic platforms, HAM4, which hosts one of the folding mirrors of the SRC.

The PRCL noise budget is very similar to the PRMI carrier configuration, with similar notes. Frequency noise estimated from the input mode cleaner dominates the spectrum, while seismic noise matches well at very low frequency. The SRCL noise budget is similar to PRCL, though the high frequency shows extra noise. Notice that the seismic curve reproduces well the microseism peak. The other noise curves are measured and calculated as before, and match their model estimations while scaling for lower input power than the model.

An important note about frequency noise is that in the full interferometer configuration it is further suppressed by the analog CARM (common arm) loop, which has a UGF in the range of 10-20kHz. The 4 km arms provide a much better frequency reference than the mode cleaner length both due to their relative lengths (4km versus 16m) and to additional seismic isolation. As such it is expected to not be limiting GW sensitivity unless the noise is a factor of 10-50 above what we measure.

While I present all DOF noise budgets for these two configurations of the DRMI, we must keep in mind what is relevant for the full interferometer. The PRCL and SRCL coupling to the GW readout (the DARM DOF) is small, so we are not particularly interested in their performance as long as their are stable and their residual motion is small. But we must track their cross-coupling to MICH, such that their coupling to DARM doesn't become higher via this path. What is important is the MICH performance since its coupling to DARM is much larger than the other DOFs. We must note that all the auxiliary couplings are reduced in the full interferometer configuration by an additional control path. The coupling transfer function from each DOF control to DARM is measured and used in a feed-forward scheme to cancel these contributions to the DARM control signal. Historically, this has been done to as low as 1% level.

CHAPTER 6
SUMMARY AND CONCLUSIONS

LIGO has had two generation of detectors, the first called initial LIGO (1999-2007) with an extension called enhanced LIGO (2008-2010) where a few upgrades were made. Then started a massive hardware overhaul for the construction of advanced LIGO, the second generation of detectors, which is supposed to be ten times more sensitive than the first generation. Chapter 2 also briefly points out the major upgrades and their effects from the first to the second generation. My dissertation work is contained in the following three chapters.

Chapter 3 presents studies of environmental effects on the detector sensitivity in enhanced LIGO, stemming from seismic, magnetic/electromagnetic and acoustic sources, performed at both sites. The steady-state background of these noise sources is shown not to have limited the detector sensitivity. In the future these studies will be extended to the advanced LIGO detectors using similar methods of environmental noise injection to assess the coupling to the detector. The next two chapters, 4 and 5, focus on the sub-configuration of LIGO called the dual-recycled Michelson interferometer (DRMI), essentially all interferometer optics except for the long arm cavities.

Chapter 4 discusses in detail modeling and measurements related to the sensing of the three auxiliary degrees of freedom to be controlled in the DRMI configuration. A simulink simulation is employed to model the entire length control loops in order to understand the cross-couplings of the three degrees of freedom and to extract an optimal sensing matrix. Given the success of this modeling, it is important in the future to expand the methods to the full interferometer in order to assess the auxiliary loop coupling to the gravitational wave readout. Chapter 4 ends with the presentation of an optical method of measuring the essential macroscopic lengths involved in the DRMI by the use of RF sensing phase comparisons of different locking conditions of the cavities involved. The measurements performed were in a suboptimal condition of the DRMI due to a high contrast defect, and so they will be repeated. It would also be interesting to see if it is possible to model how these measurements are affected by contrast defect, most likely through the introduction of a sideband imbalance.

Chapter 5 presents modeling and measurements related to the noise budget of the DRMI - the individual contributions of the various most likely noise sources to limit the detector sensitivity. The model helps in the prediction of which noise couplings are dominant and which are to be ignored, and matches the measurements in this sense. LIGO scientists, the author included, are developing real time noise budget software to continually monitor the detector sensitivity. It is vital to further refine these models, as was done for the DRMI, in order to properly understand the noise floor of the full interferometer and push it down even more where possible.

The detection of gravitational waves has never seemed so close. At the time of this writing, the advanced LIGO detector in Livingston has reached an inspiral sensitivity of 50 Mpc, which is higher by a factor of over 2 than any instrument has ever achieved. The installation of much improved hardware over initial LIGO made the first few steps towards higher sensitivity relatively easy. From here on, the noise sources preventing the detector from reaching the design sensitivity of 200 Mpc will be more insidious, and much harder to identify and mitigate for such a complex instrument. It is a fascinating time for detector science, to work with the most sensitive length detection instrument ever built while still faulting it for not being more sensitive.

REFERENCES

[1] S. J. Waldman. The advanced ligo gravitational wave detector. internal document, p0900115, MIT, 2010.

[2] LIGO Laboratory. Gwinc, the matlab gravitational wave interferometer noise calculator. `http://gwastro.org/for%20scientists/gravitational-wave-interferometer-noise-calculator`.

[3] J. Kissel. Optical layout with seismic isolation and suspensions. internal document, g1200071, LIGO Hanford Observatory, 2012.

[4] R. Abbott et al. Advligo interferometer sensing and control conceptual design. Technical Report T070247, 2007.

[5] Albert Einstein. Die grundlage der allgemeinen relativita tstheorie. *Annalen der Physik*, 49:769–822, 1916.

[6] Joseph Weber. Evidence for discovery of gravitational radiation. *Phys.Rev.Let*, 22: 1320–1324, 1969.

[7] R. A. Hulse and J. H. Taylor. Discovery of a pulsar in a binary system. *Astrophys. J.*, 195:L51–L53, 1975.

[8] J. et al Abadie. Predictions for the Rates of Compact Binary Coalescences Observable by Ground-based Gravitational-wave Detectors. *Class. Quant. Grav.*, 27(17):173001, 2010.

[9] B. Abbott et al. Upper limits on gravitational wave emissions from 78 radio pulsars. *Phys. Rev. D*, 76, 2007.

[10] Michele Maggiore. *Gravitational Waves*. Oxford, 2008.

[11] H Grote. Geo600. *Classical Quantum Gravity*, 25(11), 2008.

[12] K. Kuroda et al. Status of lcgt. *Classical Quantum Gravity*, 27, 2010.

[13] F. Acernese et al. Status of virgo. *Classical Quantum Gravity*, 25(11), 2008.

[14] A. Morse et al. Calibration and sensitivity of resonant-mass gravitational wave detectors. *Phys. Rev. D*, 59, 1999.

[15] G. Hobbs et al. The international pulsar timing array project: using pulsars as a gravitational wave detector. *Classical and Quantum Gravity*, 27(8), 2010.

[16] Weak gravitational lensing of the cmb. *Physics Reports*, 429(1):1–65, 2006.

[17] Tobin Fricke. *Homodyne Detection for Laser-Interferometric Gravitational Wave Detectors*. PhD thesis, Louisiana State University, 2011.

[18] LIGO and Virgo Scientific Collaboration. Sensitivity to gravitational waves from compact binary coalescences achieved during ligo's fifth and virgo's first science run. Technical Report T0900499, `http://dcc.ligo.org/LIGO-T0900499/public`, 2009.

[19] LIGO and Virgo Scientific Collaboration. Sensitivity Achieved by the LIGO and Virgo Gravitational Wave Detectors during LIGO's Sixth and Virgo's Second and Third Science Runs. non-journal companion to paper 4 T1100338, `http://dcc.ligo.org/LIGO-T110338/public`, 2012.

[20] for the LIGO Scientific Collaboration G. M. Harry. Advanced LIGO: The Next Generation of Gravitational Wave Detectors. *Class. Quant. Grav.*, 27(8):084006, 2010.

[21] Peter Saulson. *Fundamentals of Interferometric Gravitational Wave Detectors*. World Scientific, 1994.

[22] Malik Rakhmanov. *Dynamics of Laser Interferometric Gravitational Wave Detectors*. PhD thesis, California Institute of Technology, 2000.

[23] P. Fritschel. *Techniques for Laser Interferometer Gravitational Wave Detectors*. PhD thesis, Massachusetts Institute of Technology, 1992.

[24] Eric Black. An introduction to pound drever hall laser frequency stabilization. *American Journal of Physics*, 69(1):79, 2001.

[25] K. Arai. *Robust extraction of control signals for power-recycled interferometric gravitational-wave detectors*. PhD thesis, University of Tokyo, Tokyo, Japan, Nov 2001.

[26] Chris Mueller. *Techniques for Resonant Optical Interferometry with Applications to the Advanced LIGO Detectors*. PhD thesis, University of Florida, Jul 2014.

[27] A. Brooks. Thermal compensation system (tcs): Co2 laser projection system (co2p) final design document. Technical Report T1100570, LIGO, 2011.

[28] A. Brooks. aligo final design of ring heaters and electronics. Technical Report T1100034, LIGO, 2011.

[29] J. Mason. *Signal Extraction and optical design for an advanced gravitational-wave interferometer*. PhD thesis, California Institute of Technology, 2001.

[30] A Buonanno and Y Chen. Quantum noise in second generation, signal-recycled laser interferometric gravitational-wave detectors. *Phys. Rev. D*, 64, 2001.

[31] M. A. Arain and G. Mueller. Design of the advanced ligo recycling cavities. *Opt. Express*, 16(14):10018, 2008.

[32] J. H. Poeld. *Design, Implementation and Characterization of the Advanced LIGO 200W Laser System*. PhD thesis, Gottfried Wilhelm Leibniz Hannover University, Hannover, Germany, 2014.

[33] R. Abbott et al. Seismic isolation enhancements for initial and advanced ligo. *Classical and Quantum Gravity*, 21(5), 2004.

[34] R. Abbott et al. Seismic isolation for advanced ligo. *Classical and Quantum Gravity*, 19(7), 2002.

[35] J Giaime et al. A passive vibration isolation stack for ligo: Design, modeling, and testing. *Rev. Sci. Instrum.*, 67(208), 1996.

[36] R. DeRosa. *Performance of Active Vibration Isolation in the Advanced LIGO Detectors*. PhD thesis, Louisiana State University, 2014.

[37] N. A. Robertson et al. Quadruple suspension design for advanced ligo. *Class. Quant. Grav.*, 19(15):4043, 2002.

[38] A. V. Cummings et al. Design and development of the advanced ligo monolithic fused silica suspension. *Class. Quant. Grav.*, 29(3):035033, 2012.

[39] A. Staley et al. Achieving resonance in the advanced ligo gravitational-wave interferometer. *Classical and Quantum Gravity*, 31(24), 2014.

[40] R Ward. *Length Sensing and Control of a prototype advanced interferometric gravitational wave detector*. PhD thesis, California Institute of Technology, 2010.

[41] P. Fritschel L. Barsotti, M. Evans. Alignment sensing and control in advanced ligo. Technical Report P0900258, 2009.

[42] Matt Evans. Optickle. Technical Report G070728, 2007.

[43] Rana Adhikari. *Sensitivity and Noise Analysis of 4 km Laser Interferometric Gravitational Wave Antennae*. PhD thesis, Massachusetts Institute of Technology, 2004.

[44] P. Saulson G. Gonzalez. Brownian motion of a torsion pendulum with internal friction. *Phys. Rev. A*, 201:12–18, 1995.

[45] A. Effler et al. Environmental influences on the ligo gravitational wave detectors during the 6th science run. *Classical and Quantum Gravity*, 23(3), 2015.

[46] LIGO Scientific Collaboration. Characterization of the ligo detectors during their sixth science run. *in preparation, LIGO ref P1000142*, 2010.

[47] Robert Schofield. LIGO Environmental Influences. `http://www.ligo-wa.caltech.edu/~robert.schofield/iLIGOenvironmentalInflueinces.htm`.

[48] B. Abbott et al. LIGO: The Laser Interferometer Gravitational Wave Observatory. *Rep. Prog. Phys*, 72(7):076901, 2009.

[49] R. DeRosa et al. Global feed-forward vibration isolation in a km scale interferometer. *Class. Quant. Grav.*, 29(21):215008, 2012.

[50] S. Wen. *Improved Seismic Isolation for the Laser Interferometer Gravitational Wave Observatory with Hydraulic External Pre-Isolator System*. PhD thesis, Louisiana State University, 2008.

[51] E J Daw et al. Long-term study of the seismic environment at LIGO. *Class. Quant. Grav.*, 21(9):2255, 2004.

[52] R. Cessaro. Sources of Primary and Secondary Microseisms. *B.S.S.A.*, 84(1):142–148, 1994.

[53] D. M. Macleod et al. Reducing the effect of seismic noise in LIGO searches by targeted veto generation. *Class. Quant. Grav.*, 29(5):055006, 2012.

[54] E. Goetz et al. PlaneMon: Airplane Detection Monitor. Internal document, t050174, LIGO, 2005.

[55] B. Abbott et al. Beating the spin-down limit on gravitational wave emission from the Crab pulsar. *Astrophys J. Lett*, 683(1):L45, 2008.

[56] J. Smith. The path to the enhanced and advanced LIGO gravitational-wave detectors. *Class. Quant. Grav.*, 26(11):114013, 2008.

[57] T. T. Fricke, N. D. Smith-Lefebvre, R. Abbott, R. Adhikari, K. L. Dooley, M. Evans, P. Fritschel, V. V. Frolov, K. Kawabe, J. S. Kissel, B. J. J. Slagmolen, and S. J. Waldman. DC readout experiment in Enhanced LIGO. *Classical and Quantum Gravity*, 29 (6):065005, March 2012.

[58] R. Weiss. Various Reports of Experiments Conducted on the Barkhausen Noise Various Reports of experiments conducted on the barkhausen noise research. internal document, t080355, MIT, 2008.

[59] L. Barsotti D. Martynov. Prcl, srcl and schnupp asymmetry length measurements. `https://alog.ligo-la.caltech.edu/aLOG/index.php?callRep=8562`, Sep 2013.

[60] N. Smith-Lefebvre. *Techniques for improving the readout sensitivity of gravitational wave antennae*. PhD thesis, Massachusetts Institute of Technology, Jun 2012.

[61] Mark Barton. Conceptual design for beamsplitter suspension for advanced ligo. Technical report, LIGO Hanford Observatory, 2004.

APPENDIX A
THE MICHELSON INTERFEROMETER FIELDS

In order to understand how a Michelson interferometer detects gravitational waves, we must derive the laser field equations linking the output of a Michelson (as power on a photodiode) to a change in its differential length. First consider what happens to laser fields as they encounter an optic, as shown in figure A.1.

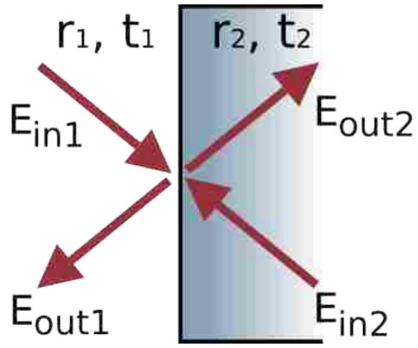

Figure A.1: Fields at the boundary of a mirror, with smaller index of refraction on the left hand side, characterized by field reflectivity and transmission r_1 and t_1. The higher index medium - the optic - is characterized by r_2 and t_2. All coefficients are complex numbers.

We can write three equations, two pertaining to writing the output fields on each side of the boundary as a combination of the input fields, and one pertaining to conservation of energy at the boundary (assuming lossless media).

$$\mathrm{E_{out_1}} = \mathrm{E_{in_1}} * \mathrm{r_1} + \mathrm{E_{in_2}} * \mathrm{t_2}$$

$$\mathrm{E_{out_2}} = \mathrm{E_{in_1}} * \mathrm{t_1} + \mathrm{E_{in_2}} * \mathrm{r_2}$$

$$|\mathrm{E_{in_1}}|^2 + |\mathrm{E_{in_2}}|^2 = |\mathrm{E_{out_1}}|^2 + |\mathrm{E_{out_2}}|^2$$

Solving these equations we obtain that the real parts of the reflectivities are equal, as well as the real parts of the transmissions. We also obtain a restriction on the phase relation of these coefficients: $\phi_{\mathrm{r_1}} + \phi_{\mathrm{r_2}} - \phi_{\mathrm{t_1}} - \phi_{\mathrm{t_2}} = \pi$. There are several conventions which can be used, but for the calculations in this dissertation we use the convention of $\phi_{\mathrm{r_1}} = \pi$ and $\phi_{\mathrm{r_2}} = \phi_{\mathrm{t_1}} = \phi_{\mathrm{t_2}} = 0$. In other words, when reflecting off of a medium with higher index of refraction, the field acquires a minus sign. Otherwise, the field reflection and transmission coefficients for a mirror are real numbers equal to the square root of the power reflection and transmission coefficients.

A.1 Field Derivation

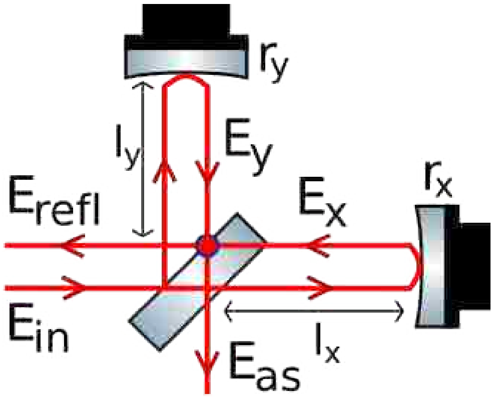

Figure A.2: A diagram of a simple Michelson interferometer with arms denoted as X and Y, where E_{in} is the laser field entering the interferometer, E_{as} is the field at the anti-symmetric port, E_x and E_y are the fields in the arms, and E_{refl} is the reflected field.

Using the parameters as set up in figure A.2 we calculate the fields in the arms and at the anti-symmetric port, assuming that the beam splitter is 50/50 i.e. $\mathrm{r_{BS}} = \mathrm{t_{BS}} = \frac{1}{\sqrt{2}}$. When propagating in vacuum a distance L, the field simply acquires a factor of $\mathrm{e^{ikL}}$, where k is the wavenumber. For example, E_x at the BS boundary is obtained by propagating $\mathrm{E_i}$n through the beam splitter with $\mathrm{t_{BS}}$, over distance l_x, reflected from the end mirror with -r_x, and over another distance of l_x.

$$\mathrm{E_x} = -\tfrac{1}{\sqrt{2}}\mathrm{r_x E_{in} e^{2ikl_x}}$$

$$\mathrm{E_y} = \tfrac{1}{\sqrt{2}}\mathrm{r_y E_{in} e^{2ikl_y}}$$

$$\mathrm{E_{as}} = \tfrac{1}{\sqrt{2}}(\mathrm{E_x} + \mathrm{E_y}) = \tfrac{1}{2}\mathrm{E_{in}}(\mathrm{r_y e^{2ikl_y}} - \mathrm{r_x e^{2ikl_x}})$$

Calculating the power at the anti-symmetric port:

$$\mathrm{P_{as}} =\mid \mathrm{E_{as}} \mid^2 = \tfrac{1}{4}\mathrm{P_{in}}[(\mathrm{r_x} - \mathrm{r_y})^2 + 4\mathrm{r_x r_y} \sin(\mathrm{k}(\mathrm{l_x} - \mathrm{l_y}))]$$

the dark fringe (minimum power) is given by: $\mathrm{P_{as}} = \frac{1}{4}\mathrm{P_{in}}[(\mathrm{r_x} - \mathrm{r_y})^2]$ and the bright fringe (maximum power) is given by: $\mathrm{P_{as}} = \frac{1}{4}\mathrm{P_{in}}[(\mathrm{r_x} + \mathrm{r_y})^2]$.

Since a gravitational wave would only have a differential effect on the lengths of the two arms, let's redefine the length basis into a differential arm length $\Delta l = l_x - l_y$ and an average arm length $l = \frac{l_x + l_y}{2}$. Then the field at the AS port becomes:

$E_{as} = -\frac{1}{2}E_{in}e^{i2kl}(r_x e^{ik\Delta L} - r_y e^{-ik\Delta L}) = -\frac{1}{2}E_{in}e^{i2kl}((r_x - r_y)\cos(k\Delta L) + i(r_x + r_y)\sin(k\Delta L))$

And with a further simplification that $r_x = r_y \approx 1$

$$E_{as} \approx -E_{in} i e^{i2kl} \sin(k\Delta L)$$

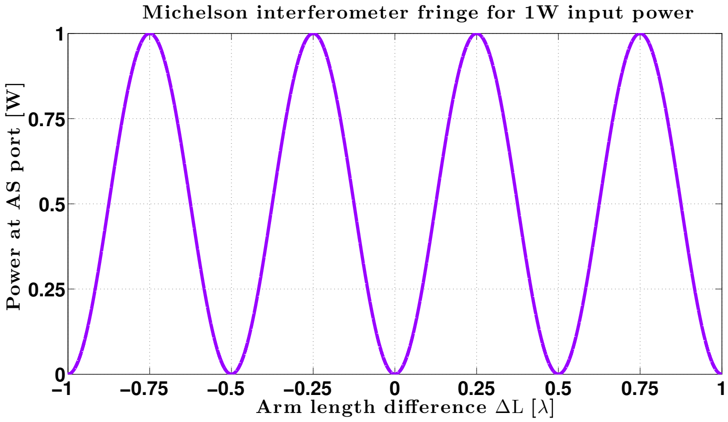

Figure A.3: The power at the anti-symmetric (AS) port as the difference between the Michelson interferometer changes.

The effect of a gravitational wave is only on $\Delta L \rightarrow \Delta L + 2hl$ since the strain h lengthens or shortens each arm proportional to its length. The average arm length remains unchanged. Then the power at the AS port becomes:

$$P_{as} = \mid E_{as} \mid^2 \approx P_{in}\sin^2(k\Delta L + 2khl).$$

If ΔL is zero, the coupling of h to the readout is not linear but quadratic! This can be seen from figure A.4, since at the bottom of the fringe the slope in Watts per meter is zero. We would prefer to be at mid-fringe where this slope is maximum, but laser noise would no longer cancel and would dominate above any gravitational wave signal. There are two options for dealing with this conundrum. Either we operate slightly off the dark fringe allowing some small amount of light to the AS port - this is called a homodyne readout or "DC "readout. Or we can set up a macroscopic length difference in the arms and RF sidebands whose frequency is chosen such that when the Michelson is perfectly dark to the carrier, it is not dark for the sidebands; the readout is then a beat between carrier and sideband called heterodyne or ”RF” readout. The macroscopic length difference is called the Schnupp asymmetry and in LIGO is on the order of few to tens of cm, depending on the desired coupling of the sidebands at the AS port.

A.2 RF Readout

The idea of using RF sidebands in order to get a linear relative phase control signal for control and readout of optical systems comes from the Pound-Drever-Hall technique [24] for Fabry-Perot cavities, as discussed in Chapter 2.

Applying phase modulation to the laser with frequency ω_m and modulation depth γ, we can approximate the input field into separate terms of different frequencies and propagate each one separately to the output using the transmission coefficient derived above. ω_0 is the frequency of the laser and $\mathrm{k} = \frac{\omega}{\mathrm{c}}$ will differ for each term. For a 1 micron laser as used in LIGO the frequency is on the order of 300 THz while the applied RF sidebands are in the few to tens of MHz. I will use the following approximations: $\mathrm{e}^{\mathrm{iz}\cos\phi} = \sum\limits_{\mathrm{i}=-\infty}^{\infty} \mathrm{i}^\mathrm{n} \mathrm{J}_\mathrm{n}(\mathrm{z}) \mathrm{e}^{\mathrm{in}\phi}$ and $\mathrm{J}_{-1}(\mathrm{x}) = -\mathrm{J}_1(\mathrm{x})$.

$$\mathrm{E}_\mathrm{in} = \mathrm{E}_0 \mathrm{e}^{\mathrm{i}(\omega_0 \mathrm{t} + \gamma\cos\omega_\mathrm{m}\mathrm{t})} \approx \mathrm{E}_0 \mathrm{e}^{\mathrm{i}\omega_0\mathrm{t}} (\mathrm{J}_0(\gamma) + \mathrm{i}\mathrm{J}_1(\gamma)\mathrm{e}^{\mathrm{i}\omega_\mathrm{m}\mathrm{t}} + \mathrm{i}\mathrm{J}_1(\gamma)\mathrm{e}^{-\mathrm{i}\omega_\mathrm{m}\mathrm{t}} + ...)$$

$$\mathrm{T}_\mathrm{as}(\omega) \equiv \mathrm{i}\mathrm{e}^{\mathrm{i}2\mathrm{kl}}\sin(\mathrm{k}\Delta\mathrm{L}),\ \mathrm{T}_0 \equiv \mathrm{T}_\mathrm{as}(\omega_0),\ \mathrm{T}_+ \equiv \mathrm{T}_\mathrm{as}(\omega_0 + \omega_\mathrm{m}),\ \mathrm{T}_- \equiv \mathrm{T}_\mathrm{as}(\omega_0 - \omega_\mathrm{m})$$

$$\mathrm{E}_\mathrm{as} = \mathrm{E}_0 \mathrm{e}^{\mathrm{i}\omega_0\mathrm{t}} (\mathrm{J}_0(\gamma)\mathrm{T}_0 + \mathrm{i}\mathrm{J}_1(\gamma)\mathrm{T}_+\mathrm{e}^{\mathrm{i}\omega_\mathrm{m}\mathrm{t}} + \mathrm{i}\mathrm{J}_1(\gamma)\mathrm{T}_-\mathrm{e}^{-\mathrm{i}\omega_\mathrm{m}\mathrm{t}})$$

The power at the AS port is $\mathrm{P}_\mathrm{as} = |\mathrm{E}_\mathrm{as}|^2$ so some algebra is required. I recommend splitting the exponentials into sin and cos and not expanding the transmission coefficients. We are interested in DC and ω_m sinusoidal terms:

$$\mathrm{P}_\mathrm{as} = \mathrm{P}_\mathrm{c}|\mathrm{T}_0|^2 + \mathrm{P}_\mathrm{s}|\mathrm{T}_+|^2 + \mathrm{P}_\mathrm{s}|\mathrm{T}_-|^2 - 2\sqrt{\mathrm{P}_\mathrm{c}\mathrm{P}_\mathrm{s}}\,\mathrm{Im}[\mathrm{S}]\cos\omega_\mathrm{m}\mathrm{t} + 2\sqrt{\mathrm{P}_\mathrm{c}\mathrm{P}_\mathrm{s}}\,\mathrm{Re}[\mathrm{S}]\sin\omega_\mathrm{m}\mathrm{t}$$

where $\mathrm{S} = \mathrm{T}(\omega_0)^*\mathrm{T}(-\omega_\mathrm{m}) - \mathrm{T}(\omega_0)\mathrm{T}(\omega_\mathrm{m})^*$,

$\mathrm{P}_\mathrm{c} = \mathrm{J}_0(\gamma)^2\mathrm{P}_\mathrm{in}$ is the power in the carrier and

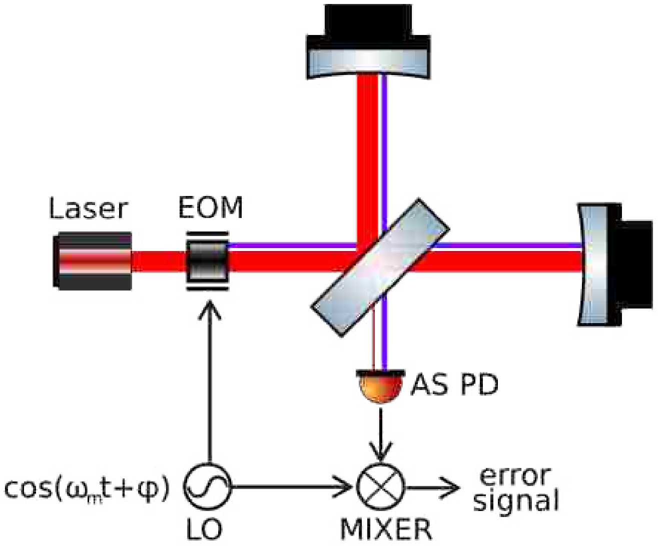

Figure A.4: Setup for RF readout of a Michelson interferometer. An electro-optical modulator (EOM) is used to aply the phase modulation from the local oscillator (LO) at the input. The same local oscillator is then used as reference for the demodulation of the photodiode signal using a mixer.

$$\mathrm{P_s = J_1(\gamma)^2 P_{in}} \text{ is the power in each sideband.}$$

Demodulating at ω_m, since the initial modulation was a cosine, we obtain two phases which pick out either the sine (out of phase ≡ Q) or cosine (in phase ≡ I) terms from $\mathrm{P_{as}}$, since through integration only terms such as (sin × sin) or (cos × cos) are non-zero.

$$\mathrm{AS\_I} = \langle \mathrm{P_{as}} \cos(\omega_\mathrm{m} \mathrm{t}) \rangle = -\sqrt{\mathrm{P_c P_s}}\, \mathrm{Im[S]}$$

$$\mathrm{AS\_Q} = \langle \mathrm{P_{as}} \sin(\omega_\mathrm{m} \mathrm{t}) \rangle = \sqrt{\mathrm{P_c P_s}}\, \mathrm{Re[S]}$$

Now we must expand S to find out the response to a gravitational wave and we will express $\Delta \mathrm{L} \to \Delta \mathrm{L_S} + \delta \mathrm{l}$, where $\Delta \mathrm{L_S}$ is the Schnupp asymmetry and $\delta \mathrm{l}$ is the differential signal from a GW that we are interested in detecting.

$$\begin{aligned} \mathrm{S} =& \mathrm{T}(\omega_0)^* \mathrm{T}(-\omega_\mathrm{m}) - \mathrm{T}(\omega_0)\mathrm{T}(\omega_\mathrm{m})^* = \\ &= -\mathrm{i} e^{-\mathrm{i}2k_0 l} \sin(k_0 \Delta L) \mathrm{i} e^{\mathrm{i}2(k_0 - k_m) l} \sin(k_0 \Delta L - k_m \Delta L) - \\ &\quad \mathrm{i} e^{\mathrm{i}2k_0 l} \sin(k_0 \Delta L)(-\mathrm{i}) e^{-\mathrm{i}2(k_0 + k_m) l} \sin(k_0 \Delta L + k_m \Delta L) = \\ &= 2 e^{-\mathrm{i}2k_m l} \sin(k_0 \Delta L) \cos(k_0 \Delta L) \sin(k_m \Delta L) \end{aligned}$$

Setting the carrier on the dark fringe means $\mathrm{k_0\Delta L_S = n\pi}$ so $\mathrm{sin(k_0\Delta L) \approx k_0\delta l}$. But the sideband is not dark, so $\mathrm{sin(k_m\Delta L) \approx sin(k_m\Delta L_S)}$. Then:

$$\mathrm{S = 2k_0\delta l e^{-2ik_m l} sin(k_m\Delta L_S)}$$

which is linear in δl and so both AS_I and AS_Q signals are linear in δl. It is customary to rotate the phase between I and Q in the readout electronics such that all differential signal is in one phase, e.g. Q. The final demodulated signals become:

$$\mathrm{AS\_I = 2\sqrt{P_c P_s} k_0 sin(k_m\Delta l_S) sin(2k_m l) \times \delta l,}$$

$$\mathrm{AS\_Q = 2\sqrt{P_c P_s} k_0 sin(k_m\Delta l_S) cos(2k_m l) \times \delta l.}$$

Advanced LIGO uses DC readout, where the carrier fringe is slightly offset from minimum. However, the Schnupp asymmetry is still required for the other degrees of freedom.

APPENDIX B
PERMISSIONS

The results in Chapter 3 have been published in the Classical and Quantum Gravity (CQG) journal whose policy allows reproduction of published articles in dissertations. The communication with the publishers at CQG on this topic is pasted below.

Dear Anamaria,
Thank you for your email.
Upon transfer of copyright, IOP and/or the copyright owner grants back to authors a number of rights. These include the right to include the article in research theses or dissertations. Please include citation details and for online use, a link to the Version of Record. IOP's permission will be required for commercial use of an article published as part of your thesis.

Kind Regards
Gemma

Please note: We do not usually provide signed permission forms as a separate attachment. Please print this email and provide it to your publisher as proof of permission.

Gemma Alaway
Rights & Permissions Adviser
IOP Publishing
Temple Circus, Temple Way, Bristol
BS1 6HG, UK
Direct line +44 (0)117 930 1146
ioppublishing.org

VITA

Anamaria Effler was born and lived in the city of Arad, Romania until the age of 18. After graduating high-school in 2002, she attended Caltech for her undergraduate degree in Physics, which she completed in 2006. There she learned about LIGO and has been with the project ever since. She worked as operations specialist at the LIGO Hanford Observatory for 3 years and then started her graduate studies at LSU in Baton Rouge in 2009. During her time as a tiger, she's been mostly hanging out at the LIGO Livingston Observatory where she will continue her research as a Caltech postdoc after the completion of her Ph.D.